Complete characterisation of the crystal electric field in Ce Kondo lattices with resonant inelastic soft X-ray scattering

Andrea Amorese

Communauté
UNIVERSITÉ Grenoble Alpes

THÈSE

Pour obtenir le grade de

DOCTEUR DE LA COMMUNAUTÉ UNIVERSITÉ GRENOBLE ALPES

Spécialité : **Physique de la matìere condensée et du rayonnement**

Arrêté ministériel : 25 Mai 2016

Présentée par

Andrea AMORESE

Thèse dirigée par **Nicholas Brookes**
et codirigée par **Kurt Kummer**

préparée au sein du **European Synchrotron Radiation Facility**
et de l'**École doctorale de Physique de Grenoble**

Une caractérisation complète du champ cristallin dans les réseaux Kondo à base de cérium par diffusion inélastique résonante de rayons X

Thèse soutenue publiquement le **31 mars 2017**,
devant le jury composé de :

Pr. Olivier Isnard
Université Grenoble Alpes & Institut Néel, Président

Pr. Gerrit van der Laan
Diamond Light Source, Rapporteur

Pr. Liu Hao Tjeng
Max Planck Institute for Chemical Physics of Solids, Rapporteur

Dr. Andrea Severing
University of Cologne, Examinatrice

Dr. Nicholas Brookes
European Synchrotron Radiation Facility, Directeur de thèse

Dr. Kurt Kummer
European Synchrotron Radiation Facility, Co-Directeur de thèse

To you as a reader.

Acknowledgements

In these three years of PhD, I grew both as a scientist and as a person and I want to acknowledge everyone that contributed to this process.
Firstly, I would like to express my sincere gratitude to my thesis director Nicholas Brookes, who put his trust in me since the beginning of the project, and my thesis supervisor Kurt Kummer, which has always been understanding and patient with me. They have believed in my skills and ideas more than I did and have been forgiving of my initial inexperience, allowing me to work serenely towards my goals. By doing so, they have been able to take out the best of me.
Together with my advisors, I want to acknowledge the daily dedication and hard work that the ID32 beamline staff puts into the maintenance of the instrumentation. I learned a lot from the strengths of each member of this united team and they all deserve to be listed by name. I admired the determination and genuineness with whom Flora Yakhou-Harris, the ID32 beamline operation manager, can face every situation. Andrea Fondacaro, the beamline technician, besides knowing everything about the instrumentation, is the most sympathetic, generous and helpful person I ever met, always ready to give wise and disinterested advice. The two Post-Docs have been good companions for relaxed chats and laughs during the breaks. Emilio Velez-Fort, with his easygoing and positive approach to problems, and Davide Betto, with his unshakable enthusiasm and willingness, make a perfect working pair. I would also like to mention the newcomers, Emilie Lefrançoise and Ivan Spinelli, which already integrated perfectly in the group and I wish them all the best. So, I thank the whole ID32 team for the enjoyable, relaxing and pleasant time spent together.
I am also very thankful to Pr. Giacomo Ghiringhelli and Pr. Lucio Braicovich of Politecnico di Milano, with whom I moved the first steps in this fascinating world during my master thesis and which taught me all the secrets of RIXS spectroscopy. Beside designing and commissioning the ERIXS spectrometer and polarimeter, they kept enlightening me with fruitful discussions, which have been very useful for this PhD project. I also would like to acknowledge the rest of the

Politecnico di Milano team, Yingying Peng and Greta Dellea, which have been a nice company during the long, stressful and sometimes disorienting nights (and weeks) of commissioning.
Thanks to Maurits Haverkort for providing the SolidStatePhysics package for Mathematica and the Quanty code, with whom all the calculations in this thesis have been performed. The samples have been prepared at the Max-Planck-Institute for Chemical Physics of Solids in Dresden, in the group of Christoph Geibel. I thank him and his team members, Silvia Seiro and Nubia Caroca-Canales, for their excellent work.
I want to express my gratitude to Pr. Olivier Isnard, Pr. Gerrit van der Laan, Pr. Liu Hao Tjeng and Dr. Andrea Severing for agreeing to serve on my thesis committee. It is an honor for me that such experienced and prominent scientists considered my work worth of their precious time.
I wish to thank all my friends, new and old. And finally, special thanks to my family and my girlfriend, without whom none of my achievements would have been possible.

Contents

Chapter 1

Cerium intermetallic compounds and the physics of the $4f$ shell

1.1 Properties of cerium intermetallics

Cerium intermetallic compounds are solid state materials containing, in addition to Cerium, metallic and optionally non-metallic elements, arranged in a crystal structure different from that of the constituents. They belong to the group of *strongly correlated materials*, meaning that they are characterized by a strong interplay among the electrons, which cannot be considered as a uniform sea of non-interacting particles. Typically, correlated materials have ions with incompletely filled d- or f- electron shells for which the charge distribution is highly anisotropic. The behavior of the electrons cannot be described as non interacting charged particles in a mean field and many-body approaches need to be applied to account for their correlated motion. Many peculiar physical properties can arise in correlated materials, some of which are still matter of debate among researchers.

In particular, the physics of lanthanide- and actinide-based intermetallic compounds derives from the electrons in the partially filled f orbitals, which behave like localized magnetic moments in a sea of itinerant conduction electrons. The interaction between f and conduction electrons leads to two competing effects: On the one hand the conduction electrons can mediate a coupling among f electrons at different lattice sites via the Ruderman-Kittel-Kasuya-Yoshida (RKKY) interaction, favouring a magnetically ordered ground state. On the other hand, the local moments on each site tend to be screened by the conduction electrons, producing a non-magnetic state due to the so-called Kondo screening. Both the

RKKY and Kondo effects arise at low temperatures and their competition leads to remarkable magnetic, thermodynamic and electronic behaviours [1, 2, 3]. These compounds are often referred to as heavy fermions, since the interaction of conduction electrons with localized f states may result in the observation of an enhanced electron effective mass in measurements as specific heat or resistivity. Furthermore, these systems range from magnetically ordered (ferromagnetic or, more often, antiferromagnetic) to Kondo-screened or intermediate valent, and from metallic or superconducting to Kondo-insulating. Quantum critical phenomena and non-Fermi liquid behavior arise when passing from one regime to another.

Because of this exceptional diversification of uncommon properties, the scientific interest in Kondo and heavy-fermion materials continuously increased in the last 80 years [3]. Many aspects of heavy-fermion physics are still not understood and the presence of so many large anomalies made these systems "*a paradise for experimentalists*" but "*a nightmare for theoreticians*" [4]. The most studied heavy fermion materials are Ce and Yb based systems, for their large variety and relative simplicity due to the presence of a single $4f$ electron or hole. However, many other compounds (as those of Pr, Sm, U and Pu) exhibit the same fascinating phenomena.

This thesis focuses in particular on the study of the characteristics of f levels in Ce compounds that grow in the $ThCr_2Si_2$ crystal structure, also called the 122 family. In the following, a short review of heavy fermions' history and properties is presented, following references [3, 4, 5, 6] and the references therein. The many possible effects arising from the interaction between the f states and conduction electrons are reviewed, before going into the details of how to study the energy and symmetry of the $4f$ levels.

1.1.1 Historical outline

The study of the Kondo effect dates back to 1934, when de Haas *et al.* [7] measured the electrical resistivity of a gold wire with a small amount of impurities and found an unexpected increase of the resistivity at low temperatures, with a minimum around 4 K. The same behavior was later found in dilute magnetic alloys [8], suggesting a connection to the presence of magnetic impurities. A theoretical explanation for this anomaly was missing until 1964, when Kondo [9] analyzed the scattering of electrons with magnetic impurities on the basis of a model developed by Anderson [10] three years earlier. The so-called Anderson impurity model (AIM) predicted an antiferromagnetic exchange interaction between the localized magnetic moment of the impurity and the free electrons in a metal. Kondo applied the third-order perturbation theory to study the scattering rate caused by such screened magnetic

impurities and found a term proportional to $\ln(T^{-1})$, which caused the resistivity increase at low temperatures. This term, combined with the the electron-phonon and electron-electron scattering contributions, which on the contrary increase with temperature, causes the observed minimum in the resistivity. The minimum occurs around a characteristic temperature T_K (*Kondo temperature*) at which the antiferromagnetic coupling between the magnetic impurities and the conduction electrons becomes relevant. As a result of the coupling, the local moment is screened and a non-magnetic *Kondo-singlet* state forms at each site, with an energy scale $k_B T_K$.

In 1975 another unexpected experimental result, by Andres *et al.* [11], set the discovery of a new class of materials: heavy fermions (HF). They measured a value of the specific heat coefficient in $CeAl_3$ about a thousand times larger than the one of typical metals, meaning that the effective electron mass in this compound was significantly enhanced compared to the free electron. Soon after, in 1977, Doniach [12] suggested the periodical arrangement of Kondo impurities in the crystal structure (*Kondo lattice*) as a cause of the heavy-fermion behavior.

The already large interest in heavy fermions gained an additional boost with the discovery of unconventional superconductivity. Curiously, the very first observation of superconductivity in heavy-fermion materials was almost simultaneous with the discovery of the materials themselves. Bucher *et al.* [13] measured superconductivity in UBe_{13} already in 1975, but dismissed it as an artifact because the presence of magnetic moments was supposed to forbid superconductivity, according to the predictions of the BCS theory (Bardeen-Cooper-Schrieffer [14]). More convincing results were obtained in 1979 by Steglich *et al.* on $CeCu_2Si_2$ [15]. Their discovery opened up the field of unconventional superconductivity, proving that magnetism and superconductivity are not disconnected phenomena. This boosted an intensive work on these compounds, with quick progresses both in the theoretical and experimental fields. Many heavy fermion superconducting systems were discovered and new models (as the Anderson's large-degeneracy expansion) were developed for their interpretation. The phase diagram of heavy fermion materials was further enriched in 1994, with the observation of a zero-temperature quantum phase transition, i.e. a quantum critical point (QCP), in $CeCu_6$ [16].

1.1.2 The Doniach phase diagram

The phase diagram of HF (Figure 1.1) is governed by the competition between the Kondo screening and the RKKY interaction. Both effects depend on the exchange coupling J between f and conduction electrons and the density of states n around the Fermi level.

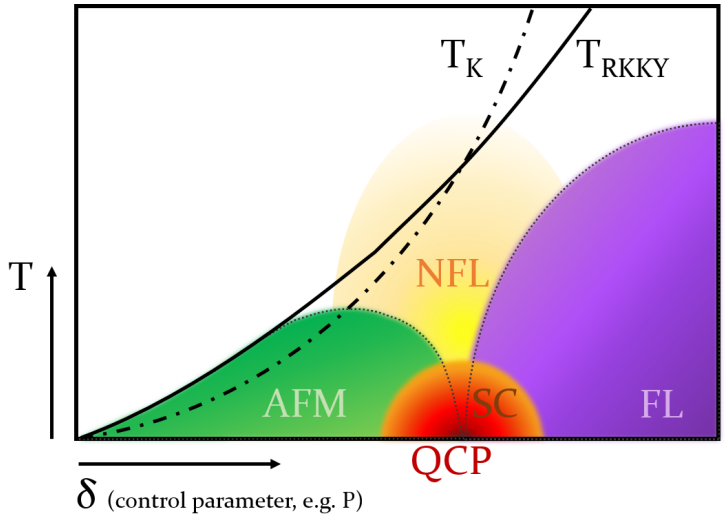

Figure 1.1: Qualitative illustration of the Doniach phase diagram. The different dependencies of T_K and T_{RKKY} on an external control parameter δ produce diverse ground states. An antiferromagnetic (AFM) ordering develops in the region where $T_{\mathrm{RKKY}} > T_K$, while for $T_{\mathrm{RKKY}} < T_K$ a paramagnetic Fermi liquid (FL) phase is formed. In between the two phases, a quantum critical point (QCP) can arise, in the vicinity of which exotic properties as non-Fermi liquid behaviour (NFL) and unconventional superconductivity may be found. Figure redrawn after Ref. [17].

The Kondo temperature, below which the f-electron magnetic moments are screened by the conduction electrons, has a strong exponential dependence

$$T_K \quad \propto \quad \exp(-1/(2Jn)) \; . \tag{1.1}$$

The Kondo screening of the magnetic moments would lead to a non-magnetic ground state, with localized singlet states formed by the antiferromagnetic coupling of f and conduction electrons. The RKKY interaction, on the other hand, favours a magnetic ordering of the localized moments mediated by oscillations of the conduction electrons' spin density. In absence of Kondo screening, it sets in below the temperature

$$T_{\mathrm{RKKY}} \quad \propto \quad J^2 n \; . \tag{1.2}$$

The RKKY ordering is the dominating effect at low values of Jn while when Jn is large the Kondo effect becomes relevant and reduces the actual ordering temperature. The magnetic ordering gradually disappears, leaving a paramagnetic ground state with strongly interacting electrons that can be described in terms of a so-called *Fermi liquid* (FL). This is the proper heavy fermion state, which is discussed in the next section. Between the two regimes, one

often reaches a quantum critical point (QCP), which is the indication of a phase transition taking place at the absolute zero. In the vicinity of the QCP, large quantum magnetic fluctuation arise, leading to non-Fermi liquid behaviour [18], i.e. deviations from the typical FL properties, and possibly to unconventional superconductivity [19].

The Doniach phase diagram in Figure 1.1 qualitatively illustrates the various possible behaviours of a heavy fermion system as a function of T and a parameter $\delta = Jn$. δ is the parameter usually varied in experiments, by applying hydrostatic pressure or chemical doping.

1.1.3 The heavy fermion state

The heavy fermion (HF) behaviour arises from the strong coupling of the f electrons to the conduction band, which causes a partial delocalisation of the f electrons and the formation of heavily-dressed quasiparticles. The coupling becomes effective below a characteristic temperature T^*, while at high temperatures the thermal fluctuations overcome the Kondo effect and the material acts like a normal metal with a paramagnetic behavior of the non-interacting localized moments. Lowering T, the localized moments start to be screened by the spins of the conduction electrons and a Kondo singlet forms at each site. This causes an increase of the electrical resistivity with decreasing T, until at T^* the resistivity suddenly drops, due to the development of phase coherence in the scattering channel [3]. This is due to the interaction, mediated by the conduction electrons, of the dense order of localized magnetic moment, which form a so-called *Kondo lattice*. The strongly coupled state between the f electrons and the conduction band causes an effective hybridization between the localized f and the itinerant states. As a result, the f electrons contribute to the Fermi surface in the HF state, as can be observed in Shubnikov-de Haas or de Haas-van Alphen experiments [3]. The characteristic temperature for the onset of the Kondo lattice state T^* is related to the single-ion Kondo temperature T_K. In the following, for simplicity, both temperatures will be referred to as T_K, to indicate in general the temperature range at which the Kondo effects start to be relevant.

Many properties of the HF state are explained by the Landau's *Fermi liquid* (FL) theory [20], which considers the electron correlations by starting from a non-interacting electron fluid and adiabatically turning on the interactions. This transforms the ground state of the Fermi gas into the ground state of the interacting system. The observed heavy quasiparticles can be described in terms of Landau quasiparticles, which differ from free electrons for their dynamics (i.e. they show an enhanced mass and a reduced magnetic moment).

At low temperature FLs show a linear dependence of the specific heat $C \propto \gamma T$ with enhanced values of γ, a quadratic dependence of the resistivity $\rho(T) \propto AT^2$ and a characteristic (and small) temperature dependence of the magnetic susceptibility [5, 21, 22], often saturating at high values (enhanced Pauli paramagnetism). Moreover, two scaling laws $\chi/\gamma = \text{const}$ [23] and $A/\gamma^2 = \text{const}$ [24] are also typical of the FL character of HF compounds.

In contrast, signatures of the non-Fermi liquid phase are a logarithmic dependence of the specific heat, a resistivity $\rho(T) \propto AT^n$ with $1 < n < 1.5$ and often a temperature dependence of the magnetic susceptibility $\chi(T) \propto \chi_0(1 - c(T/T_0)^{1/2})$, instead of the $\chi(T) \propto \chi_0(1 + aT^2 \log T)$ of the FL state [17].

1.1.4 Heavy fermion superconductivity and quantum criticality

If the antiferromagnetic ordering temperature is lowered to the absolute zero by the competition with the Kondo effect, a quantum critical point (QCP) is achieved. The QCP corresponds to a quantum phase transition from the antiferromagnetic to the paramagnetic state, that takes place at 0 K and can be induced, for example, by application of pressure. In the vicinity of the quantum phase transition, the amplitude and the coherence length of quantum magnetic fluctuations grows rapidly. Contrary to a classical finite-temperature phase transition, where the fluctuations are restricted to a small fraction of a reduced temperature scale, the critical behaviour is extended to a wide portion of the phase diagram and influence the material properties [25]. As a result, exotic phenomena as non Fermi liquid behavior [18] and unconventional superconductivity [19] may arise.

Two different magnetic QCP are possible [26, 27]. In the *spin density wave* model the antiferromagnetic order arises from a spontaneous spatial modulation of the spins of the heavy charge carriers, which exist on both side of the QCP. On the other hand, in the *Kondo breakdown* scenario the transition from the paramagnetic to the antiferromagnetic state is considered in terms of a local criticality, due to the dissolution of the Kondo singlets and a localization of the f electrons, with a consequent change of the Fermi surface. In this case, the heavy quasiparticles are therefore only present in the paramagnetic state.

Other quantum criticalities, of non-magnetic nature, are also possible and have been considered responsible of specific features of the heavy fermion superconductivity (SC). The superconducting phase of $CeCu_2Si_2$ exhibits a double-dome structure in the phase diagram, with maximal critical temperatures of $T_{c_1} = 600$ mK at $P_{c_1} = 0.45$ GPa and $T_{c_2} = 2$ K at $P_{c_2} \approx 4$ GPa [28, 29]. The two SC phases can be separated by Ge substitution of the Si atoms, indicating that they could be related to different causes [30]. Studies on $CeCu_2Ge_2$, which at ambient pressure is an antiferromagnet, linked the SC1 phase to a magnetic QCP.

On the other hand, the origin of SC2 is still a matter of debate. At first, critical valence fluctuations were proposed to provide the glue for superconductivity [28, 31]. In this model, the f electrons are supposed to enter in a weakly correlated phase, accompanied by a change in the Cerium f levels occupation, energy and degeneracy. This abrupt valence change has not been observed in experiment [32], but a variation of the crystal field splitting of the f levels has been found around $P \approx 4$ GPa [33]. Alternatively, LDA+DMFT calculations suggested an orbital transition between two crystal field levels with different hybridizations [34, 35]. The corresponding critical orbital fluctuations would be coupled with the itinerant charges, providing the glue for the Cooper pairs.

The discovery of HFSC, in the vicinity of an antiferromagnetic phase and in certain cases triggered by pressure, opened up the variegated field of unconventional superconductivity. In contrast to the classical BCS superconductors, *electronic* interactions are considered to drive the formation of the Cooper pairs. The involvement of the heavy f electrons in the pairing mechanism was confirmed by measurements of the specific heat, the London prenetration depth and the superconducting coherence length, all showing the large mass renormalization of the charge carriers [3].

1.1.5 Intermediate valence

In the previous treatment the f occupation has always been considered as (almost) integral (for Cerium ions $n_f \approx 1$), with the f electrons acting as localized moments. Depending on the respective energy of the f (E_f) and Fermi (E_F) levels, upon hybridization the f occupation may undergo a considerable change. Valence changes can be accompanied by changes in the system's properties, an example being the aforementioned SC phase related to critical valence fluctuations in $CeCu_2Si_2$.

As a matter of fact, both the Ce ion valence and the exchange integral J depend on the hybridization strength V and the distance between E_f and E_F. Following Ref. [4], one can relate the sample properties to n_f and J by redrawing the Doniach phase diagram in function of E_f (Figure 1.2). Considering that (in the limit of infinite on-site repulsion of the f electrons)

$$J \propto \frac{2V^2}{E_F - E_f} \ , \tag{1.3}$$

J increases when the f level approaches E_F. Of course this expression is not valid for $E_F - E_f \to 0$, but its qualitative tendency is still correct. Starting with $E_f \ll E_F$ (regime I in Figure 1.2), the deep f level is occupied by one electron ($n_f = 1$) and the corresponding low value of J will let the RKKY interaction win over the Kondo effect. As discussed above,

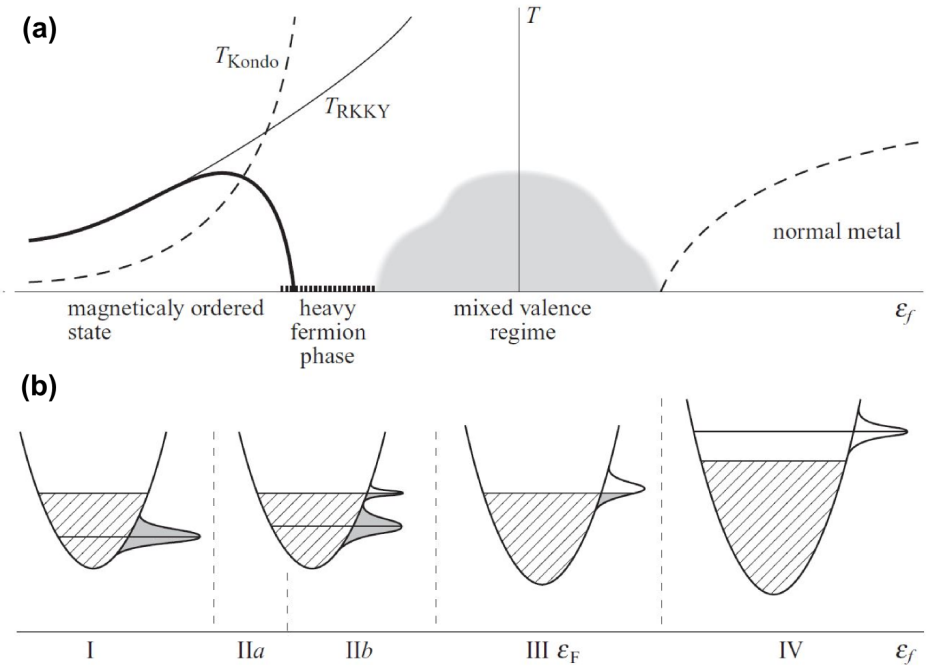

Figure 1.2: Figures reproduced from Refs. [4, 5] representing, as a function of E_f, (a) the extended Doniach phase diagram and (b) the energy scheme and density of state of the system.

an ordered magnetic phase with localized magnetic moments will form at low temperatures. By moving the f level closer to the Fermi level, the Kondo energy scale becomes relevant and the f magnetic moments are screened. This causes a decrease of the magnetic ordering temperature, which is eventually driven to zero. The Kondo interaction gives rise to a resonance peak in the density of states close to E_F, of width $\sim T_K$. The Kondo behaviour may initially coexist with the remaining magnetic ordering (region IIa in Figure 1.2) until the non magnetic HF liquid behaviour completely sets in. Since the f level is still relatively deep, its occupation is again close to one ($n_f \approx 1$).

When E_f approaches the Fermi level, i.e. $E_F - E_f$ becomes comparable with the f level broadening ($\Gamma = \pi N(E_F)V^2$, due to the hybridization) and its population decreases significantly. The Kondo lattice picture doesn't hold any longer and the new regime is labelled as *intermediate valence*. The properties of the ground state are still described by a Fermi Liquid behaviour, with moderately enhanced specific heat and magnetic susceptibility, which saturates for $T \to 0$. Since $E_F - E_f \to 0$, Equation 1.3 loses its validity, nonetheless the typical Kondo scale becomes very large in this regime, with $T_K \approx 10^3 K$ instead of the usual values $T_K \sim$ 1-10 K for the HF state.

The intermediate valence should be interpreted as a superposition of states with dif-

ferent distributions of the electrons between the f states and the conduction band, i.e. $|\Psi\rangle = a|f^1c^n\rangle + b|f^0c^{n+1}\rangle$, where c represents the conduction band. In presence of such a superposition of states, the system experiences quantum fluctuations among the different valence configurations and the average occupation n_f is given by the weights $|a|^2$ of each contribution. Referring to this picture, one also usually speaks of *mixed valence*.

To conclude the description of Figure 1.2, when $E_f > E_F$ the f states are eventually depopulated. The f electrons are completely transferred to the conduction band, all the interactions with the localized states disappear and the system enters a non magnetic metallic phase.

1.1.6 Significance of the 4*f* states

In this introductory section, the properties of heavy fermion systems, which include Cerium intermetallics, were presented with a general overview, without considering the detailed characteristics of the f levels involved. Instead, as one can imagine, the properties of f states are of fundamental importance for the determination of the interaction with the conduction band.

There are 7 f orbitals, i.e. solutions of the Schrödinger equation for the hydrogen atom with quantum number $l = 3$, each with two possibilities for the electron spin. Due to the intra-atomic (spin-orbit) and inter-atomic (crystal field) interactions the 14 one-electron f states are split in energy and, in presence of more than one f electron, the $e^- - e^-$ interactions further complicate the f energy scheme.

First of all, the splitting lifts the ground state degeneracy, which, for a Ce^{3+} ion in a (non-magnetic) crystal environment, can be 2, 4 or 6 depending on the specific crystal electric field. This simple consideration has already important consequences, since the results of many theoretical works, as the Anderson impurity large N expansion, depend on the f states' degeneracy. The size of the splitting should be introduced in the discussion too, because, when compared to the other typical energy scales of the system, it determines which f levels may actually take part in the interactions. Moreover, each f level is characterized by a different projection of the total angular momentum J_z, which gives the magnetic moment of the Ce ion. Since all the exotic phenomena presented above are driven by magnetism, the knowledge of the magnetic moment of the unhybridized ion provides much information about the magnetic interactions ruling the observed phenomena. Lastly, the unhybridized f states are highly anisotropic and their specific symmetry and charge distribution are very important for modeling the properties of heavy-fermion systems [36, 37]. Indeed, strongly anisotropic Fermi liquid behavior has been observed [38] and the crystal-field anisotropy is

supposed to influence the band structure, the Fermi surface [39] and even the formation of the SC state [40, 41, 42, 43].

Despite the efforts of the last 40 years, the experimental determination of the energy, symmetry and charge distribution of the f states is still a challenge and different techniques can lead to different conclusions. In this work, the new capabilities of Resonant Inelastic X-ray Scattering (RIXS) spectroscopy at the rare earth $M_{4,5}$ edges are shown to be ideal probes of the $4f$ levels and used for solving this old puzzle in prototypical cases.

1.2 Cerium $4f$ states in the free ion and in the crystal environment of solids

As just discussed, many fascinating and interesting phenomena arise in Cerium intermetallic compounds from the presence of $4f$ states and their strong interaction with the surroundings. The property of $4f$ levels (degeneracy, energy, symmetry...) are of great importance for the full understanding of the underlying physics. In this section, the Hamiltonian describing the electronic states in a Cerium ion is discussed, starting from the free ion and more and more adapting it to the specifics of Cerium intermetallic compounds of the 122 family, as those studied in this thesis. The arguments in this section apply as well to the description of the excited states that come into play in the spectroscopic techniques used to study the electronic levels of the Cerium ion and that will be discussed in the next section and in chapter 2.

1.2.1 Energy levels of the free ion

The central field approximation. The calculation of the energy levels of an atomic system is based on the Schrödinger equation

$$H\Psi = E\Psi. \tag{1.4}$$

Considering the atom as made up of a point nucleus of infinite mass and charge Ze, surrounded by N electrons, of mass m and charge $-e$, the systems' Hamiltonian is given by [44, 45]:

$$H = \sum_{i=1}^{N}(p_i^2/2m - Ze^2/r_i + \xi(r_i)\boldsymbol{l}_i \cdot \boldsymbol{s}_i) + \sum_{i>j=1}^{N} e^2/r_{ij}. \tag{1.5}$$

The first summation in the Hamiltonian considers only single-electron terms: (a) the kinetic energy of each (i-th) electron; (b) its potential energy in the field produced by the nucleus and (c) the spin-orbit interaction. The second summation, on the other hand, takes into account

the interactions acting between the electrons in the atom, modeled as a sum of electrostatic repulsions between two charges $-e$ at a time separated by a distance r_{ij}. This last term prevents the separation of the variables describing each electron, therefore an approximation is needed in order to solve the Schrödinger equation for many-electrons atoms. The repulsion cannot be neglected as small in the first place and subsequently treated as a perturbation, because, due to the large amount of electrons, its total effect can be comparable to the interaction between the electrons and the nucleus.

The *central field approximation* [46, 44] considers each electron as moving independently in the field of the nucleus plus a central field due to the charge distribution of the other electrons. In this way the most of the electronic repulsion is taken into account as an average potential screening the nucleus and the remaining part can be eventually treated as a perturbation. The Hamiltonian for the central field approximation which is the starting point of the calculation is given by:

$$H_0 = \sum_{i=1}^{N} (p_i^2/2m + U(r_i)) \tag{1.6}$$

where $-U(r)/e$ is the spherically symmetric effective potential. The remaining terms, i.e. the spin-orbit interaction and the deviations from the average potential can be treated as a perturbation

$$H_1 = H - H_0. \tag{1.7}$$

The solution of the approximated multi-electron Schrödinger equation

$$H_0\Psi = E^0\Psi \tag{1.8}$$

can now be expressed using single-electron wave functions ψ_{k_i}, that describe the independent motion of an electron in a central field $U(r)$, with k representing the set of quantum numbers (nlm_l). It is possible to separate the radial and angular part $\psi_k = R_{nl}Y_{lm_l}(\theta, \phi)$, where Y_{lm_l} are spherical harmonics [44] and R_{nl} a radial function depending on $U(r)$. The quantum numbers follow the usual notation, meaning that n is the principal quantum number of the electron shell, l the orbital angular momentum quantum number (subshell) and $m = m_l$ the magnetic quantum number. In the general potential $U(r)$, the energy values are degenerate only with respect to m_l, but there is no degeneracy with respect to l, the latter being a peculiarity of the Coulomb potential e^2/r and therefore present in the hydrogen atom (or any one-electron ion) only [45]. The spin of the electron is introduced by multiplying ψ by one of the two spin wave functions, depending on the two possible spin projections $m_s = \pm\frac{1}{2}$

along the z axis.

The full anti-symmetrized many-electron wave function $\Psi(K_1K_2....,K_N)$ is then given by the Slater determinant of the single-electron wave functions. The antisymmetry ensures that the Pauli exclusion principle is not violated.

$$\Psi(K_1,...,K_N) = \frac{1}{\sqrt{N!}} \begin{vmatrix} \psi_1(K_1) & \psi_1(K_2) & \cdots & \psi_1(K_N) \\ \psi_2(K_1) & \psi_2(K_2) & \cdots & \psi_2(K_N) \\ \vdots & \vdots & \ddots & \vdots \\ \psi_N(K_1) & \psi_N(K_2) & \cdots & \psi_N(K_N) \end{vmatrix} \tag{1.9}$$

where $K = (nlm_lm_s)$. The resulting functions are known as *zero-order wave functions*. Since the eigenvalues E^0 are degenerate with respect to m_l and m_s, the energy levels in the central field approximation are characterized by $(n_1l_1)(n_2l_2)...(n_Nl_N)$. The sequence of quantum numbers specifies the *electronic configuration* of the system.

Electrostatic and spin-orbit interactions. The zero-order wave functions make up the basis for calculating the first-order corrections due to the perturbation potential that represents the remaining electrostatic and spin-orbit interactions [47, 48, 45]. These terms are different for different states of the same configuration, which split into *levels* under their influence. In the first order perturbation theory each configuration is considered separately, assuming that the distances between the configurations are much larger than the splitting caused by the perturbation. [45] The energy corrections are obtained by calculating matrix elements of the kind:

$$\left\langle \Psi | H_1 | \Psi' \right\rangle \tag{1.10}$$

where H_1 represents the perturbation potential. The calculation details are described by Condon *et al.* [44] for both the spin-obit (single-electron operator) and the electrostatic (two-electrons operator) perturbations.

The separation of the wave function in an angular and a radial part is essential in the evaluation of the integrals. In particular, the radial part of the spin orbit interaction can be easily reduced to a parameter ζ_{nl}, that stands for the integral

$$\zeta_{nl} = \int_0^\infty R_{nl}^2(r)\xi(r)r^2dr. \tag{1.11}$$

The spin-orbit interaction of each electron will then be written in the form:

$$\zeta_{nl}\boldsymbol{l}\cdot\boldsymbol{s}. \tag{1.12}$$

The electrostatic part can be expressed in a series of Legendre polynomials. The angular dependence can be solved analytically and consists of integrals over spherical harmonics. Several selection rules can be applied for its simplification. The radial dependence is given by the so-called Slater integrals:

$$\begin{aligned} F^k(n_a l_a, n_b l_b) =& e^2 \int_0^\infty \int_0^\infty \frac{r_<^k}{r_>^{k+1}} R^2_{n_a l_a}(r_1) R^2_{n_b l_b}(r_2) {r_1}^2 {r_2}^2 dr_1 dr_2 \\ G^k(n_a l_a, n_b l_b) =& e^2 \int_0^\infty \int_0^\infty \frac{r_<^k}{r_>^{k+1}} R_{n_a l_a}(r_1) R_{n_b l_b}(r_2) R_{n_b l_b}(r_1) R_{n_a l_a}(r_2) {r_1}^2 {r_2}^2 dr_1 dr_2 \end{aligned} \tag{1.13}$$

which cannot be solved analytically. k denotes the order of the multipole components in the interaction, $r_< = min(r_i, r_j)$ and $r_> = max(r_i, r_j)$. The general formulation of the matrix element of the two-electron interaction is thus

$$\sum_i f_i F^i + \sum_i g_i G^i \tag{1.14}$$

where $F^i(f_i)$ and $G^i(g_i)$ are respectively the Slater-Condon parameters for the *radial (angular)* part of the direct and exchange parts of the electrostatic interaction [48]. The values for the Slater integrals and the spin-orbit parameters for a free ion can be determined with the code by R. D. Cowan [49] based on Hartree-Fock approximation. The effect of the electrostatic interaction is to split the electronic configurations into *levels*, the so-called Russel-Saunders (or LS) *terms*. The corresponding wave function is characterized by L, S, M_L and M_S, which are all good quantum numbers describing the atomic levels (respectively, total orbital and spin angular momentum of the atom, and their components along a quantization axis) as far as the spin-orbit interaction is not taken into account. The usual notation of *terms symbols* is ${}^{2S+1}X$, where X corresponds to a letter according to the value of L ($X = S, P, D, F...$ for $L = 0, 1, 2, 3...$). Since the terms with the same L and S have the same energy, the energy levels have a $(2L+1)(2S+1)$ degeneracy, that comes from all the possible combinations of M_L and M_S quantum numbers.

The spin-orbit interaction couples the spin and orbital angular momenta, that in principle are no more conserved independently. The total angular momentum $\boldsymbol{J} = \boldsymbol{L} + \boldsymbol{S}$ is still conserved and therefore J becomes a more convenient quantum number than L and S for the description of the energy levels.

In the Russel-Saunders (or LS) coupling picture, the spin orbit is considered as a perturbation on the energy levels determined by the electrostatic interaction. This picture holds always for light rare-earth atoms, while for transition metals it works only in absence of a crystalline field (whose effects are stronger than the spin-orbit). The energy corrections are given by the diagonal matrix elements of the spin orbit Hamiltonian calculated on the

LS terms, each of whom is split in a close group of levels, still characterized, to a good approximation, by S and L, and distinguished by different values of J [45]. The group as whole, indicated by ${}^{2S+1}X_J$, is called a *multiplet* and each level is $(2J+1)$-fold degenerate.

In the simple case of the ground state of a trivalent Cerium ion, only one electron is present in the $4f$ subshell, all the other subshells being filled and contributing only with a spherical potential in the central-field approximation Hamiltonian. The electron has $S = 1/2$ and $L = 3$, which can combine giving two different values of J, $|L - S| = 5/2$ and $L + S = 7/2$. Following the Hunds' rule, the level with the lowest J will be the ground state, described by the term ${}^2F_{5/2}$. The only parameter needed for the description of the electronic levels is here the $4f$ spin-orbit parameter. On the other hand, after the excitation of a core electron in the $4f$ subshell, as in X-ray Absorption Spectroscopy (XAS) or Resonant Inelastic X-ray Scattering (RIXS), the interactions that have to be considered are many more. The electrostatic repulsion between the $4f$ electrons, the electrostatic interaction between the core hole and the $4f$ electrons and the spin-orbit coupling for the core hole increase dramatically the number of the possible atomic levels. In the case of an excited $3d^9 4f^2$ configuration, the number of possible states is $10 \cdot \frac{14 \cdot 13}{2} = 910$, grouped in multiplets with the same L, S, and J but different M_J. Selection rules for dipole transition will restrict the number of possible excited states which nonetheless remains large.

The correct and full implementation of the electron-electron repulsion, with the *full multiplet atomic theory*, is of fundamental importance for the calculation of the spectra and interpretation of the experimental data. A discussion about the consequences of simplifications in the electron-electron Hamiltonian can be found in Ref. [47]. The Slater integrals to be considered in all the $3d^{10}4f^n \rightarrow 3d^9 4f^{n+1}$ transitions are given and discussed in Ref. [50].

1.2.2 Atoms in a crystal: the crystal electric field

Reduction of Slater integrals. In a solid, the presence of both "free" electrons and "fixed" ions introduce further modifications in the atomic Hamiltonian. First of all, the presence of the other charges partially screens the electron-electron repulsion. This affects in particular the monopole part of the repulsion [47], which anyway is usually not considered in multiplet calculations because it only affects the average energy of a configuration. On the other hand, the multiplet splitting within a configuration is experimentally found to be much less reduced from the free ion values. Experimentally, it has been noticed that a reduction of the Slater-Condon parameters to 80% of their Hartree-Fock values can take into account the screening effects. In the case of the presence of a $3d$ hole in a rare earth ion,

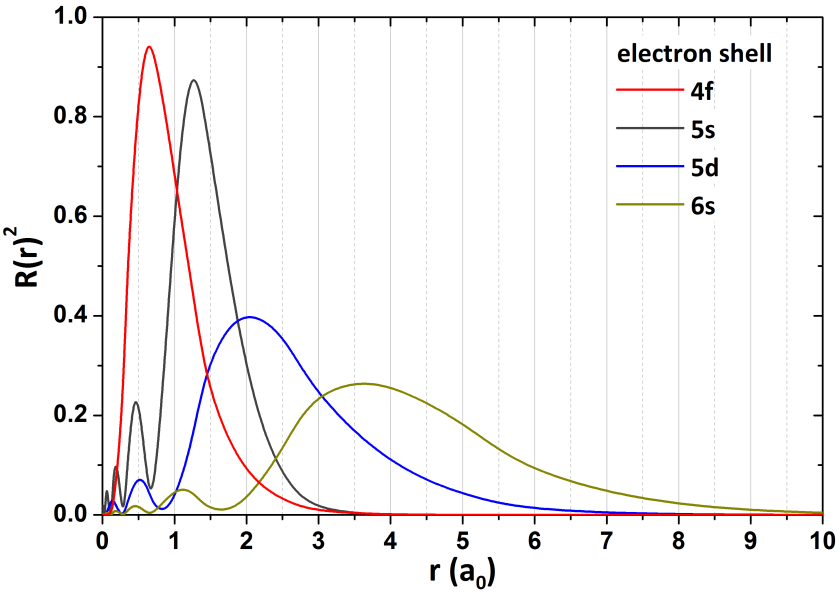

Figure 1.3: Square of the atomic radial wave functions for $4f$, $5s$, $5d$ and $6s$ states, as calculated by the Hartree-Fock method for Ce^{3+}. On the x-axis the distance r from the nucleus is given in units of the Bohr radius a_0. For comparison, in Cerium intermetallics of the 122 family, the a crystallographic axis is $\sim 4\mathring{A} \approx 8a_0$. Figure reproduced from Ref [5].

the reduction of the repulsion between the $3d$ hole and the $4f$ electrons is usually reduced to 60%, in order to reproduce the $3d \rightarrow 4f$ X-ray absorption spectra [51].

Crystal-field model. In addition to the average screening effect, the presence of the ions surrounding the atom leads to a further splitting of its $(2J+1)$-degenerate multiplet levels. This effect is small for electronic states of the $4f$ subshell because they are in general well localized in the ion and shielded by other electrons (see Figure 1.3). Therefore it can be treated as a perturbation. The overlap with the wave functions of the surrounding ions is negligible for $4f$ orbitals, while the shells with $n = 5, 6$ are much more affected by surrounding ions, with $5d$ and $6s$ electrons being involved in the bondings. This is the reason why the lanthanides lose first their $5d$ and $6s$ electrons upon ionization, so that Ce^{3+} is found with a $4f^1$ configuration in its ground state.

Since $4f$ wave functions do not participate significantly in the bondings, their interaction with the surrounding ions of a crystal can be modeled, to a good approximation, as an interaction with an electrostatic field, called the *crystal electric field (CEF)* [47, 52, 53, 54]. The CEF Hamiltonian can be written as:

$$H^{\mathrm{CEF}} = -e \cdot V_{\mathrm{CEF}}(r, \theta, \phi), \tag{1.15}$$

where V_{CEF} is the CEF potential. It is important to stress the *effective* nature of the CEF potential: the CEF-split states are given mostly by an anisotropic hybridization of the $4f$ states with the ligands' bands, therefore deviations from the CEF model, which depicts a single ion in a static electric field, are possible. [5]

There are of course some physical requirements for the CEF potential: first of all it must reflect the symmetry of the crystal. It is indeed the lowering of the symmetry, from the spherical environment of the free atom to the local point symmetry in the crystal, that lifts the $(2J+1)$ degeneracy of the multiplets. The lower the symmetry, the larger the number of CEF-split levels. To express considerations on the symmetry of the CEF potential, and to perform the calculations, it is particularly convenient to expand it in spherical harmonics:

$$V_{\mathrm{CEF}}(r,\theta,\phi) = \sum_{k=0}^{\infty}\sum_{m=-k}^{k} A_k^m r^k C_k^m(\theta,\phi), \tag{1.16}$$

where $C_k^m(\theta,\phi) = \sqrt{\frac{4\pi}{2k+1}} \cdot Y_k^m(\theta,\phi) = \sqrt{\frac{(k-m)!}{(k+m)!}} \cdot P_k(cos\theta) \cdot e^{im\phi}$ are the renormalized spherical harmonics, and $P_k(cos\theta)$ the Legendre polynomials. A_k^m are the coefficients of the expansion. This expansion is possible as long as the overlap with ligands is neglected for $4f$ wave functions, so that V_{CEF} satisfies Laplace's equation. [55] To calculate the CEF states' energies as a first order perturbation, one has to evaluate the matrix elements on the basis of $\psi_k = R_n^l Y_l^m(\theta,\phi)$:

$$H_{i,j}^{\mathrm{CEF}} = -e\sum_{k=0}^{\infty}\sum_{m=-k}^{k} A_k^m \left\langle R_{n_i}^{l_i}(r)|r^k|R_{n_j}^{l_j}(r)\right\rangle \left\langle Y_{l_i}^{m_i}(\theta,\phi)|C_k^m(\theta,\phi)|Y_{l_j}^{m_j}(\theta,\phi)\right\rangle. \tag{1.17}$$

The integrals over the radial part $\left\langle R_{n_i}^{l_i}(r)|r^k|R_{n_j}^{l_j}(r)\right\rangle$ can, for a free ion, be calculated with the Hartree-Fock approximation using Cowan's code [49], while the integrals over spherical harmonics can be solved analytically; they are usually re-written using $3j$ symbols [49]:

$$\left\langle Y_{l_i}^{m_i}(\theta,\phi)|C_k^m(\theta,\phi)|Y_{l_j}^{m_j}(\theta,\phi)\right\rangle = (-1)^{m_i}\sqrt{(2l_i+1)(2l_j+1)}\begin{pmatrix} l_i & k & l_j \\ 0 & 0 & 0\end{pmatrix}\begin{pmatrix} l_i & k & l_j \\ -m_i & m & m_j\end{pmatrix}. \tag{1.18}$$

where the $3j$ are defined as:

$$\begin{pmatrix} j_1 & j_2 & j_3 \\ m_1 & m_2 & m_3\end{pmatrix} \equiv \frac{(-1)^{j_1-j_2-m_3}}{\sqrt{2j_3+1}}\langle j_1 m_1 j_2 m_2|j_3 -m_3\rangle. \tag{1.19}$$

It is now possible to use some properties in order to reduce the number of CEF parameters needed to fully describe the Hamiltonian. The triangular inequality of $3J$ symbols imposes that only matrix elements with $k \leqslant l_i + l_j$ can be non-vanishing, therefore only the CEF

parameters A_k^m that respect this restriction will affect the CEF levels. Furthermore, $k+l_i+l_j$ has to be even to have a non-zero expectation value, otherwise the angular part would consist of an integral over an odd function, which vanishes. Symmetry conditions on the V_{CEF}, which has to reflect the site symmetry of the rare earth ion, further reduce the number of useful A_k^m parameters. This restriction is introduced because H^{CEF} must be invariant under the point groups' symmetry operations. For example, if the high symmetry axis has q-fold rotational symmetry, V_{CEF} has to fulfill the condition $V_{\mathrm{CEF}}(r,\theta,\phi) = V_{\mathrm{CEF}}(r,\theta,\phi+\frac{2\pi}{q})$. This condition on the angular part of V_{CEF} translates into $e^{im\phi} = e^{im(\phi+\frac{2\pi}{q})}$, that is true if $m = N \cdot q$ with $N \in \mathbb{Z}$. This condition on m in the CEF Hamiltonian directly implies that the CEF can only mix states with $\Delta J_z = q$ [56].

Further conditions on the A_k^m allow to simplify the parametrization [57, 58]. For example, the requirement of an hermitian Hamiltonian imposes $A_k^m = (-1)^m (A_k^{-m})^*$, so that it is sufficient to determine the parameters A_k^m with $m \geqslant 0$.

Crystal-field parameters. In most cases, the A_k^m are considered as free parameters and are chosen in order to fit experimental data [47, 53, 55]. No assumptions are made on the potential, other than the ones dictated by symmetry. Moreover, the parameters A_k^m are always multiplied by the radial integral $\left\langle R_{n_i}^{l_i}(r)|r^k|R_{n_j}^{l_j}(r)\right\rangle$. The calculation of the integral with an atomic Hartree-Fock based method may lead to wrong expectation value, because the radial wave functions may be different for a free atom and an atom in a solid. To avoid this problem, the radial expectation values is included in the free phenomenological parameter, defining:

$$\check{A}_k^m = A_k^m \left\langle R_{n_i}^{l_i}(r)|r^k|R_{n_j}^{l_j}(r)\right\rangle. \tag{1.20}$$

This is the notation that will be used in this thesis. It must be said that in literature many other conventions can be found to express the CEF parameters, a full list and explanation of which is given in Ref [53]. The *Stevens parameters* B_k^m are by far the most common in literature. These parameters result directly from the *Stevens approximation* [59], which deserves some explanation.

Since the splitting of the LSJ multiplets produced by the spin-orbit coupling is much larger than the effect of the CEF potential, one may assume that the CEF will only be able to mix states within the same LSJ multiplet (but with different values of J_z). This approximation considerably reduces the size of the basis on which the matrix elements of H^{CEF} need to be evaluated, simplifying the calculations. The study of the CEF is usually performed in order to know the properties of the ground state and of the first low-energy excitations, therefore one can restrict the calculation to the lowest LSJ multiplet. J can be

then considered as a good quantum number [5]. Stevens, after expressing V_{CEF} as sums of (non-normalized) tesseral harmonics in the Cartesian coordinates, showed that the sum of polynomials in x_i, y_i, z_i can be replaced by a sum of polynomials in $\boldsymbol{J}_x$, $\boldsymbol{J}_y$, $\boldsymbol{J}_z$ operators, which transform likewise under symmetry operations [52]. The new operators are much more convenient because they act on the basis as a whole, while the x_i, y_i, z_i polynomials acted on a particular one-electron wave function [52]. After the conversion, Stevens Hamiltonian is expressed as:

$$H^{\mathrm{Stevens}} = \sum_k \sum_{m=0}^{l} B_k^m O_k^m(J). \tag{1.21}$$

O_k^m are the *Stevens operators* and B_k^m the *Stevens parameters*, to be determined experimentally. To understand the relations between B_k^m and $\check{A}_k^m$ parameters, one must follow backwards the Stevens method. The Stevens parameters are defined as [59, 53] :

$$B_k^m = \tilde{A}_k^m \left\langle r^k \right\rangle \langle \Theta_k \rangle. \tag{1.22}$$

Where $\left\langle r^k \right\rangle$ is a short notation for the usual expectation value of the radial part of the matrix element and $\langle \Theta_k \rangle = \langle J | \Theta_k | J \rangle$ is a prefactor introduced during the x_i, y_i, $z_i \rightarrow \boldsymbol{J}_x$, $\boldsymbol{J}_y$, $\boldsymbol{J}_z$ substitution. These prefactors were tabulated by Stevens [59] and depend only on k and J, which in this approximation is a good quantum number, therefore constant for a given multiplet. $\tilde{A}_k^m$ are the coefficients of the expansion of the CEF potential:

$$V_{\mathrm{CEF}}^{\mathrm{Stevens}} = \sum_l \sum_{m=0}^{l} \tilde{A}_k^m r^k f_k^m(x, y, z). \tag{1.23}$$

$f_k^m(x, y, z)$ are tesseral Harmonics in their Cartesian expression, without any numerical normalization factor. Re-introducing this prefactor as $p_{k,m}$ (tabulated in Ref. [53]) and expressing the tesseral harmonics as sum of spherical harmonics, it is easily found that [58]:

$$\begin{aligned} B_k^m &= \check{A}_k^m p_{k,m} \sqrt{\frac{4\pi}{2k+1}} \langle \Theta_k \rangle \quad \text{if } m = 0 \\ B_k^m &= \check{A}_k^m p_{k,m} \sqrt{\frac{8\pi}{2k+1}} \langle \Theta_k \rangle \quad \text{if } m \neq 0. \end{aligned} \tag{1.24}$$

The calculations in this thesis were performed using the SolidStatePhysics package for Mathematica by Maurits Haverkort. There the prefactors $\lambda_{k,m} = p_{k,m}\sqrt{\frac{4\pi}{2k+1}}$ are defined in the documentation as *Stevens prefactors*.

The Stevens notation is extensively used in all the techniques that limit their analysis to the lowest J multiplet, as Inelastic Neutron Scattering (INS) and many indirect techniques as magnetic susceptibility. In a RIXS spectrum, on the other hand, features coming

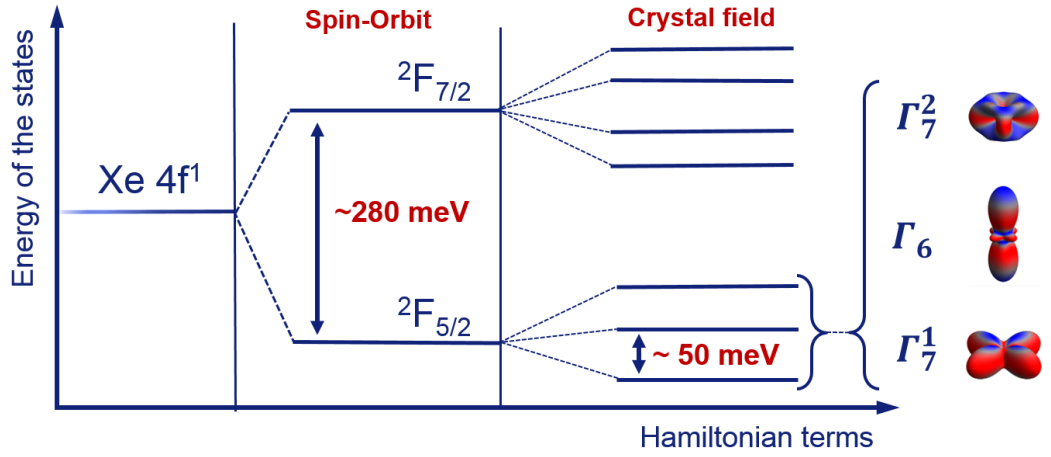

Figure 1.4: Energy splitting of the $4f^1$ configuration in tetragonal symmetry and the charge distribution of each CEF state arising from the ${}^2F_{5/2}$ multiplet.

from different LSJ multiplets will usually contribute. In this case, the J-dependent B_k^m parameters are not appropriate and one should use the J independent $\check{A}_k^m$ notation instead.

States of Ce^{3+} in tetragonal crystal field. The specific case of the ground state of a Ce^{3+} ion can now be discussed. As stated above, we can focus on one configuration ($4f^1$) and split its LS terms by perturbating them with spin-orbit coupling first and then with the CEF. Since there is one electron in the $4f$ subshell, $L = 3$, $S = 1/2$ and the only possible term symbol is ${}^2F$. Spin-orbit coupling splits levels with different J values ($J = |L \pm S| = 5/2, 7/2$) leading to ${}^2F_{5/2}$ and ${}^2F_{7/2}$. The Hund's rules set that for a less-than-half-filled subshell, the ground state is the one with the lowest J values, i.e. ${}^2F_{5/2}$. The $(2J+1)$ degeneracy of each multiplet is lifted by the CEF. The *Kramers' theorem* states that in the absence of a magnetic field the energy levels of a system with an odd number of fermions (here, electrons) can at most be split into double-degenerate levels, the so-called Kramers' doublets. The Cerium intermetallic compounds discussed in this thesis are of the 122 family, which exhibits tetragonal D_{4h} symmetry that completely splits the ${}^2F_{5/2}$ and ${}^2F_{7/2}$ multiplets in 3 and 4 Kramers' doublets respectively.

The CEF parameters determine the energy of the CEF levels and the J_z mixing of the CEF wavefunctions. Which of the $\check{A}_k^m$ have to be used is set by the constraints outlined before. Since $L = 3$, we have that $k \leqslant l_i + l_j = 3 + 3 = 6$ and the requirement on $k+l_i+l_j =$ even implies that $k =$ even. Therefore $k = 0, 2, 4, 6$ are the possible values of k for a $4f^1$ configuration. The harmonic functions with $k = 0$ only have a spherical contribution to the potential and don't affect the splitting, thus their effect is usually neglected and

is included in the effective spherically symmetric potential. The presence of the four-fold rotational axis imposes $m = 0, 4$. This implies that the CEF Hamiltonian will mix in the lowest ${}^2F_{5/2}$ multiplet, $J_z = \pm 5/2$ with $J_z = \mp 3/2$. $J_z = \pm 1/2$, on the other hand, stays a pure J_z states as long as the inter-multiplet mixing is neglected, otherwise a small mixing with $J_z = \mp 7/2$ is in principle possible.

Limiting the analysis to the ${}^2F_{5/2}$ multiplet and neglecting the inter-multiplet mixing, another condition imposes that $k \leqslant 2J = 5$ [60], letting us discard the terms with $k = 6$. We are therefore left with the three parameters $\check{A}_2^0$, $\check{A}_4^0$ and $\check{A}_4^4$ to model the effects of CEF on the ${}^2F_{5/2}$ multiplet[1].

The CEF wave functions result from an admixture of different J_z states within the same multiplet and can therefore be expressed as linear combination of the $|J = 5/2, J_z\rangle \equiv |J_z\rangle$ wave functions. After applying the CEF Hamiltonian on the $|J = 5/2, J_z\rangle$ basis, the resulting states are given by:

$$\begin{aligned} \Gamma_7^1 &= \frac{1}{(a^2+b^2)}(a|\pm 5/2\rangle + b|\mp 3/2\rangle) \\ \Gamma_7^2 &= \frac{1}{(a^2+b^2)}(b|\pm 5/2\rangle - a|\mp 3/2\rangle) \\ \Gamma_6 &= |\pm 1/2\rangle, \end{aligned} \tag{1.25}$$

where the double group Bethe's notation Γ_k is used to label the states according to their symmetry. The relative energy of the CEF levels and the mixing of the J_z wave functions can be expressed as a function of $\check{A}_2^0$, $\check{A}_4^0$ and $\check{A}_4^4$. In particular, we have that

$$\begin{aligned} a &= 5\sqrt{14}\check{A}_4^4 \\ b &= 18\check{A}_2^0 - 10\check{A}_4^0 - \sqrt{4(9\check{A}_2^0 - 5\check{A}_4^0)^2 + 350\check{A}_4^{4\,2}}, \end{aligned} \tag{1.26}$$

and the weight α of the component $J_z = |\pm 5/2\rangle$ in the state Γ_7^1 is given by:

$$\alpha = \frac{a}{\sqrt{a^2+b^2}} = \frac{5\sqrt{14}\check{A}_4^4}{\sqrt{350\check{A}_4^{4\,2} - \left(18\check{A}_2^0 - 10\check{A}_0^4 - \sqrt{4(9\check{A}_2^0 - 5\check{A}_4^0)^2 + 350\check{A}_4^{4\,2}}\right)^2}}. \tag{1.27}$$

The relative energies of the states are:

$$\begin{aligned} E_{\Gamma_7^1} &= \frac{1}{105}\left[(-12\check{A}_2^0 - 5\check{A}_4^0) - 2\sqrt{4(9\check{A}_2^0 - 5\check{A}_4^0)^2 + 350\check{A}_4^{4\,2}}\right] \\ E_{\Gamma_7^2} &= \frac{1}{105}\left[(-12\check{A}_2^0 - 5\check{A}_4^0) + 2\sqrt{4(9\check{A}_2^0 - 5\check{A}_4^0)^2 + 350\check{A}_4^{4\,2}}\right] \\ E_{\Gamma_6} &= \frac{8}{35}\check{A}_2^0 + \frac{2}{21}\check{A}_4^0. \end{aligned} \tag{1.28}$$

[1]For a complete description of the splitting of the ${}^2F_{7/2}$ multiplet, we would need to add $\check{A}_6^0$ and $\check{A}_6^4$ to the set.

It can be easily noticed that $E_{\Gamma_7^1} \leqslant E_{\Gamma_7^2}$. Apart from this, these expressions do not provide any further information about the order of the states in energy. In our strictly phenomenological approach, this needs to be determined with experiments.

The $\check{A}_4^4$ parameter is always present elevated to the power of two in (1.28), therefore its sign does not affect the energy splitting. However, it affects the sign of α and this has consequences on the orientation of the states with respect to the crystallographic axes. This will be discussed in more detail in section 4.3.

1.3 Experimental determination of the crystal field acting on the $4f$ states

Several techniques have been used over the years to investigate the CEF effects in rare earth ions, depending on the studied material class and the specific physical property of interest. Each of these methods comes with some limitations and the gained information on the CEF is usually only partial and does not necessarily agree with the results obtained by another method. In this section, the established techniques are briefly reviewed, in order to be able to compare their peculiarities to those of Resonant Inelastic X-ray Scattering, discussed in the next chapters.

1.3.1 Classic approaches

The CEF splitting affects various physical properties of the rare earth compounds, therefore different physical quantities can be measured and related to the CEF scheme.

The most straightforward methods to probe the energy of the CEF-split levels involve *optical* (*absorption* and *fluorescence*) measurements [61, 62, 63], but these are feasible only on transparent samples, while in metallic systems the signal coming from $4f - 4f$ transitions would be in general overwhelmed by that of other excitations occurring in the same energy range. Since a simple and direct optical measurement of the CEF-levels' splitting is not doable, many indirect measurements arose to study the CEF scheme in rare earth compounds.

The majority of the methods exploit the magnetic properties of the rare earth ion. *Electron Paramagnetic Resonance* (EPR) or *Electron Spin Resonance* (ESR) [64, 65], measuring the Zeeman splitting of a given CEF-level, can study the properties of the ground state wave function and its magnetic field-induced mixing with other states, but it is suitable only for very small CEF splitting, mostly on S-states ions [66, 52]. The so-called *hyperfine methods*, as *Nuclear Magnetic Resonance* (NMR), *Mössbauer spectroscopy* and *Muon Spin Resonance*

(μSR) study the (magnetic) effect of the CEF-ground state on the nucleus [65], but, being rather indirect techniques, may often not give a unique set of CEF parameters [66].

Magnetic susceptibility and specific heat

Magnetic susceptibility (χ) measurements have a more direct insight into the magnetic properties of the ground state and are more commonly used for Cerium intermetallic compounds. The electron in the $4f$ sub-shell is responsible for the atomic magnetic moment μ, that can be related to the J_z mixing of the occupied states. The projection of μ along a direction i is given by $\mu_i = -\mu_B g_J J_i$ and, in presence of an applied magnetic field $\boldsymbol{B}^{ext} = B_i^{ext}$, an energy term $\boldsymbol{B}_{ext} \cdot (\boldsymbol{L} + 2\boldsymbol{S}) = g_J \boldsymbol{B}^{ext} \cdot \boldsymbol{J} = g_J B_i^{ext} J_i$ is added in the atomic Hamiltonian. The magnetization of a (paramagnetic) sample at finite temperature T can then be calculated via a Boltzmann statistic, by averaging the magnetic moment of each level, weighted with the respective Boltzmann factor. Since in Cerium intermetallics of the 122 family the tetragonal symmetry sets a natural quantization axis, measurements with $B \parallel [100]$ and $B \parallel [001]$ show a magnetic anisotropy, which is directly related to the ground state's J_z value. Moreover, the temperature dependence of $\chi_i(T) = \frac{\partial M_i(T)}{\partial H_i}$ provides information about the thermally occupied excited states. This method has again the drawback of being indirect: in the data analysis, indeed, the CEF-parameters are varied until the calculated curve agrees with experiments, but different sets of parameters, yielding different energy splittings of the $4f$ levels may fit the same curve. Furthermore, at low temperatures, the Kondo effect and the antiferromagnetic RKKY interaction strongly affect both the magnetic anisotropy and the temperature dependence of $\chi(T)$. Their effect can be considered in simulations by introducing some further parameters, but this implies further uncertainty in the data interpretation. [67, 68, 69]

Another indirect way to determine the CEF-levels is via *specific heat* measurements. Starting with all the ions in their ground state at the absolute zero, upon increasing T higher energy levels are thermally populated and therefore more energy must be provided to the sample. At higher temperatures, one can imagine that all the states are equally populated and no further energy is required for the CEF excitations. The magnetic specific heat is therefore expected to show a maximum at a temperature such that the thermal energy becomes comparable to the separation of the levels (usually at $T \lesssim 1/2\Delta E_{\mathrm{CEF}}$). This phenomenon is referred to as *Schottky anomaly* [55, 52, 72]. The contribution of phonons to the total specific heat is usually considered as independent, and either neglected or estimated from non-magnetic parent compounds. The accuracy of the measurements is therefore limited by the presence of spin-phonon interactions. In addition to this, Kondo

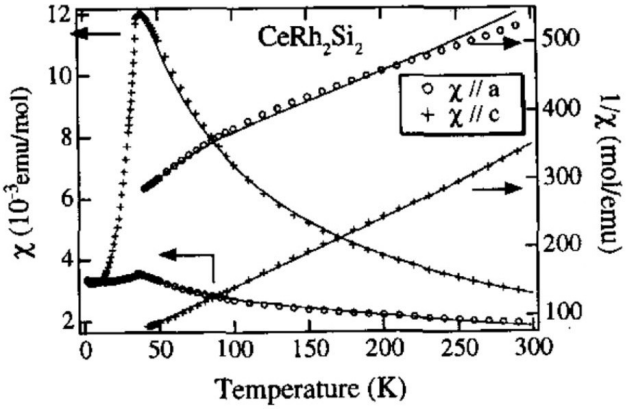

Figure 1.5: Magnetic susceptibility data for $CeRh_2Si_2$, reproduced from Ref. [70]. The fit of the data lead to a CEF scheme Γ_7 - Γ_6 -Γ_7, with 31 and 80 meV splittings. The CEF-related part is the one at high temperatures (> 100 K), while the decreasing of χ at low temperatures has to be ascribed to magnetism and other phenomena. Note that another magnetic susceptibility study, in Ref. [71], gave 27 and 59 meV splittings and a Γ_7 - Γ_7 - Γ_6 scheme.

and exchange effects among rare earth ions further distort the specific heat curves and their contribution has to be considered. Figure 1.6 shows the $4f$ part of the specific heat in $YbIr_2Si_2$ after subtraction of the specific heat measured from the non-magnetic reference $LuIr_2Si_2$. The data is compared to calculations of the magnetic part of the specific heat including the Kondo effect for two different CEF schemes obtained from inelastic neutron scattering and photoemission spectroscopy [73].

Inelastic neutron scattering

Inelastic Neutron Scattering (INS) [52, 66, 74, 75] can measure the splitting between the $4f$ levels directly and has become the dominant method for studying crystal fields in rare earth intermetallic compounds. In such an experiment monochromatic neutrons are scattered from the sample and are analysed according to their energy and momentum, determining the energy- and momentum $\boldsymbol{Q}$ transfer. The differential cross section for a transition between two CEF-split states is (in dipole approximation) proportional to $|\langle j|J_\perp|i\rangle|^2$, where $J_\perp$ is the $\boldsymbol{J}$ component perpendicular to the scattering vector $\boldsymbol{Q}$, the transition being due to a magnetic interaction. Transitions between two CEF-levels are visible in the INS spectrum as peaks in correspondence to the energy transfer required for the excitation, that is the energy of the CEF-splitting. Moreover information about the ground state's spatial distribution is contained in the intensity ratios of the quasielastic and inelastic excitation lines.

The magnetic scattering is often superimposed by phonon contributions which are complicated to correct for. In principle one can separate the magnetic and nuclear scattering by

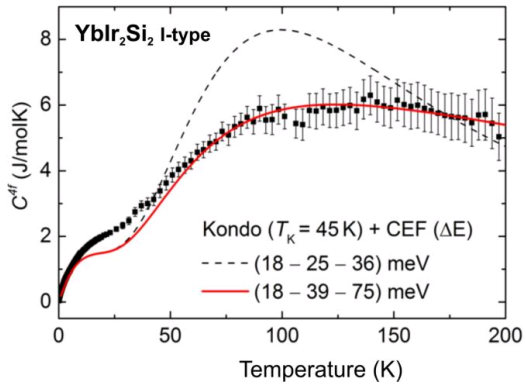

Figure 1.6: Magnetic part of the specific heat of $YbIr_2Si_2$ as function of temperature. The data is compared to calculations for two CEF schemes obtained with photoemission spectroscopy (solid line) and inelastic neutron scattering (dashed line). Figure reproduced from [73].

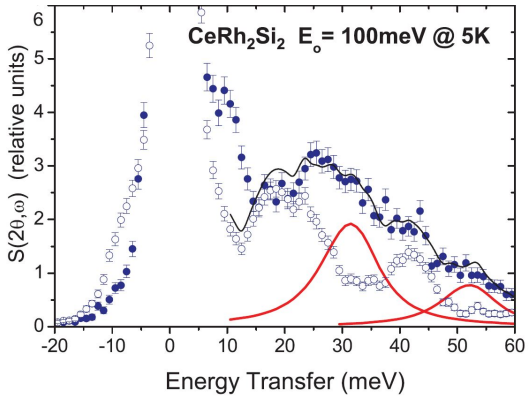

Figure 1.7: INS data for $CeRh_2Si_2$, reproduced from Ref. [51]. The open dots represent the phonon scattering, scaled from the high to low scattering angles. The red lines represent the signal attributed to CEF peaks. Combining these data with XAS measurements (Figure 1.9), a CEF scheme Γ_7^1-Γ_7^2-Γ_6, with 30 and 52 meV splittings, was obtained.

using polarised neutrons and analysing their polarisation after the scattering [76]. However, this is usually not performed because of the limited intensities. The most used method to separate the two contribution relies on the different behavior of the two scattering processes when the momentum transfer and temperature are varied. One can also obtain information on the phonon spectra by measuring a nonmagnetic reference compound with a similar crystal structure. This procedure, even if well established, is very difficult to apply on strongly correlated electron systems. The electron-electron interactions cause the CEF-transition peaks to be very broad and they can be lost in the complex phonon background.

Another drawback of INS is the limited energy range that can be probed. For energy losses larger than $\sim$ 60meV, the contribution of multiple (phonon) scattering processes becomes very large and covers the CEF peaks. Therefore splittings larger than $\sim$ 60meV

cannot be observed.

Finally, the count rate is always an issue in INS. In order to increase the signal, large samples are required, but it is not always possible to grow single crystals of centimeter-size. Powder are therefore used, but this means a partial loss of the information coming from the peaks' intensity. Furthemore, many elements are strong absorber of neutrons, therefore INS experiments in some compounds are practically impossible.

1.3.2 Recently established methods

X-ray absorption spectroscopy

In X-ray Absorption Spectroscopy (XAS) X-ray photons excite an electron from a filled core level to an empty valence one, leaving a core hole. The amount of photons that interacted with the sample is measured by comparing the flux transmitted by the sample with the incident one or by measuring the electrons (Total Electron Yield) or photons (Fluorescence Yield) emitted during the recombination of the core hole. XAS spectra are labelled depending on the core level excited: its principal quantum number ($n = 1, 2, 3, 4...$) is replaced by a letter (K, L, M, N...) and a number is added to represent, in order of increasing energy, the spin-orbit-split subshells. To study the properties of lanthanide ions $3d_{3/2,5/2} \rightarrow 4f$ and $4d_{3/2,5/2} \rightarrow 4f$ transitions are used, corresponding to $M_{4,5}$ and $N_{4,5}$ *edges*, which are both in the soft-X-ray range.

The transition from an initial state i to a final state f is governed by the Fermi's golden rule: $|\langle f|T|i\rangle|^2$, where T is the transition operator. In the case of λ-polarised soft X-rays interacting with a core electron, the operator can be well approximated as a dipolar interaction $T \propto \boldsymbol{e}_{\boldsymbol{k}\lambda} \cdot \boldsymbol{p}$. Fermi's golden rule corresponds to an integral over the whole space, which is not zero only for an even integrand. Since the dipole operator T is odd, the initial and final state must have different parity to have a non-vanishing integral, i.e. a dipole-allowed transition. By applying these symmetry considerations, together with the conservation of angular momentum and spin (photons carry an angular momentum 1 and no spin) the dipole selection rules are found: $\Delta l = \pm 1$; $\Delta j = 0, \pm 1$; $\Delta m_l = 0, \pm 1$; $\Delta m_s = 0$; $\Delta L = 0, \pm 1$; $\Delta S = 0$; $\Delta J = 0, \pm 1$ but no $J = 0 \rightarrow J = 0$ transitions. The notation for the quantum numbers is the usual.

The integral is also very dependent on the light polarisation, i.e. the orientation of the dipolar electric field with respect to the initial and final wavefunctions. The angular and polarisation dependencies give rise to dichroism in X-ray absorption spectra, meaning that spectra acquired with different light polarisations will be different. This effect is used to study the magnetic properties of the ions (mostly with circular light polarisation), or the

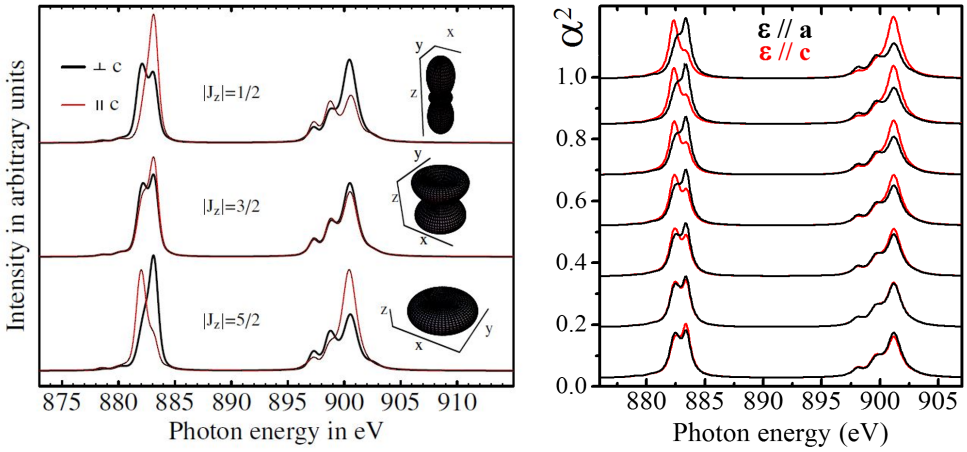

Figure 1.8: Left: Figure taken from Ref [81], showing the dichroism of XAS spectra in the case of pure J_z states (depicted in the insets) as ground wavefunctions for the $4f$ electron. Right: calculated spectra for a Γ^7 ground state, for various values of the α^2 mixing parameter (see section 4.2.2 for more information). To observe the XLD, XAS spectra with light polarisation $\epsilon \parallel c$ and with $\epsilon \parallel a \perp c$ are compared, a and c representing the crystallographic axes of the tetragonal unit cell.

orbital anisotropy in the ground state (linear polarisation). The first known study addressed to the investigation of $4f$ states in rare earth intermetallic compounds via X-ray Absorption Spectroscopy was performed on $CeRh_3B_2$ in the nineties. Crystal-field-related dichroism was observed in the calculated [77] and measured [78] spectra. Unfortunately, the model employed for the data interpretation was applicable only for the rather large CEF splitting of $CeRh_3B_2$ and lead to a much too high Kondo temperature [79]. Moreover, the crystal field symmetry was not fully taken into account [80].

Recently, Hansmann *et al.* [79] conceived a simple and powerful method to study the $4f$ ground wavefunction that stimulated a comeback for this technique to probe the CEF in rare earth intermetallics. With a single-ion approach, justified by the fact that usually $E_{Kondo} \ll E_{CEF}$, they observed that the $M_{4,5}$ spectra calculated supposing pure J_z states for the $4f$ electrons show defined polarisation dependences. This polarisation dependence, or X-ray Linear Dichroism (XLD), strongly depends on the ground state wavefunction's J_z (Figure 1.8).

The idea is to fit the experimental spectrum with an incoherent sum of the spectra simulated for pure J_z states. The resulting coefficients of the sum give the J_z mixing of the $4f$ electron ground state. Considering a Γ_7 ground wavefunction, given by an admixture $\alpha|\pm 5/2\rangle + \beta|\mp 3/2\rangle$, Figure 1.8 illustrates the spectra obtained with this method for various

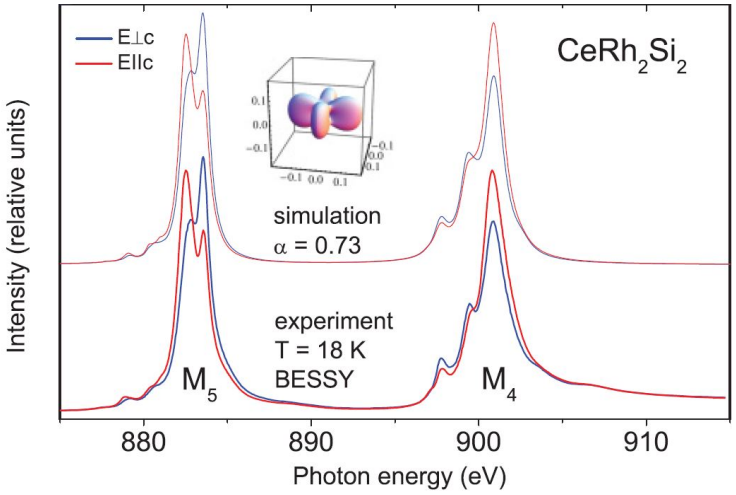

Figure 1.9: XAS data and simulations for $CeRh_2Si_2$, reproduced from Ref. [51]. Calculations with a Γ_7 ground state $|\alpha| = 0.73$ reproduce the experimental spectra. The order of the levels obtained from these data, combined with those of Figure 1.7 was Γ_7^1 - Γ_7^2 -Γ_6, with 30 and 52 meV splittings.

values of α^2. It should be noted that the lifetime of the excited $3d$ hole is $\tau < 10^{-15}$s, giving a linewidth broadening $\Delta E > 0.5\text{eV} \gg \Delta E_{\text{CEF}}$: the observation of the ground state properties is possible even if the CEF-related peaks are hidden in the spectral broadening.

This method provides a very good description of the ground state wave function, but information about the symmetry and energy of the higher energetic levels is missing. In principle, a temperature dependence of the XAS due to thermal population of excited states may provide an estimate of the energy of higher levels if the splittings are small enough. Due to the only limited information provided by XAS there is usually an uncertainty on the CEF scheme left and other measurements, such as INS, are needed for a complete description.

Some difficulties may also arise from the fact that the mixed valence of the Ce ion leads to an extra spectral component originating from the Ce^{4+} contribution, partly superimposed to the Ce^{3+}, that needs to be considered separately to the dichroic effects [82, 83]. Moreover, to study the ground state, experiments must be performed at low temperatures $k_BT \ll \Delta E_{\text{CEF}}$ to avoid the thermal population of higher levels, but at these low temperatures the sample may be in an antiferromagnetic phase. The magnetic ordering is another cause of dichroism in the absorption spectra [84, 83] and it needs to be identified apart from the ground state mixing effects.

Lastly, if the XAS signal is detected as TEY, due to the short mean free path of electrons in condensed matter, the signal is given by a portion of the sample close to the surface, which must be accurately prepared in order to avoid artefacts.

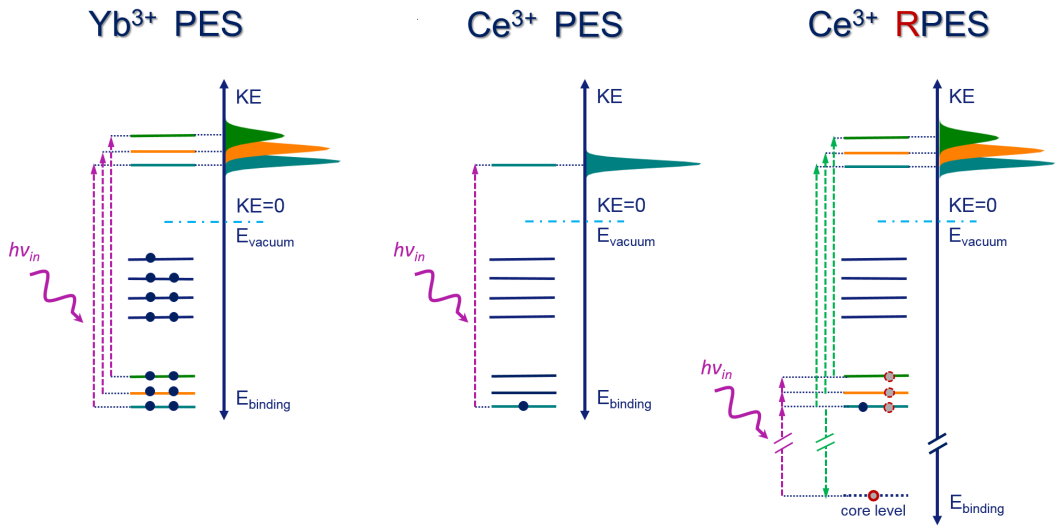

Figure 1.10: Photoemission spectroscopy from the $4f$ subshell of lanthanides. If the $4f$ levels are occupied, as in the case of Yb^{3+}, the CEF splittings are observable with direct PES, each peak corresponding to a level. This is not possible on Ce^{3+}, because only the ground state is populated. In Resonant PES, a core electron is resonantly excited into the $4f$ subshell and the super Coster-Kronig decay from the $4f$ levels is observed. The emitted electrons will have different energies depending on the $4f$ levels occupied in the intermediate state, which allows to determine the splitting between the levels.

A final remark shall be made on the techniques presented up to now, in particular the most commonly used: magnetic susceptibility, INS and XAS. In their usual formulation, they all rely on dipole excitations and are therefore insensitive to symmetries higher than twofold. There are, in tetragonal systems, two possibilities for the orientation of the CEF wavefunctions, distinguished by a 45° rotation about the crystal c axis. The wavefunction orientation is of relevant importance for the study of the hybridization effects with the neighboring atoms. It does not affect the splitting, the symmetry or the mixing α^2, therefore it is not detectable with any of the techniques only sensitive to these quantities. Recently, core-level photoemission [85] and Non Resonant X-ray Scattering [43] demonstrated their sensitivity to the in-plane orientation of the $4f$ orbitals. We will show that the same information can be obtained easily with Resonant Inelastic X-ray Scattering that, as a second order process, is not limited to dipole excitations only.

Photoemission spectrocopy

One of the most used experimental techniques to gain information about the electronic states in matter is photoemission spectroscopy (PES), which analyses the energy (and momentum) of the electrons emitted by a sample exposed to monochromatic UV or X-ray radiation. In

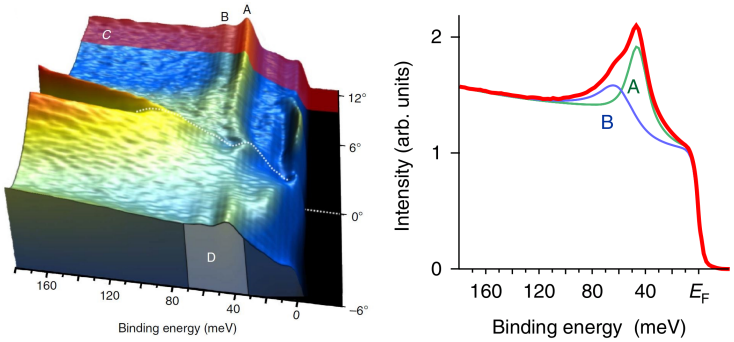

Figure 1.11: Resonant Photoemission data of $CeRh_2Si_2$ from Ref [88]. The two features labelled A and B correspond to the signal due to CEF levels. The splittings estimated for the $^2F_{5/2}$ multiplet are 48 (A) and 62 meV (B), with a Γ_7^1 - $\Gamma_6 - \Gamma_7^2$ scheme. A dispersion of the levels due to hybridisation with the approaching valence band is clearly visible.

standard PES, an electron is excited by a photon in an empty state above the Fermi level and, if it has a sufficient energy and its momentum points towards the sample surface, it can leave the sample. The kinetic energy of the photoelectron is then detected and, by imposing the energy conservation, one can find the energy of the electron before the excitation, that is the energy of its starting electronic level. Angular Resolved PES (ARPES), exploiting also the momentum conservation, can map the dispersion relation $E(\boldsymbol{k})$ of electronic levels (or bands).

PES is successfully used to study the splitting and hybridisation-induced dispersion of $4f$ CEF-levels, as long as they are populated so that electrons can be photoemitted. This is in general the case of heavier lanthanides as europium or ytterbium [81, 73] (Figure 1.10, left panel). Cerium, on the other hand, has at most one electron in the $4f$ shell and photoemission from the unoccupied CEF-levels is not possible. It is in principle possible to thermally populate the higher energy CEF-levels and to observe other CEF-related features [86], but this does not provide the full CEF scheme and comes with several technical difficulties. The study of empty levels is usually carried out via Inverse Photoemission Spectroscopy (IPES) [87], but the resolution (~ 0.1 eV) is not good enough to study the CEF splitting.

Recently, Resonant Photoemission Spectrocopy was used to probe the splitting and dispersion of CEF levels in cerium compounds [88]. By tuning the photon energy to the $M_{4,5}$ or $N_{4,5}$ edges, $3d$ or $4d$ core level electrons are excited into the valence subshell ($4f$), generating a core hole. If at least another electron is present in the valence subshell, a super Coster-Kronig Auger decay is possible. The core hole is filled by a $4f$ electron and the released energy is transferred to another $4f$ electron, which is emitted (Figure 1.10, right). A typical drawback of PES-RPES is the surface sensitivity: it is discussed in Ref. [88] that

not only the surface quality, but also which atom terminates the surface after the cleaving (Ce or Si in the case of $CeRh_2Si_2$) influences the features observable in the spectrum. Moreover, the enhanced surface sensitivity, caused by the short inelastic mean free path of electrons, may be a limitation to draw conclusions about the CEF effects in the bulk. Lastly, it should be stressed that in the photoemission process, one electron is removed from the ion and its energy is measured only *afterwards*. During the photoemission, the other electrons may reorganize to screen the generated hole, thus emitting the photoelectron with a slightly different energy. The measured value is therefore the energy of the electronic level *without* the electron, that can be different from the actual energy of an electron in that level.

1.4 Scope of this thesis

The strongly interacting $4f$ CEF-split levels are the origin of the manifold of exotic phenomena arising in rare earth intermetallic compounds, as discussed in section 1.1. This makes the study of the crystalline field effects in these compounds of primary importance, so that many techniques have been developed during the years to investigate the rare earths' $4f$ levels, the most relevant of which were discussed in section 1.3. Drawbacks and limitations are present in every technique and only a partial information about the CEF can in general be obtained.

In this thesis work, Resonant Inelastic soft X-ray Scattering (RIXS) is presented for the first time as a technique able to probe directly $4f$ CEF levels' splittings and symmetries, with bulk sensitivity and free of a complex background. A RIXS investigation of $4f$ levels became possible only in the last two years, with the inauguration of the ID32 beamline at ESRF and its high resolution RIXS spectrometer, first of a new generation of instruments that are being built in many facilities around the world. In chapter 2 the possible RIXS processes in 4f systems are discussed and data obtained with 250 meV resolution using the predecessor of the current spectrometer is presented. This data already shows all the possible features visible in a rare-earth RIXS spectrum, including first hints on CEF effects.

Chapter 3 describes the instrumentation for high resolution soft-RIXS experiments, focusing on the details and innovations of ID32 and its ERIXS spectrometer. In chapter 4 $CeRh_2Si_2$ is used as an example to demonstrate how information about the splitting, symmetry and orientation of the states can be obtained from the spectra. RIXS is also sensitive to the dispersion of $4f$ levels and this will be shown in chapter 5, where a simple model for the interpretation of the data will be also provided. Finally, chapter 6 deals with the limits of the presented method. $CeCu_2Si_2$ spectra will be used to show an analysis of the CEF in

a system with splittings smaller than the instrumentation's resolution, while $CeCo_2Ge_2$ will represent a case with very large splittings, where the usual hypothesis and approximations made in CEF analysis are not valid. Finally, in the Summary and outlook the most important results will be summarized and the possible future of the use of RIXS on rare earth compounds is outlined.

Chapter 2

Resonant inelastic soft X-ray scattering from $4f$ states

Resonant Inelastic X-ray scattering (RIXS) is a synchrotron-based spectrocopic technique able to directly probe elementary excitations in a large variety of systems [89, 90, 91, 92, 93, 94, 95, 96, 97]. In this chapter the basic concepts for the understanding of RIXS spectrocopy are presented, paying particular attention to its applications for the study of rare earth intermetallic compounds at the $M_{4,5}$ edge.
The scattering process is described, starting from a basic description and then deriving and discussing in detail the formula for the RIXS cross section. The peculiar properties that make RIXS so powerful and suitable for the study of strongly correlated systems are then listed and commented on, together with the possible excitations accessible by this technique. Results of a first, exploratory RIXS study of cerium intermetallics will be presented, showing the typical features observable. The data, acquired on ID08, the former soft-RIXS beamline of ESRF, also serve to depict the state of the art of $M_{4,5}$ RIXS before the instrumentation upgrades of the last years, setting the starting point for this thesis work.

2.1 Fundamentals of resonant inelastic X-ray scattering

RIXS is a *photon in - photon out* process in which a photon is scattered off a sample leaving behind an excitation. The energy of the incident photon is set to an X-ray absorption resonance of the sample, largely increasing the scattering cross section and ensuring chemical sensitivity. Depending on the details of the light-matter interaction, the sample may be left in different excited states which can be characterised by looking at the changes in the photon's energy, momentum and/or polarisation. By comparing the photon's properties

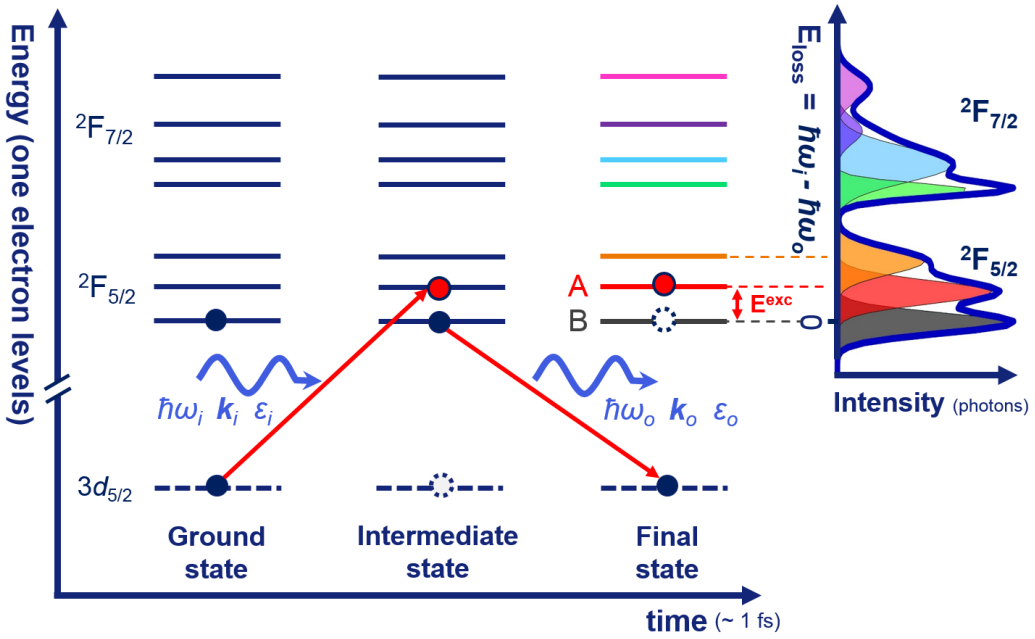

Figure 2.1: Simplified scheme of an M_5 RIXS process on Ce^{3+}, leading to a ff excitation between CEF-split levels which can be detected as an energy loss of the scattered photon. The peaks in the photon energy loss spectrum (right) directly correspond to the different CEF-split $4f$ levels that can be occupied by the $4f$ electron in the final state.

before and after the interaction, information can be retrieved about the sample's ground and excited states.

The whole interaction can be, in a simplified approach, interpreted as a two-step process. First, the photon is resonantly absorbed by a core electron, which is promoted to an empty electronic level (A), leaving a deep core hole. The sample is thus in a highly energetic intermediate state which decays within a few femtoseconds via either an Auger process (as in RPES) or a radiative transition. In the latter case, an electron from a valence level (B) recombines with the core hole, emitting a second X-ray photon. If the electronic levels A and B differ, a net electronic transition from A to B took place in the sample, as depicted in Figure 2.1 in the case of a $4f \rightarrow 4f$ (or ff) transitions in Ce^{3+}. Other kinds of excitations, like magnons or phonons, and charge transfer may occur, depending on many possible phenomena taking place in the highly excited intermediate state. It must be stressed that the given scheme, although it provides an easy interpretation of the peaks of a RIXS spectrum, is missing an important detail. The highly excited intermediate state has a linewidth broadening of $\sim$ 1 eV, large if compared with the splittings among the different possible intermediate states. Many intermediate states can therefore contribute to the scattering process and must be considered at the same time.

In order to avoid the thermal population of the excited states, RIXS experiments are usually performed at low temperatures. In this way, before the interaction, the sample lies in its ground state, which constitutes the reference energy for all the RIXS transitions. Information about the excitations occurring in the sample can be obtained by imposing the energy and momentum conservation of the whole system, made of the photons and the scatterer:

$$\begin{aligned} \hbar\omega_i &= \hbar\omega_o + E^{exc}, \\ \hbar\boldsymbol{k}_i &= \hbar\boldsymbol{k}_o + \hbar\boldsymbol{q}^{exc}, \end{aligned} \tag{2.1}$$

where $\hbar\omega_i$ ($\hbar\omega_o$) is the energy of the incident (outgoing) photon and $\hbar\boldsymbol{k}_i$ ($\hbar\boldsymbol{k}_o$) is the corresponding momentum. Moreover a third conservation law applies to the angular momentum, regarding the polarisation of the ingoing (ϵ_i) and outgoing (ϵ_o) photons, as well as the total angular momentum of the sample. If the energy, momentum and polarisation of both the ingoing and outgoing photons are known, the corresponding properties of the excitation can be retrieved.

In a RIXS experiment the energy $\hbar\omega_i$ and polarisation ϵ_i of the incident photons are controlled to a high degree, thanks to the use of synchrotron beamlines, equipped with undulators and monochromators. So are the absolute values of the momenta, since $\hbar|\boldsymbol{k}_i| = \hbar\omega_i/c$ and $\hbar|\boldsymbol{k}_o| = \hbar\omega_o/c \approx \hbar\omega_i/c$, where it is used the fact that $E^{exc} \ll \hbar\omega_i$ and therefore $\hbar\omega_i \approx \hbar\omega_o$. The directions of the momenta are imposed by the geometry of the experiment, i.e. by the angles defined by the beamline, the sample and the spectrometer, which selects the photons scattered in a certain solid angle. The parameters to be determined in order to have a full description of the process, and of the excitations, are therefore the energy and polarisation of the scattered photons. These can be measured with a spectrometer and a polarimeter respectively.

A last observation can be made before facing the details of the calculation of the RIXS cross section. RIXS was described as consisting of two radiative transitions, absorption and emission, each one of which is regulated by the dipole selection rules. The total RIXS transition, however, does not follow these rules. ff excitations provide a typical example: the transition $4f \to 4f$ would be forbidden by dipole, since $\Delta l = 0$, but the two steps $3d \to 4f$ ($\Delta l = +1$) and $4f \to 3d$ ($\Delta l = -1$) are allowed, making the whole transition possible. RIXS can therefore access transitions forbidden by dipole selection rules.

2.1.1 The Kramers-Heisenberg cross section

The RIXS cross section can be derived by considering the Hamiltonian of the system and calculating the transition probabilities using perturbation theory[92, 98]. Quantum electrodynamics is used to describe the interaction between the electrons and the photons' electromagnetic field, the latter being represented by a vector potential $\boldsymbol{A}(\boldsymbol{r},t)$ (so that $\boldsymbol{E}(\boldsymbol{r}) = -\nabla\phi - \partial\boldsymbol{A}/\partial t$ and $\boldsymbol{B} = \nabla \times \boldsymbol{A}$, where ϕ is a continuously differentiable scalar function). In the non-relativitic case and in the limit that the potentials related to both the electrons and the photons in the system are small compared to twice the mass of the electron ($e\phi/2mc^2, e|\boldsymbol{A}|/2mc \ll 1$), the Hamiltonian for a system with N electrons interacting with an electromagnetic field is written (in SI units) as:

$$\begin{aligned} H =& \sum_j^N \Bigg(\frac{[\boldsymbol{p}_j + e\boldsymbol{A}(\boldsymbol{r}_j)]^2}{2m} + \frac{e\hbar}{2m}\boldsymbol{\sigma}_j \cdot \boldsymbol{B}(\boldsymbol{r}_j) \\ &+ \frac{e\hbar}{2(2mc)^2}\boldsymbol{\sigma}_j \cdot \{\boldsymbol{E}(\boldsymbol{r}_j) \times [\boldsymbol{p}_j + e\boldsymbol{A}(\boldsymbol{r}_j)] - [\boldsymbol{p}_j + e\boldsymbol{A}] \times \boldsymbol{E}(\boldsymbol{r}_j)\} \Bigg) \\ &+ H^{\text{Coulomb}} + \int d\boldsymbol{k} \sum_\epsilon \hbar\omega_{\boldsymbol{k}} \left(c^\dagger_{\epsilon,\boldsymbol{k}} c_{\epsilon,\boldsymbol{k}} + \frac{1}{2} \right) , \end{aligned} \tag{2.2}$$

where $\boldsymbol{p}_j$, $\boldsymbol{r}_j$ and $\boldsymbol{\sigma}_j$ are the momentum and position operators and the Pauli matrices acting on the electron j, respectively. $c^{(\dagger)}_{\epsilon,\boldsymbol{k}}$ annihilates (creates) a photon with wave-vector $\boldsymbol{k}$ and polarisation ϵ. The first term of H is the kinetic energy of the electrons in presence of an electromagnetic field, the second yields the Zeeman splitting and the third takes into account the spin-orbit coupling. H^{Coulomb} contains the remaining electrostatic interactions of electrons with the charges in the sample (among which, the potential of the nucleus, the electron-electron interaction and crystal field). The last term is the energy of the radiation summed on all the modes, each mode having energy $\hbar\omega_{\boldsymbol{k}}$.

To derive the photon scattering cross section, it is convenient to split the Hamiltonian H in an electron-photon interaction part H' and the remaining terms $H^0 = H^{\text{el}} + H^{\text{em}}$, which describe the electrons and and photons in absence of the interaction. H' can then be treated as a perturbation of H^0. Since H^0 does not mix the electron and photon terms, its eigenfunctions are written as product of those of H^{el} and H^{em}.

Let's consider a single photon in the initial state, with momentum $\hbar\boldsymbol{k}_i$, energy $\hbar\omega_i$ and polarisation ϵ_i, that is scattered to $\hbar\boldsymbol{k}_o$, $\hbar\omega_o$, ϵ_o. In the process, the sample changes its state from the ground $|g\rangle$ to a final $|f\rangle$ one. The total wavefunctions of the system can thus be written as $|\text{g}\rangle = |g; 1_{\epsilon_i,\boldsymbol{k}_i}\rangle$ and $|\text{f}\rangle = |f; 1_{\epsilon_o,\boldsymbol{k}_o}\rangle$, where $|1_{\epsilon_o,\boldsymbol{k}_o}\rangle$ is the one-photon wavefunction, result of the application of the creation operator $c_{\epsilon,\boldsymbol{k}}$ on the vacuum state $|0\rangle$. The energy corresponding to the $|\text{g}\rangle$ and $|\text{f}\rangle$ states are, respectively, $E_{\text{g}} = E_g + \hbar\omega_i$ and

$E_{\mathrm{f}} = E_f + \hbar\omega_o$.

The transition rate w for the scattering process can be written, in the second order perturbation theory, as

$$w = \frac{2\pi}{\hbar}\sum_f \left| \langle \mathrm{f}|H'|\mathrm{g}\rangle + \sum_n \frac{|\langle \mathrm{f}|H'|n\rangle|\langle n|H'|\mathrm{g}\rangle}{E_{\mathrm{g}} - E_n} \right|^2 \cdot \delta(E_{\mathrm{f}} - E_{\mathrm{g}}) \ , \tag{2.3}$$

where n runs over the intermediate states $|n\rangle$, eigenstates of the unperturbed Hamiltonian H^0 with energy E_n. In a general (non resonant) scattering event, the first order amplitude dominates the second order, which is usually neglected. In the case of RIXS, instead, the incoming X-ray energy matches an absorption edge, therefore, for some $|n\rangle$, $E_{\mathrm{g}} \approx E_n$, making the second term very large.

Within the limits considered here (non-relativistic electrons in small potentials), the resonant part of the second order amplitude can be written as

$$w = \frac{e^2\hbar}{2m^2 V\epsilon_0\sqrt{\omega_{\boldsymbol{k}_i}\omega_{\boldsymbol{k}_o}}} \sum_n \sum_{j,j'}^{N} \frac{\langle f|\epsilon_o^* \cdot \boldsymbol{p}_{j'} e^{-i\boldsymbol{k}_o\cdot\boldsymbol{r}_{j'}}|n\rangle\langle n|\epsilon_i \cdot \boldsymbol{p}_j e^{-i\boldsymbol{k}_i\cdot\boldsymbol{r}_j}|g\rangle}{E_g + \hbar\omega_{\boldsymbol{k}_i} - E_n + i\Gamma_n} \ . \tag{2.4}$$

V is the volume of the system and a broadening Γ_n is introduced in the denominator to account for the short lifetime ($\sim$ 1 fs) of the intermediate states. Considering (2.4) as the second order term in (2.3), and neglecting the first order term, one obtains the Kramers-Heisenberg expression for the RIXS cross section.

The formula can be further simplified by means of the dipole approximation, that holds true for soft X-ray photons interacting with atomic electrons. $e^{i\boldsymbol{k}\cdot\boldsymbol{r}}$ can indeed be considered to be approximately constant at the length scale of the atomic wavefunctions, therefore $e^{i\boldsymbol{k}\cdot\boldsymbol{r}} = 1 + i\boldsymbol{k}\cdot\boldsymbol{r} + ... \approx 1$. The scattering amplitude becomes

$$\begin{aligned} w &= \frac{e^2\hbar}{2m^2 V\epsilon_0\sqrt{\omega_{\boldsymbol{k}_i}\omega_{\boldsymbol{k}_o}}} \sum_n \sum_{j,j'}^{N} \frac{\langle f|\epsilon_o^* \cdot \boldsymbol{p}_{j'}|n\rangle\langle n|\epsilon_i \cdot \boldsymbol{p}_j|g\rangle}{E_g + \hbar\omega_{\boldsymbol{k}_i} - E_n + i\Gamma_n} \approx \\ &\approx \frac{e^2\hbar}{2m^2 V\epsilon_0}\sqrt{\omega_{\boldsymbol{k}_i}\omega_{\boldsymbol{k}_o}} \sum_n \sum_{j,j'}^{N} \frac{\langle f|\epsilon_o^* \cdot \boldsymbol{r}_{j'}|n\rangle\langle n|\epsilon_i \cdot \boldsymbol{r}_j|g\rangle}{E_g + \hbar\omega_{\boldsymbol{k}_i} - E_n + i\Gamma_n} \ , \end{aligned} \tag{2.5}$$

where the operator $\boldsymbol{p}$ was substituted with the commutator $im[H^0, \boldsymbol{r}]/\hbar$ and the equality $\langle n|\epsilon_i \cdot [H^0\boldsymbol{r}]|g\rangle = \langle n|H^0\epsilon_i \cdot \boldsymbol{r}|g\rangle - \langle n|\epsilon_i \cdot H^0\boldsymbol{r}|g\rangle = (E_n - E_g)\langle n|\epsilon_i \cdot \boldsymbol{r}|g\rangle \approx \hbar\omega_{\boldsymbol{k}_i}\langle n|\epsilon_i \cdot \boldsymbol{r}|g\rangle$ was used. Finally, one can obtain the double differential cross section by multiplying w by the density of (outgoing) photons' states in the solid angle $d\Omega$ (that is $V\boldsymbol{k}_o^2 d|\boldsymbol{k}_o|d\Omega/(2\pi)^3 = V\omega_{\boldsymbol{k}_o}^2 d\hbar\omega_{\boldsymbol{k}_o} d\Omega/\hbar c^3(2\pi)^3$) and dividing by the photon flux c/V. The RIXS cross section

results:

$$\frac{d^2\sigma}{d\hbar\omega d\Omega} = r_e^2 m^2 \omega_{\boldsymbol{k}_i} \omega_{\boldsymbol{k}_o}^3 \sum_f \left| \sum_n \sum_{j,j'}^{N} \frac{\langle f|\epsilon_o^* \cdot \boldsymbol{r}_{j'}|n\rangle\langle n|\epsilon_i \cdot \boldsymbol{r}_j|g\rangle}{E_g + \hbar\omega_{\boldsymbol{k}_i} - E_n + i\Gamma_n} \right|^2 \delta(E_g - E_f + \hbar\omega) \ , \qquad (2.6)$$

where $r_e = e^2/(4\pi\epsilon_0 mc^2)$ is the classical electron radius and $\hbar\omega = \hbar\omega_{\boldsymbol{k}_i} - \hbar\omega_{\boldsymbol{k}_o}$.

The δ function assures the energy conservation, so that the difference of the photon energies equals the excitation energy of the system. The RIXS excitations will be therefore observed at constant energy losses. This distinguishes proper RIXS features from fluorescence that occurs at fixed $\hbar\omega_{\boldsymbol{k}_o}$. Therefore the energy loss $\hbar\omega = \hbar\omega_{\boldsymbol{k}_i} - \hbar\omega_{\boldsymbol{k}_o}$ increases linearly with the energy of the incident photons. These features are in general given by the radiative decay of an electron from shells different to those reached by the excited electron in the intermediate state. The information about $\hbar\omega_{\boldsymbol{k}_i}$ is lost and $\hbar\omega_{\boldsymbol{k}_o}$ only depends on the ΔE between the atomic levels involved in the emission of the photon.

It shall be noted that the cross section formula contains two dipole operators and both transitions must be allowed in order to go from the state $|g\rangle$ to $|f\rangle$. The cross section formula correctly reproduces also the interference among the possible excitations paths discussed in the previous section, because the sum over the intermediate states n is carried out before the absolute square. The sum over all the possible intermediate states might lead to very demanding computations in complex systems, when one wants to simulate a RIXS spectrum. Software programs such as Quanty or SolidStatePhysics overcome this problem by introducing Green's functions for the description of the scattering process, that make the calculations much faster.

Lastly, it must be stressed that the resonance acts as an amplifier increasing remarkably the cross section of the process and enhancing the sensitivity of the measurements, which would be otherwise impossible, due to the very small numerators in the formula. Despite this, RIXS is still a very *photon hungry* technique, and sources with very high brilliance, as well as sensitive instrumentation and detectors are necessary to perform experiments.

2.1.2 Strengths of the technique

Many characteristics of the scattering process described above make RIXS a powerful and unique technique for studying elementary excitations in condensed matter. The most important aspects are shortly reviewed here, paying particular attention to the features that allow to provide complementary information to, and overcome the drawbacks of, the established techniques used to investigate $4f$ states in rare earths. First of all it is clear from the aforementioned conservation laws that RIXS can simultaneously probe the energy and

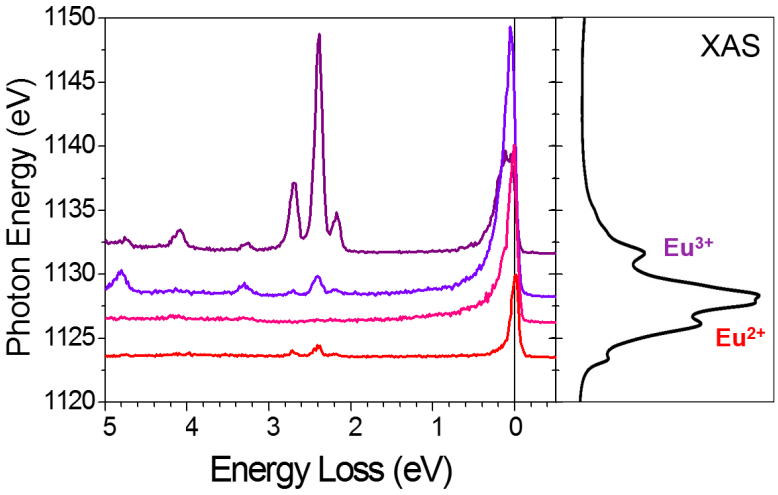

Figure 2.2: RIXS spectra of the mixed valence compound $EuNi_2P_2$ at different incident energies accross the M_5 edge (left) and corresponding XAS spectrum (right). While in the XAS spectrum features coming from Eu^{2+} and Eu^{3+} are superimposed, the RIXS spectra clearly changes depending on the resonance selected.

momentum of the excitations, therefore it can map the dispersion relations. Soft x-ray photons with $\hbar\omega_{\boldsymbol{k}} \approx 1$ keV can transfer a maximum momentum of $2\hbar\boldsymbol{k} \approx 1$ Å^{-1}, comparable with the typical sizes of the Brillouin zone in cerium intermetallics of the 122 family (~ 0.5 or 1.5 Å^{-1}, depending on the direction considered, given that $c \sim 10$ Å and $a \sim 4$ Å in the unit cell). Neutrons might in general probe a wider region of the reciprocal space, but this is usually not exploited for ff excitations. The strong $\boldsymbol{q}$ dependence of the cross sections for phonon and magnetic scattering, indeed, causes the magnetic (ff) contribution to be lost in the phonon background at high scattering angles. Furthermore, INS experiments are often performed on powdered samples, therefore averaging $\boldsymbol{q}$ on all the possible orientations of the crystal.

The use of powders is dictated in INS by the need of large samples ($\approx$ grams, i.e. cm^3 sizes), difficult to grow as single crystals, in order to compensate for the small scattering cross sections. This is obviated in RIXS by the use of resonance, that amplifies the signal and allows to measure sub-millimeter size single crystals or thin films.

The resonant nature of RIXS also provides element sensitivity. This becomes very important when one wants to focus on excitations related to a specific subshell of a sample's constituent, as is the case of ff excitations. This holds true also for phonons and magnons, that are visible in a RIXS spectrum only if they are somehow coupled with the electronic

levels involved in the RIXS process. The large and complex phonon background present in INS is therefore greatly, if not completely, suppressed.

Chemical sensitivity is also guaranteed in RIXS spectroscopy. Different oxidation states (or valences) of the same element have slightly shifted absorption edges and one can tune the incident photon energy to the desired one. This becomes helpful in the study of mixed valence compounds, where only a specific valence can be selected, neglecting the mixing (Figure 2.2). In contrast, the valence mixing is directly visible in a XAS spectrum, and it must be considered to correctly analyse the data.

The RIXS process is also charge neutral, meaning that no electron is added to or removed from the sample during the process. In the case of ff excitations, one also does not change the occupancy of the 4f shell. This guarantees that the energy splittings measured in a RIXS spectrum are free of any screening effect, in contrast to e.g. photoemission. Another important feature that distinguishes RIXS from PES is the bulk sensitivity: soft X-rays can travel tens of nanometers inside the sample, making the surface contribution negligible compared to the rest of the volume probed. If desired, the surface contribution can be enhanced by selecting a scattering geometry in grazing incidence. The quality of the surface is however important for the study of features very close (or superimposed) to the peak at zero energy loss, because the roughness of the surface contributes to the diffuse (elastic) scattering. Lastly, the possibility of investigating the polarisation dependence of each feature provides further information on the nature of each excitation.

2.1.3 Excitations accessible to RIXS

The RIXS process may leave several types of excitations in the sample, depending on the selected absorption edge and the properties of the material. The most important features are outlined here, while a more complete review can be found in Refs. [92, 94].

Orbital excitations. If the valence subshell involved in the RIXS process is partially filled (i.e. other electrons than the photoexcited one can decay to fill the core hole) an orbital excitation can occur; this is the case of ff excitations depicted in Figure 2.1. $3d$ orbital (dd) excitations have been widely studied, because of the very large CEF splittings (> 1 eV) that made them detectable with the much lower resolution of the first RIXS spectrometers. These excitations usually provide local information about the ionic orbitals. In some special cases, degenerate orbitals can be present and these may couple with the neighboring sites by superexchange, allowing collective orbital excitations, called orbitons. It must be stressed

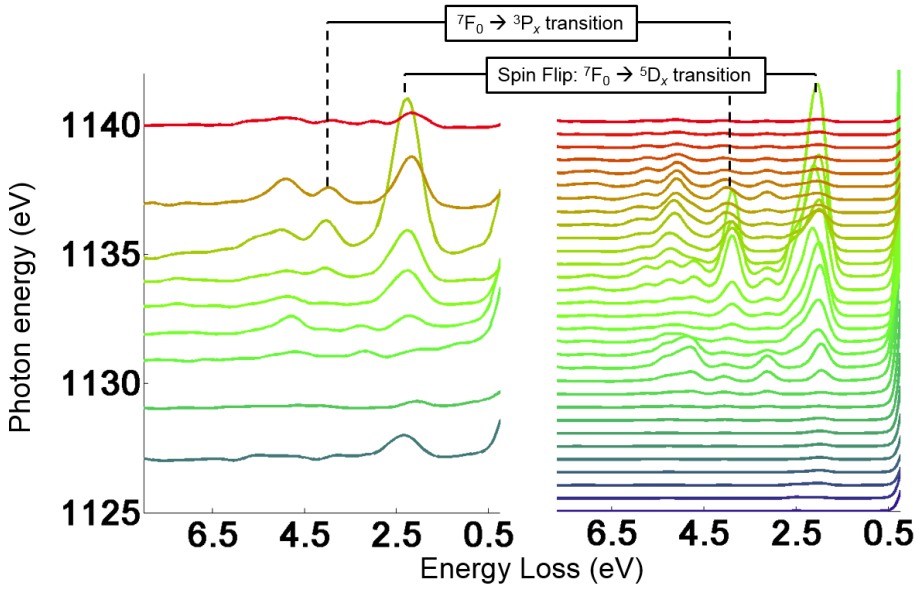

Figure 2.3: M_5 RIXS spectra of $EuCo_2Si_2$ at different incident energies accross the edge (left) and simulations for a Eu^{3+} (right) ion, showing the manifold of multiplet excitations. Crystal field was not considered in this simulation.

that in a RIXS spectrum the peaks due to orbital excitations do not necessarily correspond to the one-electron levels as depicted in Figure 2.1. This happens only when one single electron (or hole) occupies the valence subshell as in Ce^{3+} ($4f^1$) and Cu^{2+} ($3d^9$). In other ions, as Eu^{3+} (Figure 2.3), the electronic interactions within the electrons in the valence subshell give rise to a complex multiplet structure, resulting in a manifold of peaks.
RIXS is also sensitive to many other elementary excitations, due to various phenomena that might take place in the intermediate excited state.

Collective magnetic excitations. In materials with magnetic correlations, collective magnetic excitations are possible. In general, photons carry an angular momentum $L^{ph} = 1$ that can be exchanged during the interaction, meaning that a RIXS process can transfer $\Delta L_z^{ph} = 0, 1, 2$ to the sample. In the example of $3d$ materials, where the magnetism is related to the spin of valence electrons, the transferred angular momentum may rotate one or two spins ($\Delta S_z = 1$ or $\Delta S_z = 2$), giving rise to magnons or bi-magnons. The rotation of the spin occurs in the intermediate state, in which the spin of the $2p$ core hole, due to the strong spin-orbit coupling, is not a good quantum number and it is allowed to change. Since magnetic excitations imply a change of the angular momentum (i.e. the polarisation) of the photon, they are usually well recognisable via a polarisation analysis.

Phonons. Due to the extra valence electron, the intermediate state presents a local valence charge disequilibrium that might affect the bondings with the neighbouring atoms, eventually generating lattice vibrations, i.e. phonons. These have been observed at the L and K edges [99, 100]. The electron-phonon coupling is anyway small for $4f$ orbitals and a phonon contribution in M edge RIXS spectra has neither been predicted nor observed by experiments.

Charge transfer. The presence of the core hole in the intermediate states can also cause rearrangement of the ligands' charge in order to screen it, yielding a charge transfer from the ligand sites. The process is usually interpreted as a transfer of a ligand (or valence band) electron to the excited ion due to a stronger hybridisation taking place in the intermediate state. Charge transfer excitations (E_{Loss} = 1 to 10 eV) can provide much information about the hopping processes and the on-site repulsion.

Fluorescence. Coster-Kronig conversion and other fluorescence features may also be visible in RIXS spectra, but they lie at much higher energies ($\sim$ 20 eV) and are not usually studied with RIXS. They will be anyway shown in the next section in the specific case of cerium compounds.

Elastic scattering. Lastly, the peak at zero energy loss, even if it does not represent any excitation, must be mentioned in the list of RIXS spectral features. It is due to the photons that don't undergo any inelastic process during the scattering, therefore it is referred to as elastic peak. Most of the elastic intensity comes from diffuse scattering from the sample's surface and is particularly intense in specular geometry. It can be reduced by going off-specular and/or choosing opportune experimental conditions so that $\epsilon_i \cdot \epsilon_o = 0$. Elastic scattering can bring information about orderings present in the sample. Charge density waves and stripes have been found on layered cuprates [101] thanks to the study of the elastic peak in RIXS spectra. These features might be difficult to observe in conventional diffraction experiments without energy discrimination because they produce a small modulation of the elastic intensity, that is lost in the background of the inelastic features. RIXS spectroscopy can separate the inelastic and the elastic contributions, i.e. it can be used as a very sensitive energy resolved diffraction.

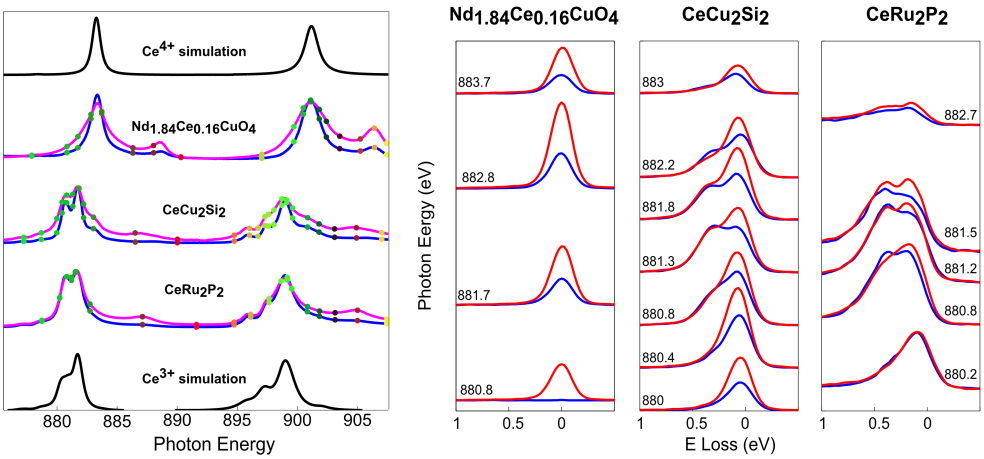

Figure 2.4: (Left) $M_{4,5}$ XAS spectra, with π polarisation and 40° incidence, of three different cerium compounds, together with calculated spectra for pure Ce^{4+} and Ce^{3+} in absence of crystal field. Both total electron yield (blue) and fluorescence yield (magenta) are shown, the latter enhancing features with low intensity. The coloured dots represent the energy at which RIXS spectra were acquired. (Right) Corresponding M_5 RIXS spectra, with σ (red) and π (blue) polarisation, $2\theta = 130°$, $\theta = 40°$ (normal emission).

2.2 $M_{4,5}$ resonant inelastic X-ray scattering on cerium: a first, exploratory study

Before the advent of ERIXS, the high resolution spectrometer installed on ID32 at ESRF, the energy resolution of soft-RIXS instrumentation ($\sim$ 125 meV for SAXES, at Swiss Light Source), was too low for resolving the ff excitations ($\sim 30 - 60$ meV) in cerium. In the following, data acquired in 2013 with the spectrometer AXES on ID08 beamline at ESRF ($\sim$ 250 meV resolution) are presented, in order to review, with the help of an example, all the possible features that were already visible in RIXS spectra of cerium compounds before the latest upgrades. These data have been published in Ref. [102] as part of this thesis work.

2.2.1 First evidence of $4f$ excitations

XAS spectra of $Nd_{1.84}Ce_{0.16}CuO_4$ (NCCO), $CeCu_2Si_2$ and $CeRu_2P_2$ are shown in figure Figure 2.4. By comparing the experimental spectra with the calculated ones for isolated cerium ions, NCCO and $CeRu_2P_2$ can be considered respectively as (almost) pure Ce^{4+} and Ce^{3+}, while $CeCu_2Si_2$ shows spectral signatures of both configurations. M_5 RIXS spectra of NCCO (Figure 2.4, right) confirm its $4f^0$ nature. Since no electron is present in the $4f$ subshell before the $3d \rightarrow 4f$ excitation, the only possible $4f \rightarrow 3d$ emission process is the

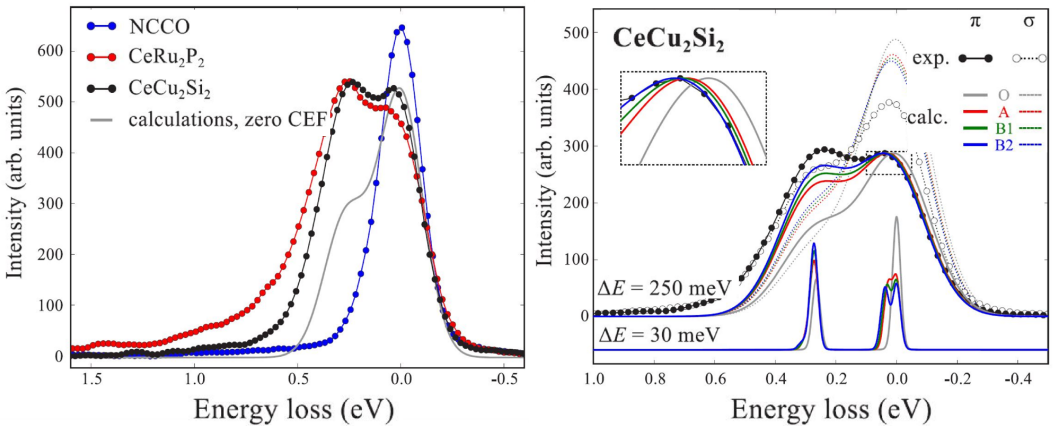

Figure 2.5: (Left) RIXS spectra $CeCu_2Si_2$ and $CeRu_2P_2$ (Ce^{3+}) with incoming photon energy between the two M_5 XAS peaks with π polarisation. The spectra are not fit by calculations without CEF, proving that RIXS is sensitive to its effects. The difference between the two spectra in the low energy range (< 0.5 eV) are due to different CEF schemes. NCCO (Ce^{4+}) does not show any low energy inelastic features. (Right) RIXS spectra for $CeCu_2Si_2$ and corresponding spectra calculated using different sets of CEF parameters. The calculations without CEF (0) don't fit the data, while introducing the CEF the fit improves. A uses CEF parameters obtained from INS [103], with a Kramer's doublet ground state and a quartet at 29 meV (0-29-29 meV splitting scheme), while $B1$ and $B2$ are obtained by sligtly modifying the CEF (respectively giving splitting of 0-29-34 meV and 0-33-41 meV). The three schemes provide a similar fit of the magnetic susceptibility curves (see Ref. [102] for details). Even with 250 meV resolution, small variations of the CEF have visible effects on the spectra.

decay of the excited electron back into the core hole. The emitted photon has the same energy of the absorbed one, giving only an elastic peak at zero energy loss. On the other hand, $CeCu_2Si_2$ and $CeRu_2P_2$ spectra have a two-peak structure, due to the presence of a $4f$ electron that makes ff excitations possible. The first peak, around zero energy loss, contains all transitions within the ${}^2F_{5/2}$ multiplet, included the elastic peak, while the other one, at about 300 meV, consists in all transitions to a ${}^2F_{7/2}$ final state. As expected, the inelastic intensity is higher on resonance. Figure 2.5 compares the spectra of the three compounds. $CeCu_2Si_2$ and $CeRu_2P_2$ spectra cannot be fit by calculations without the CEF effects, implying that RIXS is sensitive to them. Moreover, the two spectra present clear differences, ascribable to different CEF schemes. The right panel of Figure 2.5 show attempts of fitting the $CeCu_2Si_2$ spectrum with calculated spectra, using CEF parameters from Ref. [74] (A) or alternative parameters obtained by the fit of magnetic susceptibility data (B1, B2). It is clear that, due mostly to changes in the peaks' intensities in the three cases, the three slightly different CEF schemes provide distinct spectra. In comparison, the blue curve (B2) best fits the energy position and the intensity ratio of the experimental data. The corresponding CEF parameters yield an energy of 33 and 41 meV for the lowest two

excited CEF levels, in contrast to the 29 meV proposed in Ref [74], and represented by the red curve A1.

Even though a complete determination of the CEF scheme was impossible at the time, due to the lack of resolution, this was the first proof of the ability of RIXS to probe excitations within the $4f$ subshell.

2.2.2 Charge transfer excitations

Charge transfer (CT) processes are a direct consequence of the hybridisation of $4f$ states with the ligand orbitals and involve the hopping of a ligand electron into the $4f$ subshell. Usually CT excitations are in the energy range from 1 to 10 eV and they could therefore be studied even with the low resolution of the early days of RIXS.

The basic process was theorized for the (mostly $4f^0$) mixed valence compound CeO_2 by Nakazawa *et al.* in Refs. [104, 105] and later confirmed by experiments of Watanabe *et al.* [106]. The CT RIXS process is depicted in Figure 2.6. The initial state consists in an admixture of $4f^0$ and $4f^1\underline{v}$ configurations, where $\underline{v}$ represents a valence hole. The admixture generates a bonding ground state, a nonbonding state located 4.5 eV higher in energy and an antibonding state at 7 eV (4 eV and 6 eV respectively according to measurements in Ref. [106]). Similarly, bonding, nonbonding and antibonding states are present in the intermediate state after the $3d \rightarrow 4f$ excitation, given by the admixture of $3d^9 4f^1$ and $3d^9 4f^2\underline{v}$. The presence of the core hole brings the two configurations closer in energy in the intermediate state, resulting in a stronger hybridisation and thus allowing the charge transfer during the RIXS process. When the photon energy is tuned to the main peaks of the $M_{4,5}$ XAS, the bonding intermediate state is selected and a transition to the nonbonding final state is possible, in addition to bonding final state (which includes the elastic peak and ff excitations, if possible). A transition to the antibonding state is also possible, but

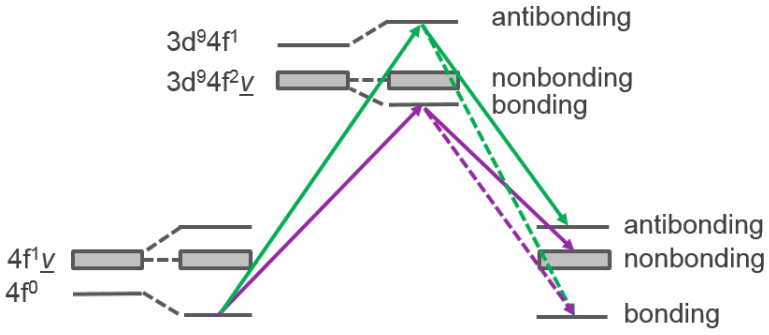

Figure 2.6: Charge transfer process as described in Refs [104, 105]

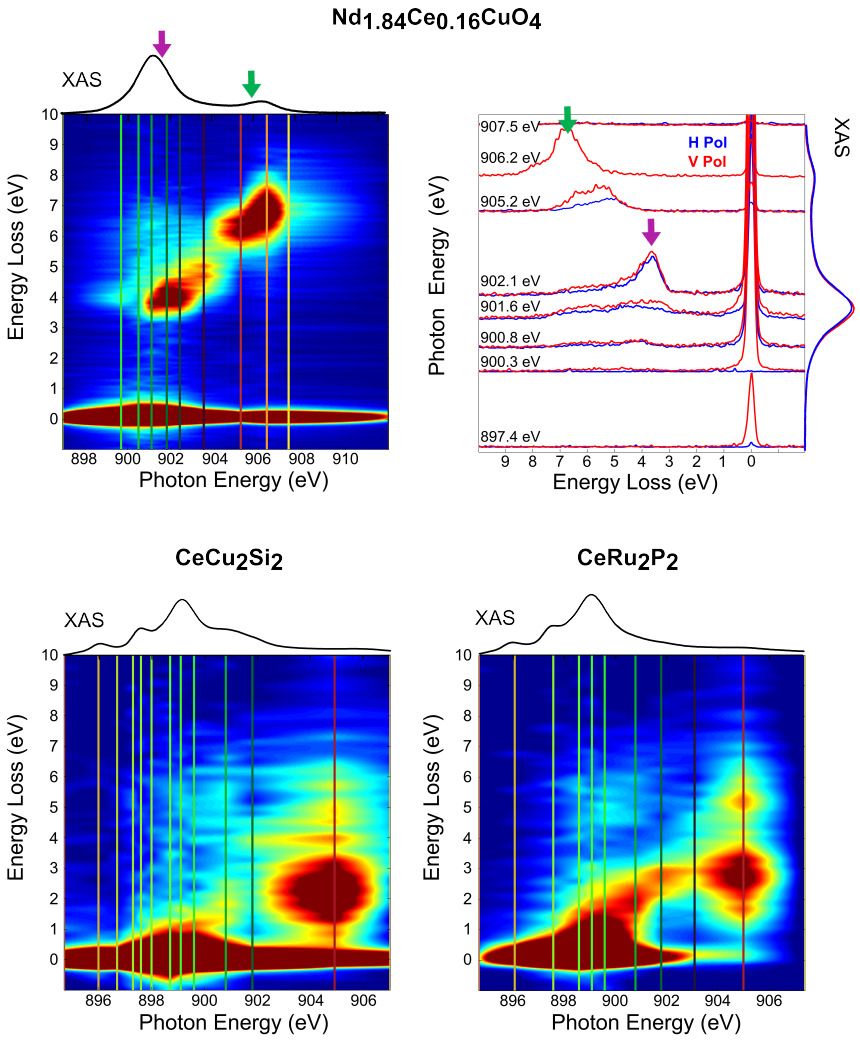

Figure 2.7: M_4 RIXS maps with vertical polarisation of the incident light and corresponding XAS spectra. Vertical lines indicate the spectra used to build the map. For NCCO, the comparison between the two polarisations is also shown.

much weaker. XAS spectra in Figure 2.4 also show a small satellite about $5-7$ eV after the main peaks, not present in the single-ion simulations. These features are an effect of the hybridisation between $4f$ and ligand states. In particular, if the photon energy is set resonant with these satellites, the antibonding intermediate state is selected and the most probable transition is towards the antibonding final state. This provides another example of the importance of the possibility to tune the incident energy in a RIXS experiment, in order to select specific intermediate and final states.

The presented model explains the NCCO M_4 RIXS map in Figure 2.7, where the photon energies giving the two CT processes are indicated by arrows. Consistently with the description above, in correspondence to the XAS main peak a strong intensity is found at

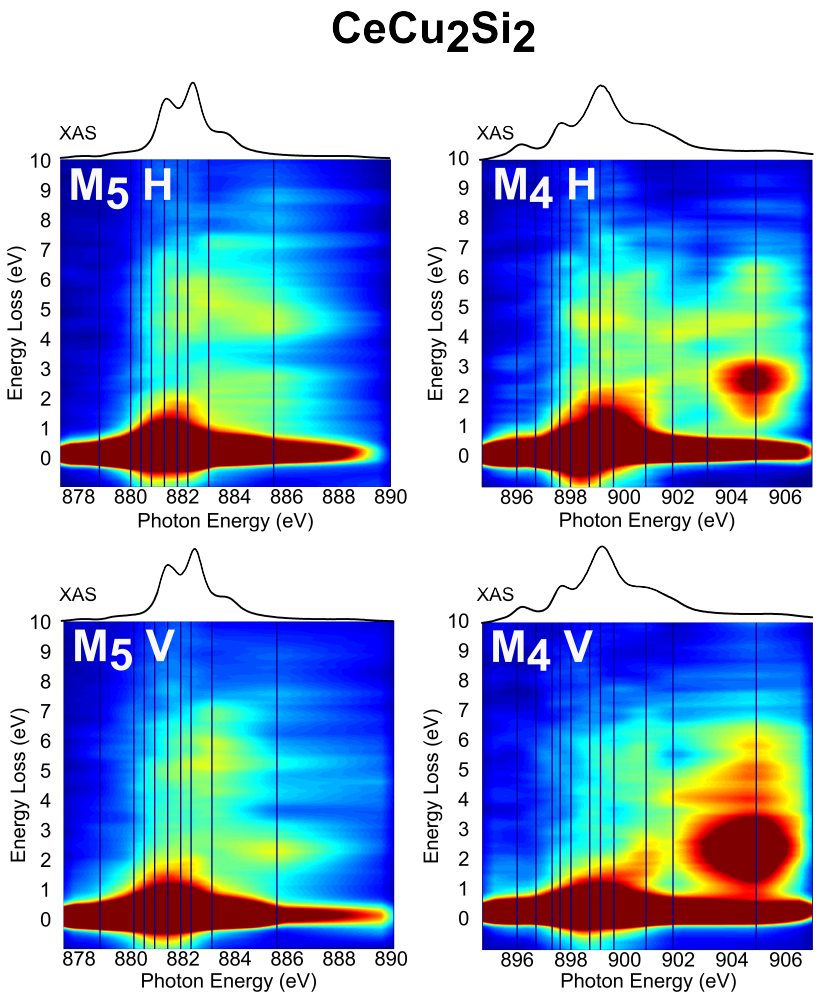

Figure 2.8: $M_{4,5}$ RIXS maps for $CeCu_2Si_2$ with horizontal (H) and vertical (V) polarisation. Zoom on CT region.

4 eV loss, together with a weaker signal around 6 eV, while only the 6 eV feature is visible when the incident photon energy is tuned to the XAS satellite. Both excitations seem to move towards higher energy losses with increasing photon energy. This happens because, by changing the photon energy, it is possible to span the finite bandwidths of the intermediate and final states, always finding a path that allows the CT transition. The transition to the nonbonding final state at 4 eV is independent on the incident photons' polarisation, while the transition to the antibonding state at 6 eV seems enhanced with vertical polarised photons (Figure 2.7, top right). This further confirms the calculations [105], which predicts a weaker signal on the antibonding peak with horizontal polarised light. In order to interpret the RIXS map of $CeCu_2Si_2$ and $CeRu_2P_2$ an extension to the scheme of Figure 2.6 is needed. A suitable model was developed by Nakazawa *et al.* [107] for the description

of charge transfers in $CeRh_3$. Both the metallic nature of the compounds and the higher $4f$ population ($n_f = 0.8$ in their calculations) are taken into account, providing a better description also for cerium compounds of the 122 family. The basis set includes $4f^0$, $4f^1\underline{v}$, $4f^2\underline{v}^2$, $4f^0c\underline{v}$, $4f^1c\underline{v}^2$ and $4f^2c\underline{v}^3$ configurations and more excitations become therefore possible. By using this model, it is still possible to assign in Figure 2.7 a peak to the transition to the nonbonding state (at 1 eV for $CeCu_2Si_2$ and 1.5 eV for $CeRu_2P_2$), which overlaps with the low energy features, and the intense peak on the XAS satellite to the antibonding state (2.2 and 2.8 eV respectively). Other weak features are attributed to e-h pairs and f^2 excitations. It must be noticed that the energy required for a CT excitation diminishes from NCCO to $CeRu_2P_2$ and again to $CeCu_2Si_2$. Following the argument of Dallera *et al.* [108], this effect can be related to the electronegativity of the atoms surounding the rare earth ion. This could also explain the results of Watanabe *et al.*, that found lower energies for CT excitations for $CeRh_3$ compared to CeO_2 and to calculations in Ref. [107]. The presence of the CT excitations at low energies, partly overlapping with the ff signal, implies that the valence band and the $4f$ levels are energetically very close, giving rise to the possibility of hybridisation.

To complete the description of the CT excitations in cerium intermetallic compounds, Figure 2.8 shows the M_4 and M_5 RIXS maps of $CeCu_2Si_2$ with both vertical and horizontal polarised light. The excitations and their energy positions are the same at the two edges, but the intensity ratio between the CT and the ff signal is higher at the M_4 edge. The polarisation dependence of CT transitions observed for NCCO is confirmed in $CeCu_2Si_2$ spectra, where the intensity at 2 eV is always stronger with vertical polarisation of the incident light.

2.2.3 Coster-Kronig conversion and fluorescence

Other features at higher energy losses are visible in RIXS spectra of cerium compounds. Strictly speaking, these features are not related to a RIXS process, because different electronic levels are involved in the absorption and emission steps. The information on the intermediate state, and on the energy of the absorbed photon, can be in general lost in this kind of processes. If this is the case, the energy of the emitted photon is constant and only dependent on the energy of the levels involved in the emission process. These excitations are visible as lines with slope 1 in the RIXS map E_{in} vs. $E_{Loss} = E_{in} - E_{out} = E_{in} - constant$ and are generally referred to as *fluorescence*. In both the M_4 and M_5 RIXS maps of $CeCu_2Si_2$ (Figure 2.9) a peak is present around 22 eV energy loss. In agreement with the experimental observations of Dallera *et al* [108] it can be assigned to a $5p \rightarrow 3d$ radiative deexcitation.

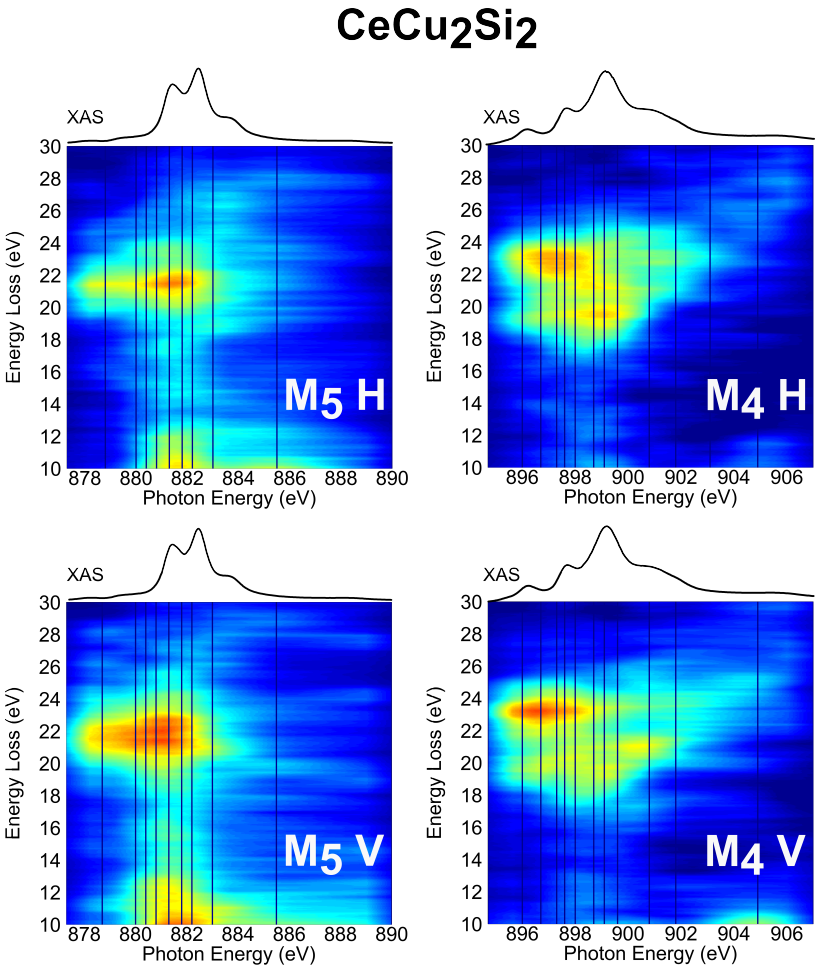

Figure 2.9: $M_{4,5}$ RIXS maps for $CeCu_2Si_2$ with horizontal (H) and vertical (V) polarisation. Zoom on high energy losses.

As measured by Lenth *et al.* [109], the $5p$ subshell lies 22 eV lower in energy than the $4f$, therefore a $5p \rightarrow 3d$ deexcitation generates a photon 22 eV less energetic than the one absorbed in the $3d \rightarrow 4f$ transition (Figure 2.10, left). The energy loss is 2 eV higher in the M_4 RIXS maps, if compared to the M_5 RIXS map with horizontal polarised photons. The data at the M_5 edge with vertical polarised light, on the other hand, show a broad peak from 21 to 23 eV energy loss. Multiple losses are indeed possible, due to the combination of $5p \rightarrow 3d$ emission and CT excitations, that can leave the system in the final state in the $\underline{5p}4f^{n+2}\underline{v}$ configuration, different from the pure $5p$ emission final configuration $\underline{5p}4f^{n+1}$ [110, 108]. The various possible CT processes are not well resolved in the presented maps because of the poor statistics and the strong smoothing applied in order to make these weak features appear out of the noise. In comparison, the $5p \rightarrow 3d$ emission peaks are strong around the main XAS peaks, but disappear quickly with higher photon energies, probably

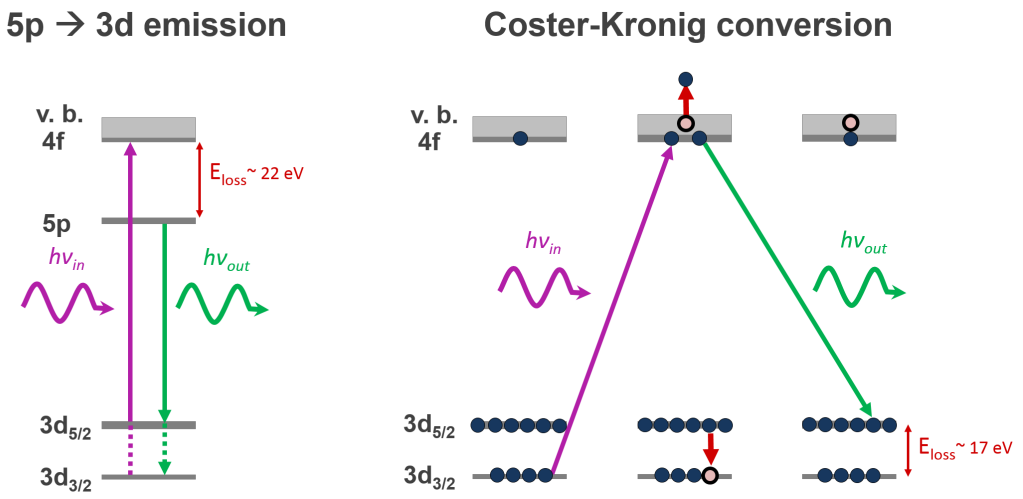

Figure 2.10: Scheme of the $5p \rightarrow 3d$ emission and the MMN Coster-Kronig transition that may occur during a RIXS process.

because other deexcitation processes become more probable. This does not allow to probe the fluorescent behaviour of the process. In the small range of E_{in} for which it is visible, the peak seems indeed to appear at constant energy loss, instead of constant E_{out}.

Another feature is visible at similar energy losses, but only in the M_4 RIXS maps, implying that the corresponding deexcitation path is possible only in presence of a $3d_{3/2}$ hole. This is the case of the MMN Coster-Kronig process (Figure 2.10, right). In the intermediate state, an electron deexcites from the $3d_{5/2}$ to the $3d_{3/2}$ subshell in order to fill the hole, and its energy is transferred to a valence electron, which is photoemitted. A radiative deexcitation then occurs from the valence to the $3d_{5/2}$ hole left by the Coster-Kronig conversion. The emitted photon will differ from the absorbed one in the $3d_{3/2} \rightarrow 4f$ transition by the distance in energy between the $3d_{3/2}$ and $3d_{5/2}$ subshells. This can be measured as the distance between the M_4 and M_5 edges in a XAS spectrum, about 17 eV. Interestingly, the energy loss of this feature increases with increasing incident photon energy, i.e. is a *fluorescence* process. This means that during the Coster-Kronig process the information on the absorption and on the intermediate state is lost and the deexcitation takes place from a relaxed state. The presence of the extra Coster-Kronig deexcitation path causes $3d_{3/2}$ holes to have a shorter lifetime and this results in a larger lifetime broadening of M_4 XAS spectra compared to the M_5.

Chapter 3

Advances in soft X-ray RIXS instrumentation at the ESRF

During the last 20 years, the increasing interests in RIXS, driven by its versatility and ability to probe elementary excitations, has boosted a continuous technical improvement of the instrumentation. In this chapter, the ID32 beamline of European Synchrotron Radiation Facility (ESRF) and its spectrometer, which represent the state-of-the-art in instrumentation for soft-RIXS spectroscopy, are reviewed.

The basic requirements to perform RIXS spectroscopy are a monochromatic incident X-ray beam, an analyser of the scattered photons' energy and a detector. The X-ray photons are provided by synchrotron radiation and are monochromatized along the beamline, while a dispersive spectrometer is usually employed for the energy analysis. On ID32, innovations and extensions to this basic scheme have been introduced. The continuous rotation of the spectrometer and a 6-degrees-of-freedom control of the sample position give a unique and unprecedented flexibility for the choice of the scattering geometry. Moreover, a polarimeter allows for the first time the analysis of the polarisation of the scattered beam. Lastly, the use of a centroid reconstruction algorithm allowed to overcome some limitations of the commercially available CCD detectors.

The whole ID32 beamlime was built in the framework of a major ESRF upgrade program (ESRF Upgrade Phase I) started in 2009 and ended in 2015. The design and commissioning of the ERIXS (European-RIXS) spectrometer and its polarimeter are the result of a long-standing and close collaboration between the group of Professors Giacomo Ghiringhelli and Lucio Braicovich of Politecnico di Milano (Dipartimento di Fisica) and the ESRF (in particular, the ID32 team led by Nicholas Brookes). I had the privilege of following the development of the beamline and spectrometer and dedicated a considerable portion of the

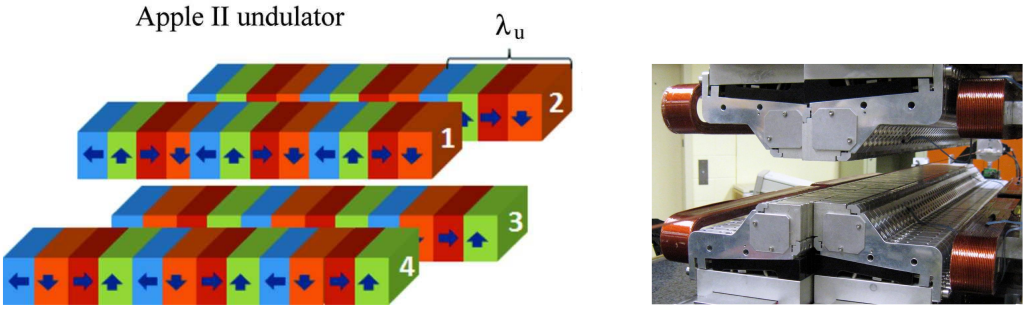

Figure 3.1: Sketch [111] and photo [112] of an APPLE II undulator.

last years to the study of the single photon centroid reconstruction code and to the commissioning of the instrumentation.

The instrumentation and innovations of ID32 are briefly discussed in the following. A more detailed description will be given in forthcoming publications by the ID32 and Politecnico di Milano groups.

3.1 The ID32 beamline at the ESRF

The high flux of monochromatic X-ray photons is produced in the ESRF storage ring. Bunches of electrons are first accelerated up to 6 GeV in the linear accelerator and booster ring of the ESRF and then kept in the 844 m circular trajectory, made up of 32 straight sections, by 64 bending magnets. Quadrupoles and sextupoles guarantee the collimation of the electron beam and klystrons-powered RF cavities maintain the energy of the electrons constant. Various operation modes are possible depending on the needs of the 40 beamlines served. The most suitable modes for RIXS spectroscopy, due to its small cross section, are those providing the maximum electron current (200 mA) in the ring (i.e. the uniform multibunch, 7/8+1 and hybrid modes). In these operation modes, electrons are reinjected every 12 hours in the storage ring to compensate for the losses due to the finite lifetime (69 hours) of the electron beam. The ring is going to be upgraded in the program ESRF Upgrade Phase II, starting in 2019, to offer higher brilliance and coherence and to keep constant the current in the ring, by implementing the top-up mode.

In the 32nd straight section three APPLE II [113] undulators constitute the photon source of the ID32 beamline. The central undulator is 2.5 m long and the other two 1.6 m,

all having a period of 88 mm. The APPLE II structure consists in four arrays of permanent magnets, oriented following a specific pattern, as shown in Figure 3.1. The shape of the magnetic field inside the undulator can be controlled by acting on the vertical gap and the relative longitudinal position (phase) of the arrays. The magnetic field on the undulator axis imposes a wiggling trajectory to the electrons, which are forced to emit photons. ID32 undulators can produce photon beams with peak intensity in the 0.4 - 1.7 keV energy range, with $\sim$ 100% circular or linear (vertical, horizontal or inclined) polarisation.

The beam needs to be monochromatized to a high degree in order to be used for spectroscopy. A first filtering takes place in the *optics hutch*, where the combination of a water-cooled double mirror and a Bremsstrahlung stop removes the photons of higher energy. The beam is also collimated by the (toroidal) mirror in the horizontal direction and focused in the vertical, at the entrance slit of the beamline monochromator. Focusing the beam at the beginning (and end) of each section allows to consider the different parts of the beamline as independent. The vertical focus is critical all along the beamline because, due to the use of a dispersive monochromator and spectrometer, it is directly related to the energy resolution. On the other hand, the horizontal direction is less important, and the horizontal beam size is kept larger in order to reduce the heat load on the optics.

The monochromator set-up used for RIXS spectrocopy consists in a variable line spacing plane grating mirror (VLS - PGM) [114, 115] of the SX700 Peterson type. This configuration allows to keep the outgoing monochromatic beam parallel to the incoming one, always at the same height, no matter the energy selected. The grating consists in a plane (coated) Silicon mirror with a certain groove density, which, by diffraction, spatially disperses photons in the vertical direction according to their energy. The variable line spacing gives the grating focussing properties. The exit slit selects part of the first diffraction order of the outgoing beam, i.e. a certain range of energies, and is then refocussed onto the sample. Refocussing is done by a cylindrical mirror (horizontal direction) and a elliptical mirror equipped with mechanical benders (vertical focus). The beam size at the sample is $\sim$ 4 μm in the vertical direction and $\sim$ 60 μm in the horizontal. Therefore sub-millimeter size samples can be measured.

Two VLS gratings are available for the ID32 RIXS branch, one with an average of 800 lines/mm (for high flux and intermediate resolution) and the second with 1600 lines/mm (for very high resolution). Another VLS grating with 300 lines/mm provides a moderate energy resolution for the other ID32 branch, which hosts an X-ray magnetic circular dichroism (XMCD) endstation [116] and an open room for non-routine experiments. In this case, a

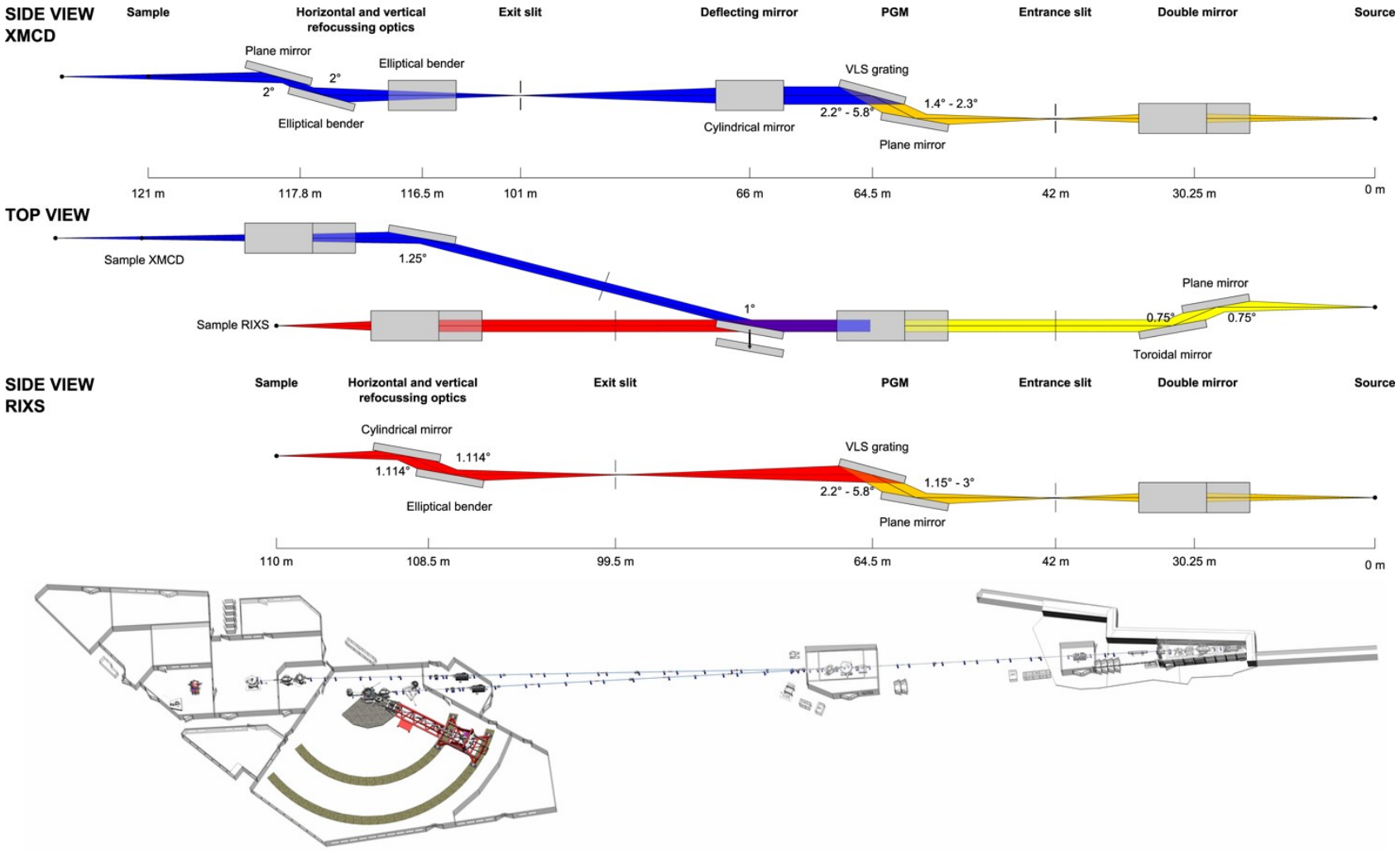

Figure 3.2: Scheme of the optical layout and floor plan of ID32 beamline.

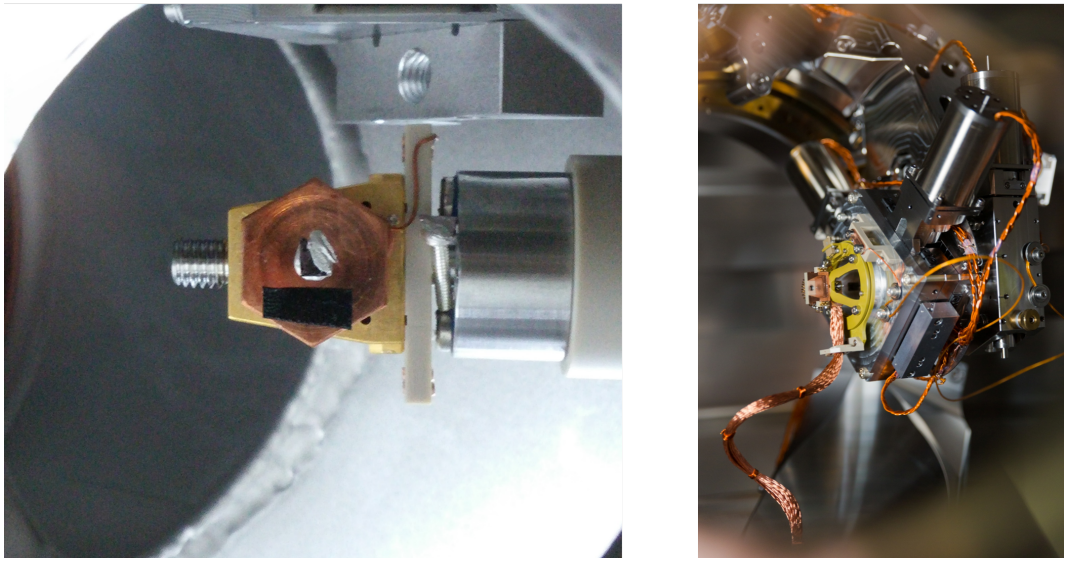

Figure 3.3: Sample mounted on a shuttle (seen through a loadlock window) and the sample stage. The sample is usually glued in the middle of the sample holder. A piece of black carbon tape is also placed on the holder to provide a purely elastic reference for the spectra.

cylindrical mirror after the grating both focuses the beam and deviates it to the exit slit of this branch. All the gratings have a ruled area of 170×25 mm^2.

The temperature control of the monochromator is of high relevance, because the beam heat load can locally modify the shape of the elements, degrading their performance. This is particularly true for the first element, the plane mirror, which takes most of the thermal load. Its temperature is therefore kept constant, by liquid Nitrogen cooling, at 125 K, at which the linear thermal expansion coefficient of Silicon is zero. For the gratings, instead, water cooling is sufficient.

The whole beamline is kept in ultra high vacuum (UHV) conditions ($\sim 10^{-10}$ mbar), mostly to avoid the damage of the optics by the interaction with high energy photons and carbon atoms present in air. Moreover, soft X-rays are highly interacting with matter and, in addition to the requirement of vacuum, no window can be put on the photons' path. ID32 is indeed a windowless beamline, whose vacuum is directly connected to the ESRF storage ring.

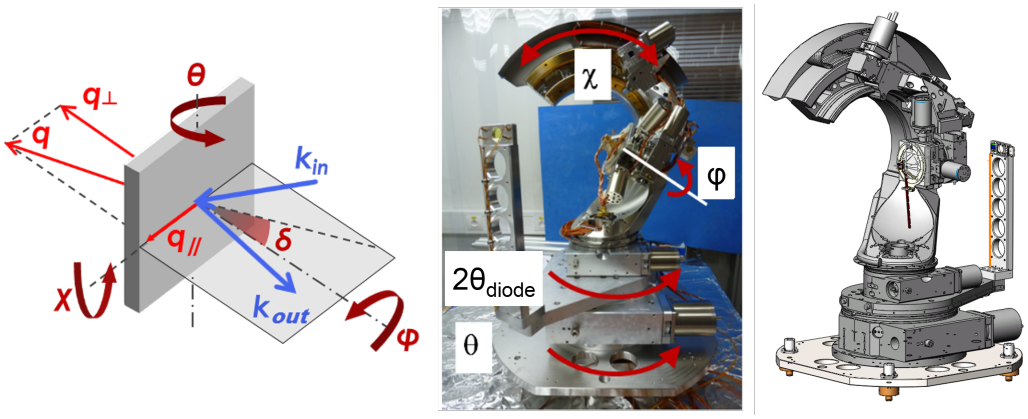

Figure 3.4: Definition of the angles and the 4-circle goniometer.

3.2 Sample stage and scattering geometry

The sample chamber is always kept in vacuum $\sim 10^{-9}$ mbar and the samples are mounted on a shuttle (Figure 3.3) which is inserted in the chamber and positioned on the sample stage via a load-lock system. The sample is electrically insulated in order to allow total electron yield (TEY) measurements with a wire connected to an ammeter that records the drain current from the sample. Low temperatures down to 20 K can be reached on the sample, thanks to a liquid Helium cooling system.

The sample stage consists in a 4-circle UHV diffractometer that allows the motorized translation (sub-μm resolution) and rotation ($\sim 0.01^\circ$ resolution) in vacuum of the sample (Figure 3.4).

The flexibility of the experimental geometry, given by the goniometer and the continuous rotation of the spectrometer, is an innovation of ID32 compared to the other existing instrumentations. It allows for the first time in soft-RIXS spectroscopy to have a complete 3D control of the momentum transferred to the sample. This is, for instance, crucial to study the dispersion relations in 3D materials or for being able to exploit geometrical dependencies in the scattering cross sections as shown in the next chapters.

To understand the scattering geometry, a careful definition of the angles is necessary. The scattering angle is the angle between the incident and the outgoing beams, i.e. between the beamline and the spectrometer axes. Following the diffraction notation, this angle is indicated as 2θ. $2\theta = 0^\circ$ defines the forward scattering and $2\theta = 180^\circ$ is the backscattering geometry. On ID32, 2θ is allowed to vary continuously from 50° to 150°, without breaking the vacuum. The plane containing the scattering angle is the scattering plane.

The angle θ is the rotation of the sample around the vertical axes and it is defined as 0° when the sample surface is parallel to the incident beam and 90° when the sample faces the

beam. Note that $\theta = \frac{2\theta}{2}$ only in specular geometry, but in general it can deviate by an angle δ from this value. χ is the rotation of the sample around the axes defined by the intersection between its surface and the scattering plane, while φ is the rotation angle around the normal to the sample surface.

3.3 The RIXS spectrometer

The purpose of the spectrometer is to collect the photons scattered by the sample in a certain solid angle and analyze their energy. In the soft X-ray range, this is typically performed by a dispersive grating. On ID32 the *single optical element scheme* [117] was adopted, meaning that both focusing and dispersing actions are provided by a concave spherical VLS grating. In order to minimize the aberrations for each energy, the grating can be moved along the spectrometer axis, changing the sample-grating distance r_1, and can be rotated to change the angle of incidence. Photons of different energies are focused in different positions by the grating, defining a focal plane. Vertical and horizontal motions of the detector allow its positioning on the focal plane, in correspondence of the energies of interests. The detector is a 2D position-sensitive CCD camera. In case of the ID32 spectrometer, the energy dispersion only occurs in the vertical direction and a monochromatic beam produces a horizontal line on the acquired images. Different energies in the beam are found as lines at different height.

The energy resolution can be improved by going far from the grating: ERIXS is indeed an extremely long spectrometer, with a grating-detector distance $r_2 \approx 8.5$ m and a sample-grating distance $r_1 \approx 2.5$ m (twice the sizes of SAXES spectrometer at Swiss Light Source [117]). At such distances, the photons hitting the detector are those contained in an extremely small solid angle, causing an enormous intensity loss. In order to increase the acceptance of the spectrometer a parabolic mirror can be inserted in the beam path before the grating (Figure 3.6) (at about 1 m distance from the sample) to collimate the photons in a horizontal fan of 20 mrad onto the detector. The vertical angular acceptance of the spectrometer, on the other hand, is about 2 mrad and is defined by the grating pitch angle ($\sim 2^\circ$), length ($\sim$ 20 cm) and distance from the sample (r_1). Two gratings are available on ERIXS: one with a groove density of 1400 lines/mm (for higher photon throughput and medium resolution) and one with 2500 lines/mm (for higher resolution).

The total resolution for spectrocopy is given by combining the resolution of the beamline and spectrometer. The first is determined by the diffraction properties of the gratings, the aperture of the monochromator's exit slit and by the aberrations and slope errors that

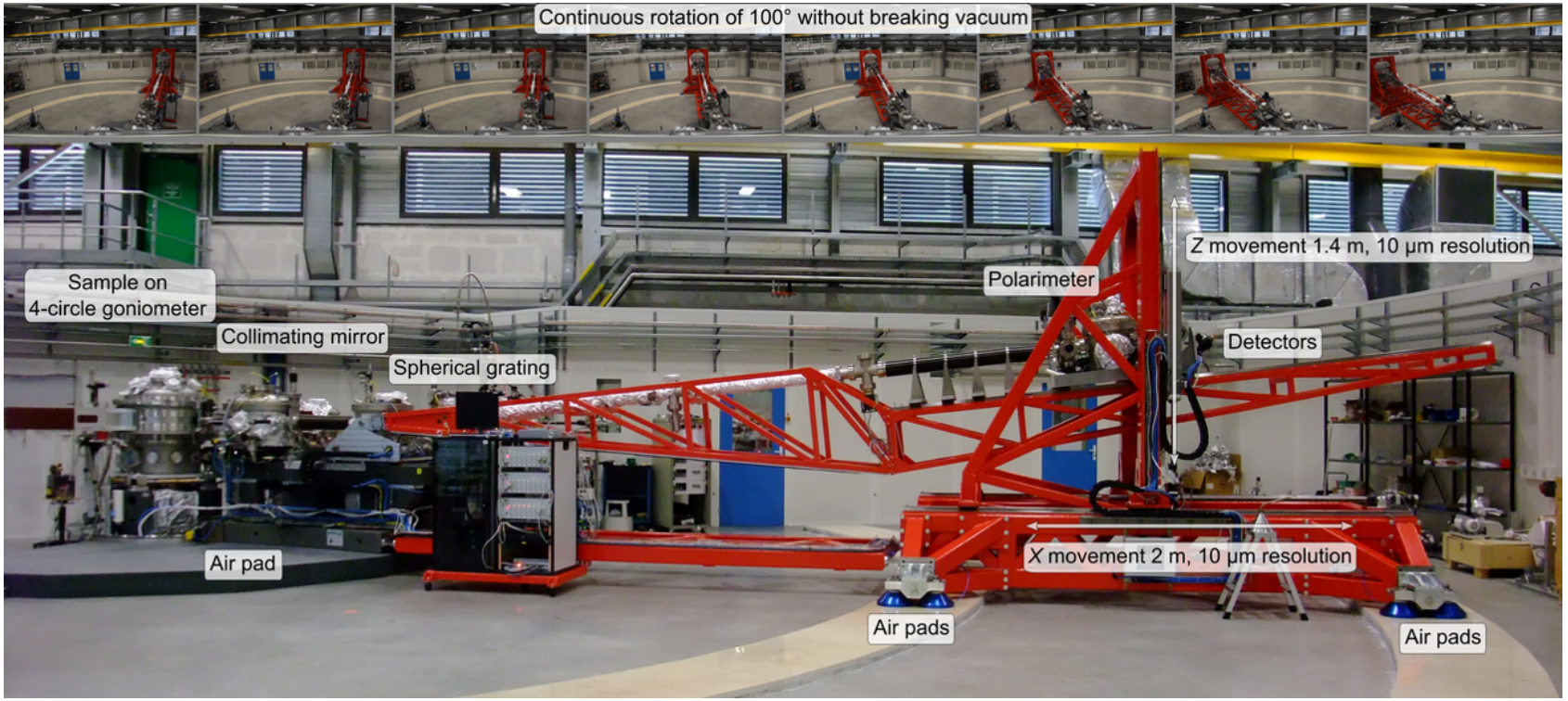

Figure 3.5: Picture of the ID32 spectrometer.

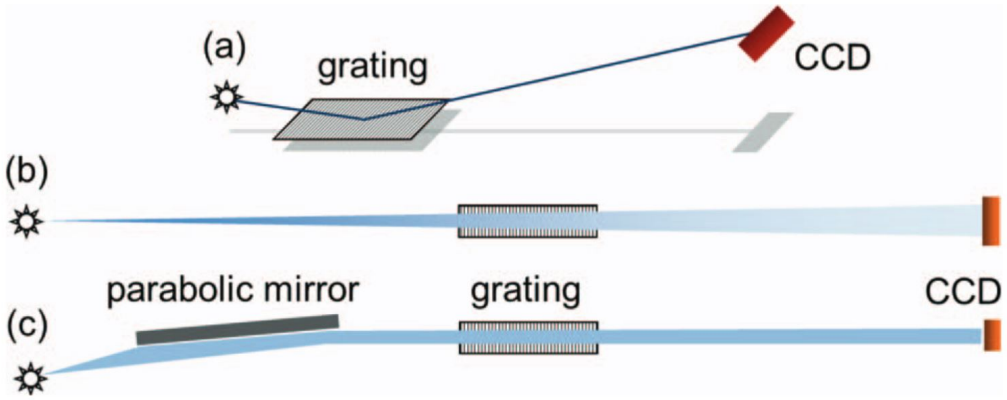

Figure 3.6: Scheme of soft-RIXS grating spectrometer based on a single optical element. Panel (a): Perspective view. Panels (b) and (c): Top view, in the absence of horizontal focusing (b) and in the case of horizontal collimation by a parabolic mirror (c). Figure from [118].

affect the focusing properties. The spectrometer resolution is given by the vertical beam size on the sample (which acts as the spectrometer's source), the diffraction and focusing properties of the grating and the detector resolution. To reduce the vertical size of the spectrometer's source, slits were used in the past between the sample and the grating. On ID32 the use of slits is unnecessary, thanks to the small focus provided by the beamline on the sample. On the other hand, the detector contribution to the resolution has become particularly important and a lot of work has been done to improve its performances, as it will be explained in the following.

The combined (beamline + spectrometer) response function is a Gaussian of $\sim$ 30 meV FWHM at the Ce M_5 edge ($\sim$ 882 eV) if both the beamline and the spectrometer are set in the high resolution mode, $\sim$ 60 meV FWHM in the high efficiency mode and $\sim$ 42 meV in the medium resolution mode that offers a good compromise between throughput and resolving power (Figure 3.7).

As mentioned above, the whole spectrometer arm can rotate around the sample chamber over 100° without breaking the vacuum. This is possible thanks to a double-differential pumped steel ribbon with a nozzle, designed by the Cinel Company. The rotation of the whole spectrometer takes place on air pads, floating on low roughness marble and granite surfaces. Two motors allow the synchronized movement of the spectrometer and the sample chamber's ribbon, to whom the scattering arm is joined with bellows.

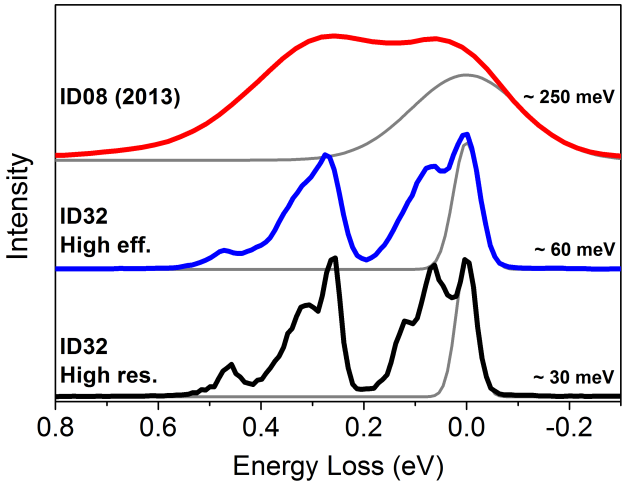

Figure 3.7: A M_5 RIXS spectrum of $CeCo_2Ge_2$ is used to compare the resolution performances of AXES spectrometer (ID08) and ERIXS (ID32). For the latter, spectra acquired in both the high efficiency and high resolution modes are presented.

3.4 Polarisation analysis in the scattered beam

In addition to the spectral analysis of the scattered photons, a simultaneous measurement of their polarisation is also possible on ERIXS, by inserting a polarisation-selective optical element (polarimeter) in the beam path. Polarimetry is not trivial for soft-RIXS and the only former study of a general scheme [1] to analyse photons' (linear) polarisation is the one of Braicovich *et al.* [118], performed on AXES spectrometer at ID08. That study set the basis for the ERIXS polarimeter, designed by G. Ghiringhelli and L. Braicovich in collaboration with ESRF.

X-ray polarimetry is performed with reflective optics. In the hard X-rays range Bragg optics are both efficient and intrinsically polarisation selective, allowing since many years hard-RIXS experiments with polarisation analysis [120]. For soft X-rays, on the other hand, decent reflectivity is achievable only with multilayer mirrors, out of the non-polarisation-selective grazing-incidence condition. Theoretically, the optimal angle of incidence for polarisation analysis is $\theta_{pol} = 45°$ (the Brewster's angle), with detection at $2\theta_{pol} = 90°$. In such a geometry the reflectivity is zero for light polarised with the $\boldsymbol{E}$ vector perpendicular to the multilayer surface, giving 100% polarisation selectivity, but the overall efficiency is extremely reduced ($r \approx 10^{-3}$) and the acquisition of RIXS spectra would be impossible. A

[1] Previously, a system sensitive to circular dichroism was implemented by Duda *et al.* [119], but its applicability was limited to the Fe L_3 edge.

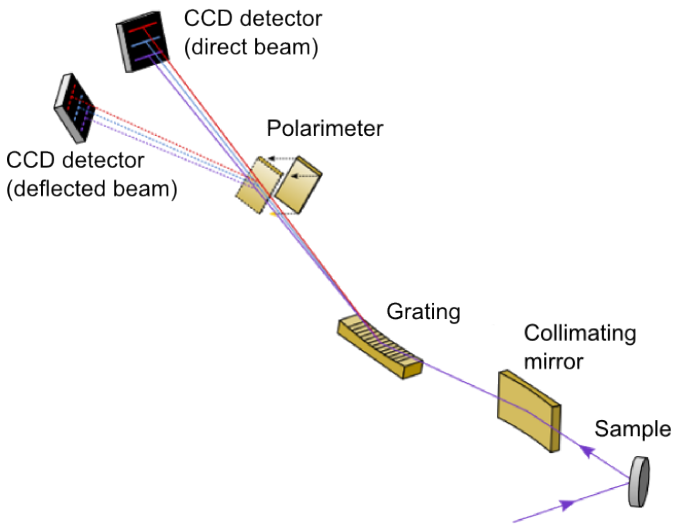

Figure 3.8: Scheme of ID32 spectrometer with the polarimeter.

compromise between intensity and polarisation selectivity was found by setting $\theta_{pol} = 20°$, resulting in an average reflectivity $r \approx 11\%$ and an efficiency ratio for the two polarisation channels ≈ 1.6.

The set-up is sketched in Figure 3.8. When used, the polarimeter is introduced in the beam path just before the detector and deflects the X-rays to another, identical detector. The spectrum acquired by this second detector is

$$I_{pol} = r_\pi \cdot I_\pi + r_\sigma \cdot I_\sigma \ , \tag{3.1}$$

where π (σ) indicates the polarisation perpendicular (parallel) to the multilayer's surface, and $r_{\pi(\sigma)}$ is the polarisation dependent reflectivity of the multilayer. On the other hand, the spectrum acquired without using the polarimeter (direct beam) is:

$$I_{dir} = I_\pi + I_\sigma \ . \tag{3.2}$$

By combining Equations 3.1 and 3.2 and knowning r_π and r_σ it is possible to find I_π and I_σ, the components of the scattered beam parallel and perpendicular to the scattering plane:

$$\begin{aligned} I_\pi &= -\frac{I_{pol} - r_\sigma \cdot I_{dir}}{r_\sigma - r_\pi} \ , \\ I_\sigma &= \frac{I_{pol} - r_\pi \cdot I_{dir}}{r_\sigma - r_\pi} \ . \end{aligned} \tag{3.3}$$

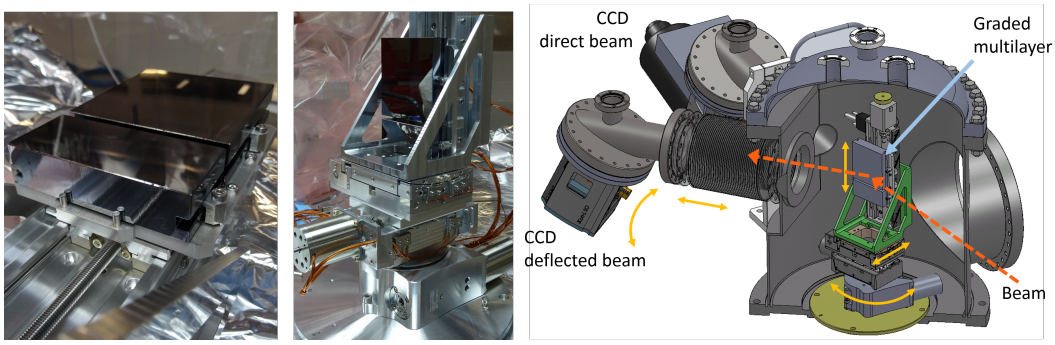

Figure 3.9: Pictures of the multilayers and drawing of the detector chamber with the polarimeter.

The values of r_π and r_σ need to be carefully estimated at the beginning of each experiment. In a real measurement, they not only account for the polarisation-dependent reflectivity of the multilayer, but include all the possible contributions that modify the intensity of the deflected beam with respect to the direct beam, like for instance a different efficiency of the two detectors. r_π and r_σ are calibrated by using a pure elastic line, as the Bragg peak of a multilayer (paying attention not to saturate and damage the detector) or the diffused scattering by a polycrystalline non-resonant material, usually carbon tape, placed in the sample position. The intensity ratios I_{pol}/I_{dir} measured with incident π and σ polarisation, give the two estimates for r_π and r_σ, respectively. Usual values for the measurements presented in this thesis are $r_\pi \approx 9.1\%$ and $r_\pi \approx 14.2\%$, in good agreement with measurements of the multilayer's reflectivity [121].

To avoid artifacts in the subtraction of the two spectra I_{pol} and I_{dir} in Equation 3.3, one must put particular attention to having the same response function (the same resolution) for the two channels. This is achieved by putting the two detectors at the same distance from the multilayer, in order to preserve the total distance from the grating, which is the focusing element. A careful calibration of the pixel $\rightarrow$ eV conversion (see next section) for both detectors is also crucial.

To better understand the design of the ERIXS' polarimeter it is worth discussing its differences with the prototype tested on AXES at ID08. The horizontal beam divergence was non-negligible in AXES, due to the absence of the parabolic collimating mirror (as in Figure 3.6, panel b) meaning that different portions of the beam were hitting the polarimeter's multilayer at slightly different angles. In order to fulfill the Bragg condition for the whole beam, the multilayer's spacing was linearly modulated in the horizontal direction, compensating for the divergence (Figure 3.10). The presence of a parabolic collimating mirror allows

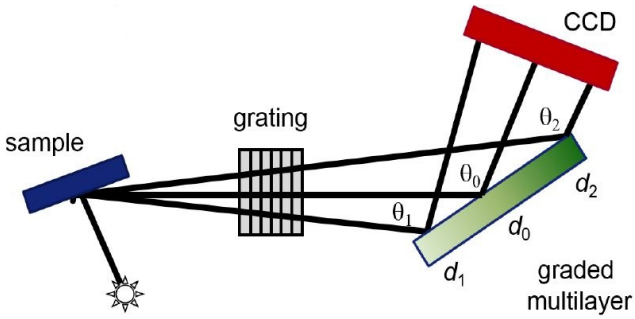

Figure 3.10: Top view of a RIXS spectrometer and polarimeter in absence of a collimating mirror. Since different portions of the beam hit the multilayer with slightly different angles θ, the spacing of the multilayer needs to be graded in the horizontal direction in order to fulfil the Bragg conditions for the whole beam.

to overcome this problem in ERIXS, since the collimated beam hits the polarimeter at a single angle and no horizontal modulation of the multilayer's spacing is needed. On the other hand, a spacing variation is introduced in the vertical direction, in order to fulfil the Bragg condition for all the energies of the spectrum (Figure 3.11), that hit the polarimeter at different heights. The multilayer's spacing is graded such that it matches the spectrometer's energy dispersion in the high efficiency setting. This allows to have a flat response function in energy and no correction needs to be introduced along the I_{pol} spectrum. This was not the case of AXES' polarimeter, whose response was rapidly decreasing already 2 eV away from the optimal energy.

Moreover, the vertical modulation of the multilayer's spacing allows to use the same multilayer in a wide range of energies, without the need of changing θ_{pol} to match the Bragg condition. To measure in a different energy range, one just needs to vertically displace the

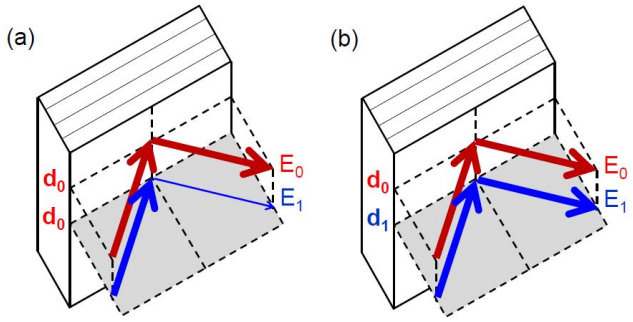

Figure 3.11: Multilayer top view in case of collimated beam (the thickness of the arrows indicates the intensity). Panel (a) - multilayer with uniform spacing: E_0 fulfils the Bragg condition of the multilayer, while E_1 (with $E_1 > E_0$) is out of tune and is reflected with lower efficiency. Panel (b) - graded multilayer: The multilayer is now tuned to E_1 in the position of the E_1 beam, thanks to a different period d, and the response function is almost flat.

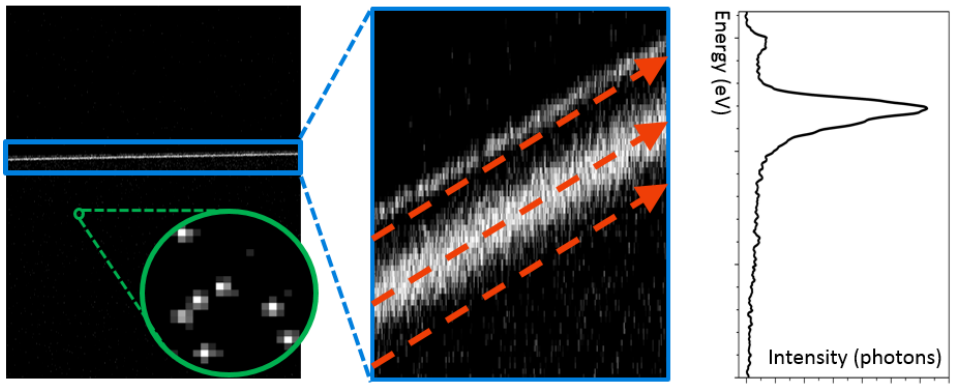

Figure 3.12: A typical image acquired in a RIXS experiment and its integration along the isoenergetic lines to get the spectrum. The zoom of the image in a low-intensity region reveals the spots produced by the X-ray photons. Each spot extends to more than one single pixel, limiting the resolution.

multilayer and find the optimal position (that is to say, the optimal multilayer's spacing) for the given energy. Two multilayers are mounted in ERIXS as shown in Figure 3.9, the larger one covering the energy range between 700 and 1000 eV and the smaller one for the energies between 450 and 650 eV.

3.5 Detection and image processing

As aforementioned, the detectors used in ERIXS are 2D position sensitive CCD cameras and the acquired images consist in horizontal lines at different heights, each corresponding to a photon energy. This allows the parallel acquisition of the whole RIXS spectrum.

For the detection of soft X-rays, that have very short penetration length in matter, thinned back-illuminated CCD cameras are needed, working in vacuum and without windows. Moreover, the low intensity of the RIXS signal requires a very uniform background, with low darkcurrent and readout noise, obtained by cooling of a high quality Silicon chip. Currently, ERIXS uses two Andor iKon-L detectors, with 2048 × 2048 pixels of 13.5 × 13.5 μm^2 size, one for the direct beam and the second to detect the beam deflected by the polarimeter. The chip is kept at -80 °C by water-cooled Peltier cells, providing negligible darkcurrent and an extremely low readout noise of 3 electrons rms at 50 kHz pixel reading frequency or 6.5 electrons rms at 1 MHz.

The usual data reduction process consists in the integration of the acquired images along the isoenergetic lines, as shown in Figure 3.12. The lines don't appear perfectly horizontal in the image because the detector is mounted slightly tilted, in order to spread the signal

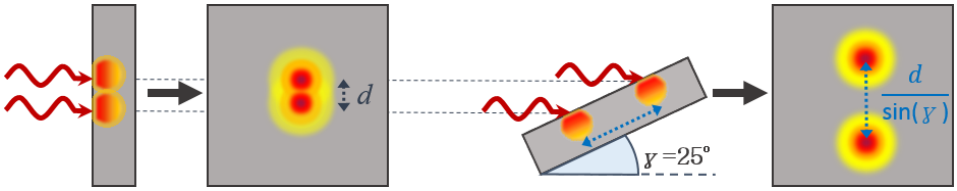

Figure 3.13: Sketch of the improvement in the effective spatial resolution for an inclined CCD. The gain in spatial resolution is $\sin\gamma$, being γ the angle between the detector's surface and the optical axis.

over multiple pixel lines and be less affected by the chip's inhomogeneities. The slope also allows to perform an oversampling of the image in smaller virtual pixels while integrating, giving a better definition of the spectrum.

After the integration, the vertical axis must be converted in energy. The conversion factor pixel → eV is obtained by measuring the changes in the position of the elastic line while gradually changing the incident photon energy.

It is clear at this point that the spatial resolution of the detector directly affects the energy resolution of the spectra. The resolution of CCD cameras for X-rays is limited by the size of the electron cloud excited by each photon absorbed in the detector. The charge cloud is generated by diffusion and electron-electron scattering processes, and has approximatively a gaussian shape of ~ 25 μm FWHM, larger than the pixel size. When the charge is collected in the pixels, each cloud produces a spot in the image spread over more than one pixel [117, 122, 123], as visible in the inset of Figure 3.12. If the detector is used without any further arrangement, its resolution alone would add a contribution of about 75 meV at the Ce M_5 edge while it has to be significantly smaller to achieve the target value of 30 meV for the total combined resolution. An incline $\gamma = 25°$ allows to reduce the detector contribution down to 30 meV (Figure 3.13), but this value is still too large and would prevent from reaching the target performances of ERIXS.

Because of its importance, a lot of effort has been put into improving the detector's spatial resolution. On ERIXS, a simple but powerful solution has been implemented, without the need of buying specific (and expensive) detectors. The idea is to use the intensity distribution in the pixels of a spot to retrieve the information about photon's impact position. This procedure must be used on each single photon's spot and it is thus named single photon counting. I have spent a significant amount of time implementing a respective algorithm and characterising the improvements in resolution with commercially available CCD detectors.

The basic assumption is that the impact position of the photon is in the charge cloud's center, which must be found by using the intensity distribution among the pixels of a spot. This approach is also called *centroiding*. Centroiding is used since a long time for photons

of higher energies, but its applicability in the soft X-rays range was limited by a low signal to noise ratio. The amount of electrons excited by a photon in Silicon is proportional to its energy. The electron-hole pair generation energy in Si is 3.65 e^-/eV, meaning that 880 eV photons generate clouds of about 244 electrons, which spread among $\sim 9-16$ pixels. The outer pixels can collect less than 10-15 electrons which is comparable to the readout noise of the electronics. Thanks to the fast advances in the detector industry, commercial CCD cameras can now reach very low noise values (3-6 electrons rms), allowing the application of centroiding techniques in the soft X-rays range [124], without the need of a detector specifically designed for single photon counting [125].

The solution implemented for the ERIXS spectrometer consists in a post-processing algorithm acting on images obtained with the normal acquisition mode. The spots are found on the image by comparing the pixels' intensities with empirical thresholds and the centroid position is assigned by a simple (but robust) center of mass calculation, i.e. weighting the pixels' positions with their intensities [122, 123]. The spots' centers are then assigned to channels of arbitrary size following the isoenergetic lines' slope. Each spot center counts for one photon and the number of photons in each channel gives the intensity of the corresponding point of the spectrum. The choice of the channels' width has to be made by a trade off between the definition-resolution of the spectrum (narrower channels) and the intensity in each channel (larger channels). Usual channel widths used to analyse ERIXS data are between 0.2 and 0.4 pixels.

Preliminary off-line tests [123, 122] proved that a spatial resolution of the images better than 6 μm can be obtained, which translates in about 7 meV energy resolution (in the ERIXS' high resolution mode). This value is negligible if compared to the beamline and spectrometer contributions, of about 20 meV each, and allowed to reach the target combined resolution of 30 meV at the Ce M_5 edge. The tests also revealed the presence of both intrinsic and random errors in the centroid reconstruction, some of which could be in principle corrected [126]. For the time being, the correction is not implemented in the analysis of ERIXS' data because the effect of these errors (less than 2 μm) is negligible if compared to the usual integration channel size (5 μm) or to the other contributions to the combined resolution.

The left panel of Figure 3.14 shows the resolution gain obtained for high resolution RIXS spectrocopy, estimate from the broadening of a pure elastic reference. Considering a pixel $\rightarrow$ eV conversion factor of 16.8 meV/pixel, the total combined resolution is improved from 43 to 30 meV when using single photon centroiding. The right panel shows the same gain in the case of the medium resolution set-up (from 68 to 55 meV, with a conversion factor of

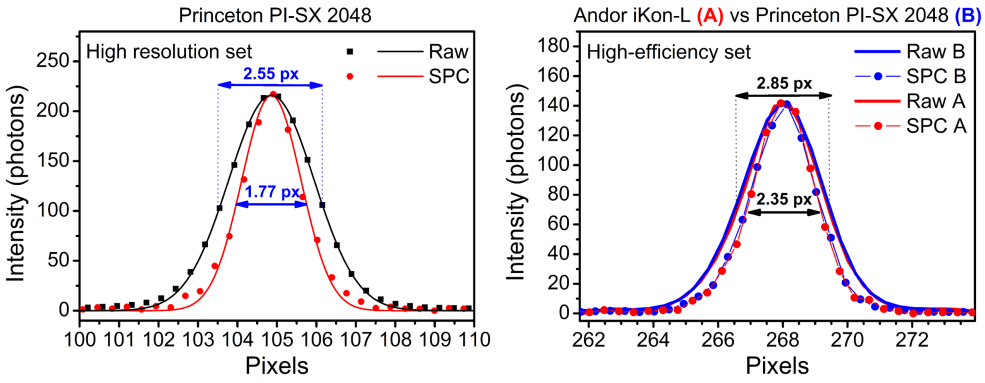

Figure 3.14: Left: Spatial resolution gain obtained with single photon counting (SPC) instead of the usual integration of raw images (Raw). The latter is rescaled to the SPC maximum in order to highlight the different broadenings. Right: Comparison of two detectors, the Princeton PI-SX 2048 and the Andor iKon-L (currently mounted on ERIXS). The resolution improvement, here shown for the medium resolution set-up, is the same for the two devices, but the latter has an higher readout frequency, allowing the reduction of the duty cycle.

24 meV/pixel). The resolution improvement is shown to be the same with two detectors, the Princeton PI-SX 2048 by Roper Scientific, which was previously mounted on ERIXS, and the Andor iKon-L. The latter can work, at the cost of a slightly higher but still negligible readout noise, at a pixel readout frequency of 1 MHz, instead of 100 kHz, and this is crucial to increase the beamline efficiency.

Single photon counting is applicable only if the photons' spots are isolated on the image, otherwise the center of mass calculation would lead to a wrong centroid reconstruction of overlapping spots. This low-photon-density requirement translates in reading the detector's image very frequently, to have few photons per acquisition. Usual exposure times are of the order of 10-30 seconds and a spectrum is obtained by summing many images (from 50 to 1000). Reading the full chip of 2048 $\times$ 2048 pixels at 100 kHz readout frequency would require 42 seconds, resulting in a very low duty cycle. On the other hand, the 1 MHz readout frequency gives acceptable readout times of about 4 seconds. This time can further be reduced by reading only a region of the image (ROI) if the useful signal is well localized as in Figure 3.12.

Another advantage of using single photon counting is a complete suppression of the detector's background, because all the base modulations do not contribute to the final spectrum, which is made by counting the number of centroids in each integration channel. This background elimination is very useful for the detection of low intensity signals or when two spectra need to be subtracted, as it happens for the polarisation analysis.

For the ID32 spectrometer, the single photon counting algorithm is now the routine way of reducing the 2D CCD images to a 1D spectrum.

Chapter 4

Full characterisation of the $4f$ levels in $CeRh_2Si_2$

The recent improvements in Resonant Inelastic soft X-ray Scattering (soft-RIXS) instrumentation open up multiple possibilities for studying the properties of condensed matter. The experimental resolution is now comparable with many low-energy excitations, which became visible in soft-RIXS spectra. Among these, the excitations between two $4f$ levels can provide much information about the relative energy, symmetry and charge distribution of the $4f$ states.

This chapter investigates the capabilities of high resolution soft-RIXS to study the crystal-field split $4f$ states of cerium ions in cerium intermetallics of the 122 family. Since this work represents the very first observation of $4f$ crystal-field features in soft-RIXS, stress will be put on the methods employed to get the information from the spectra. The example of a typical heavy fermion of the 122 family, $CeRh_2Si_2$, will be used to show and comment the steps of the data analysis, but the main outcome of this chapter are in general applicable to any cerium-based compound.

To complete the picture, the findings will be compared with results obtained with other techniques. The choice of the most important experimental settings will also be discussed, providing a further insight in the many opportunities offered by soft-RIXS spectroscopy.

4.1 Properties of $CeRh_2Si_2$

$CeRh_2Si_2$ is an heavy fermion compound belonging to the 122 family of cerium intermetallics. Its structure, showing a tetragonal D_{4h} symmetry around the cerium ion, is represented in Figure 4.1. Despite being already known as a heavy fermion system with two distinct

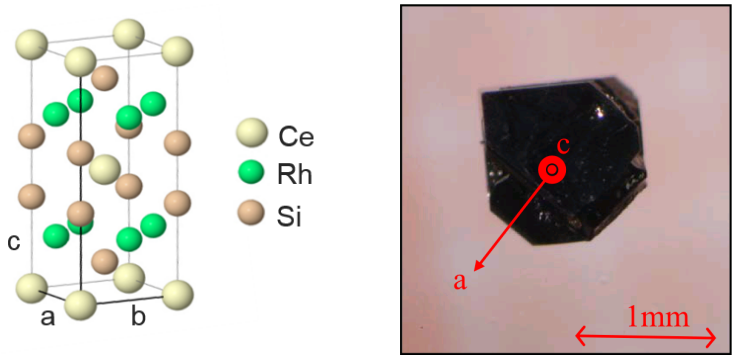

Figure 4.1: Crystal structure of cerium intermetallic compounds of the 122 family. For $CeRh_2Si_2$ $a = b = 4.09$ Å and $c = 10.18$ Å [127]. The samples grow as flat platelets with the crystallographic c axis pointing out of the surface.

antiferromagnetic orders below the relatively high Néel temperatures of $T_{N_1} = 37$ K and $T_{N_2} = 26$ K [128, 129, 130, 131], $CeRh_2Si_2$ attracted much more attention after the discovery of a superconducting phase with $p_c \approx 1.1$ GPa and $T_c \approx 400$ mK [132, 133, 134]. $CeRh_2Si_2$ was not the first heavy fermion discovered to superconduct under pressure, but this behavior was unexpected on the basis of thermopower measurements, unlike its predecessors $CeCu_2Ge_2$ and $CePd_2Si_2$ [135, 136, 133]. Since then, many studies enriched the list of its properties.

Of particular interest is the ambiguity in the nature of the $4f$ electrons [137]. On the one hand, the high magnetic ordering temperature, the large magnetic moment per Ce ion ($m_{AF_1} \approx 1.28-1.5$ μ_B [130, 129, 71] and $m_{AF_2} \approx 2.4$ μ_B [130] [1]), the large entropy [131] and the small Fermi surface [140] suggest an high localization of the $4f$ electrons. On the other hand, the quasi-elastic linewidth observed in inelastic neutron scattering spectra indicates a large Kondo scale ($T_K \approx 30$ K) and the small value of p_c implies the vicinity to magnetic instabilities; both of these observations entail a significant hybridization of the $4f$ electrons. At ambient pressure, the magnetic phase wins and masks the hybridization, whose effects are anyway present and observable in photoemission spectrocopy [88].

Despite the knowledge of the many peculiar physical properties of $CeRh_2Si_2$, the energy splittings, symmetries and charge distributions of the Ce $4f$ states are still not determined. *Ab initio* calculations [141] seem to give splittings that are too small and need comparison with experiments to restrict the value of the free parameters. Yet, due to the complex

[1] Many values of the magnetic moment can be found in literature [138, 130, 129, 71], due to: (a) different microscopic magnetic structures used to model the antiferromagnetic ordering and (b) the possible presence of magnetic fluctuations, which are integrated on a different timescale by each technique [130, 129, 71, 138]. The values presented here are considered the most reliable by the author. In particular, it must be noticed that values between $1.28-1.6$ μ_B moment per cerium ion agree with magnetic susceptibility data[139, 70, 71] for $T > T_{N_1}$ (paramagnetic region); this result is independent on the specifics of the antiferromagnetic structure and is a property of each individual site.

physics, the experimental techniques traditionally used to determine the crystal electric field (CEF) in cerium intermetallics have given contradicting results and are far from being conclusive. For example, different measurements of the dependence of the magnetic susceptibility on temperature set the CEF splittings of the $^2F_{5/2}$ multiplet to 27 and 59 meV with states Γ_7 - Γ_7 - Γ_6 in order of increasing energy[71] or 31 and 78 [70] with a Γ_7 - Γ_6 - Γ_7 order. These experiments, determining the CEF splittings only indirectly and being affected by the magnetic properties of the sample, do not always guarantee a unique result. Considering more direct techniques, an INS-XAS study [51] measured energy splittings of 32 and 52 meV and Γ_7 - Γ_7 - Γ_6 order of the states, but the hybridized 4f states give broad peaks in the spectrum, with a low contrast over the phonon background. Moreover, the energy of the observable excitations is limited to $\sim 60meV$ in INS, preventing from seeing states at higher energies. Recently a resonant photoemission [88] study measured 48 and 62 meV splittings with an order Γ_7 - Γ_6 - Γ_7 of the states. The electron removal in the final state of photoemission does not guarantee that the splittings observed are the same of the ground state and moreover the results can easily be affected by surface effects.

Therefore a technique that probes directly the CEF states' symmetry and splitting with bulk sensitivity and with a clear interpretation of the results was still needed. Soft-RIXS spectroscopy with $\sim$ 30 meV resolution, comparable to the CEF splittings, can overcome the limitation of the traditional techniques. $CeRh_2Si_2$ was therefore considered an optimal compound to perform the first soft-RIXS test, whose outcome, due to the absence of an established interpretation of its CEF, is both unbiased by previous knowledge and of high scientific interest.

4.2 From RIXS spectra to the crystal electric field

The high-resolution M_5 RIXS spectra of $CeRh_2Si_2$ are shown in Figure 4.3. Two different energies of the incoming photons were chosen, 0.3 eV before (881.7 eV) and after (882.3 eV) the first peak of the XAS (indicated in Figure 4.2 with A and C). As visible by the RIXS spectra and discussed in section 2.2 and in section 4.5 the two incident energies were chosen to enhance the signal in different spectral regions, around 0 and 300 meV energy loss, respectively. The scattering angle was fixed to $2\theta = 150^\circ$, with the crystallographic axis **a** and **c** lying in the scattering plane ($\phi = 0^\circ, \chi = 0^\circ$), **c** making the same angle with the incoming and detected beams (specular geometry, i.e. $\delta = 0^\circ$ and $\theta = 75^\circ$). Spectra were measured with polarisations of the incident beams both parallel (π) and perpendicular (σ) to the scattering plane. The spectrum at 881.7 eV and π polarisation was acquired for 8 hours,

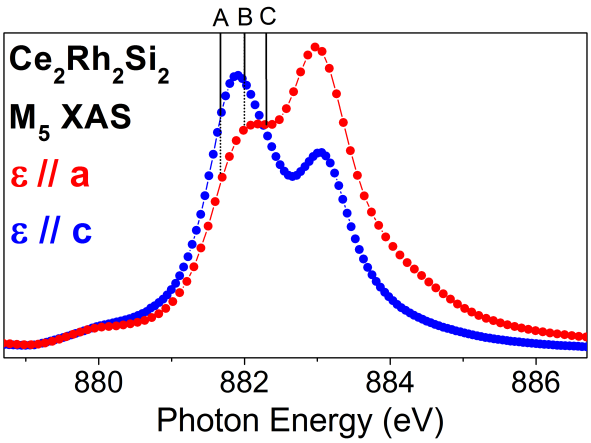

Figure 4.2: M_5 XAS spectra of $CeRh_2Si_2$ with photon polarisations parallel to the a and c axes. The photon energies corresponding to the RIXS spectra presented in the following are indicated as A (881.7 eV), B (882 eV) and C (882.3 eV).

the others for about 5 hours, with an average storage ring current of $180mA$ in uniform multibunch mode. These long acquisition times were needed due to the low count rate, of about 0.1 photons per second.

Figure 4.3 also shows the calculated spectra that best fit the data, with very good agreement. The sticks indicate the energy and intensity of the inelastic $4f-4f$ transitions, as calculated by simulations. The intensity of the elastic peak needed to be corrected in order to better fit the spectrum, because the signal at zero energy loss is influenced by contributions not considered in simulations as low-energy phonons, surface quality. It can be noticed that the peaks, representing the $4f$ levels, are split in two groups, corresponding to the $^2F_{5/2}$ (three peaks, including the elastic one, in the range $E_{loss} = 0-100$ meV) and $^2F_{7/2}$ (4 peaks at $E_{loss} = 250-400meV$) multiplets. The $^2F_{5/2}$ peaks have been broadened by a resolution-limited Gaussian of $\sim$ 35 meV FWHM, while a larger Gaussian broadening of about 60 meV (not resolution-limited) was needed for the excitations in the $^2F_{7/2}$ multiplet. A low and flat background (grey shaded area) was added to take into account the signal from excitations in the conduction band.

In the simulations, the Slater integrals were reduced to about 55% of their atomic Hartree-Fock values for the $4f$-$4f$ electronic interactions and to 88% for the $3d-4f$ interactions. These values were found by comparing experimental XAS spectra of powdered Ce^{3+} samples to simulations (without CEF), and show a negligible deviation [50] from the $\sim$ 60% and $\sim$ 80% reductions suggested in literature [51]. Similarly, the $4f$ and $3d$ spin

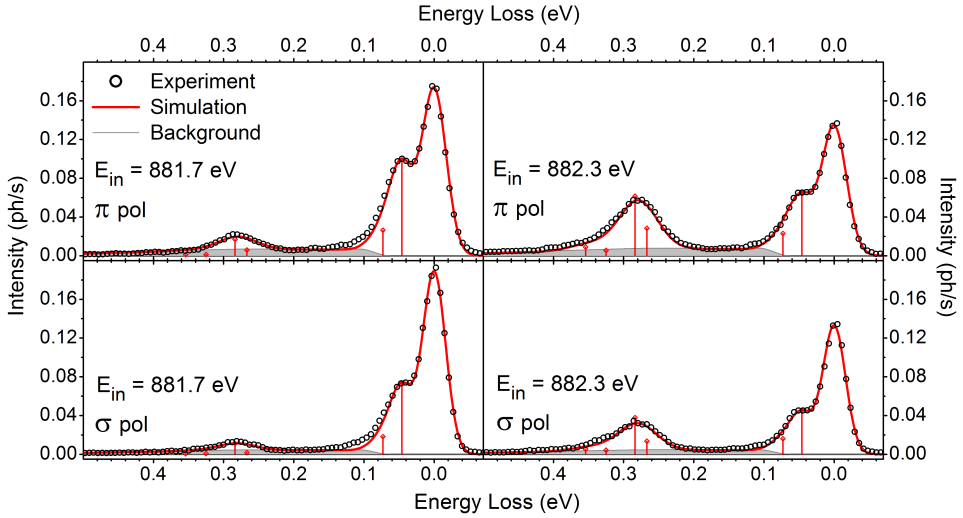

Figure 4.3: M_5 RIXS spectra of $CeRh_2Si_2$ at $2\Theta = 150°$ and specular geometry. The experimental spectra are perfectly fit by simulations with CEF parameters $\check{A}_2^0 = 60$ meV, $\check{A}_4^0 = -76$ meV and $\check{A}_4^4 = 194$ meV. i.e. with a splitting of 46-73 meV of the $^2F_{5/2}$ multiplet, with an order $\Gamma_7^1 - \Gamma_6 - \Gamma_7^2$ of the three states.

orbit interactions were respectively reduced to 87% and 96.5%. The Lorentzian linewidth of the intermediate state was estimated to be $\Gamma = 0.9$ eV by the intrinsic broadening of the XAS spectra. The CEF parameters that provide the fit of the data shown in Figure 4.3, are $\check{A}_2^0 = 60$ meV, $\check{A}_4^0 = -76$ meV and $\check{A}_4^4 = 194$ meV, resulting in a 46-73 meV CEF splitting of the $^2F_{5/2}$ multiplet and an order $\Gamma_7^1 - \Gamma_6 - \Gamma_7^2$ of the three levels.

It is important to stress once again, before facing the details of the data analysis, that the full determination of the $4f$ CEF levels can in principle be obtained with a single RIXS spectrum. This is a rather unique feature of RIXS spectrocopy, because other techniques are only sensitive to certain properties of the $4f$ levels, therefore the information gained about the CEF is never complete and may lead to wrong interpretations. A RIXS spectrum simultaneously provides not only information about the CEF levels' splittings, given by the position of the peaks, but also about their mixing, symmetry and charge-density spatial distribution. This information is held in the relative intensities of the peaks, i.e. by the cross sections of the excitations, which are highly influenced by the states' characteristics. Moreover, the dependency of the peaks' intensity on controlled experimental parameters as the incident photon energy, scattering geometry and polarisation can be also exploited to remove any residual ambiguity.

In order to relate the states' properties to the peak intensities, the comparison of the

acquired data with calculated RIXS spectra, each representative of different CEF schemes, is essential. This is a very powerful tool of RIXS spectrocopy, for which the spectrum can be calculated with dedicated codes and the absence of a complex background allows for a precise evaluation of the intensities.
The methods to retrieve the basic information from the RIXS spectra are explained in this section. The various steps of the data analysis, each revealing a specific characteristic of the CEF scheme, are discussed, eventually providing a recipe to be followed for future experiments.

4.2.1 Splitting and symmetry

The most important properties of the $4f$ levels to be determined are the energy (CEF splitting) and the J_z mixing of the states. In order to simplify the analysis one can focus on the lowest three levels ($^2F_{5/2}$ multiplet). The detailed characterization of the $^2F_{7/2}$ levels is only of secondary importance because they lie at too high energies (~ 280 meV > 3000 K) to influence the properties of the material. Moreover, this choice allows to reduce the set of CEF parameters needed to $\check{A}_2^0$, $\check{A}_4^0$ and $\check{A}_4^4$, since the higher orders of the CEF potential don't affect the $^2F_{5/2}$ levels (see section 1.2.2).

An estimate of the size of the $4f$ CEF splitting, corresponding to the distance between the peaks, can be obtained just by observing the RIXS spectra. A first intense inelastic peak is visible in Figure 4.3 at 46 meV and another less intense peak, almost covered by the tail of the first, can be located at slightly higher energies via a Gaussian fit. Since the features are overlapping, unknown parameters as the peaks' relative intensity affect the fit, which can provide only a rough estimate of the splittings (error $\sim \pm 10$ meV). This first estimate can then be optimized with the help of simulations. In fact, the calculation of the cross sections assesses the relative peaks' intensities, reducing the number of unknown variables. This leads to an iterative process between the fit and simulations, to optimize the guess on the peaks' positions and to re-calculate the cross sections; eventually providing results with an accuracy better than 2 meV. Figure 4.4 (left) compares spectra calculated with different splitting schemes, among which the $46 - 73$ meV option shows undoubtedly the best agreement with experimental data.

Knowledge of the size of the splittings, although of first importance, does not provide a full description of the CEF levels. It defines the distances between the ground and the first and second excited states, but does not tell *which* level corresponds to each of the three possible wavefunctions with symmetry Γ_7^1, Γ_7^2 and Γ_6 (see Equation 1.25). This information

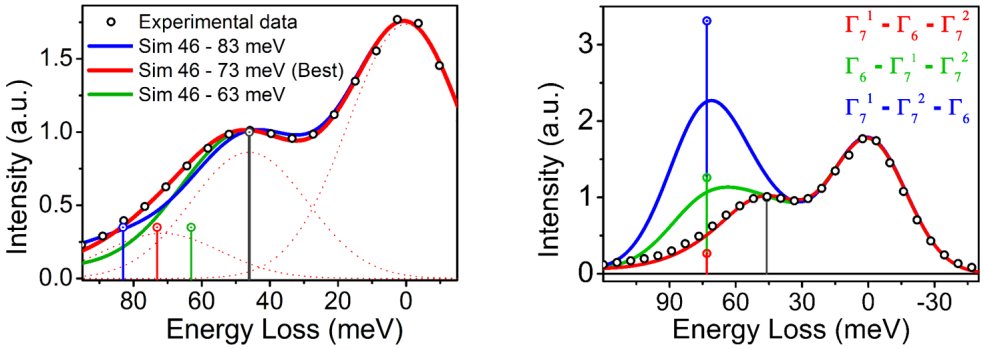

Figure 4.4: Left: Calculated spectra with different values of the CEF splittings (and same mixing and symmetries of the states); the best fit of the experimental data is obtained when the second inelastic peak is located at 73 meV. The three Gaussians represent the peaks constituting the simulated spectrum. Right: The cross sections of the transitions is affected by the states' symmetry. The best fit is obtained with a $\Gamma_7^1 - \Gamma_6 - \Gamma_7^2$ order of the states in energy.

can, however, be obtained by comparison with calculations, since the RIXS cross sections are highly affected by the symmetries of the states. The various arrangements of the three wavefunctions on the three CEF split levels give indeed different shapes of the calculated spectra, with different relative intensities of the inelastic peaks, as shown in Figure 4.4 (right). As a general trend, it shall be noticed that, when Γ_7^1 is the ground state (red and blue lines) the RIXS transitions to the excited Γ_6 level is stronger than the excitation in the Γ_7^2. On the other hand, the excitations between a Γ_6 ground state and the $\Gamma_7^{1,2}$ levels (green line) have almost equal cross sections. By comparing these observations to the experimental data, one can easily deduce that the scheme best representing the CEF splittings in $CeRh_2Si_2$ is: Γ_7^1 (ground state, 0 mev) - Γ_6 (46 meV) - Γ_7^2 (73 meV).

4.2.2 J_z mixing

The information about the energy and symmetry of the states still does not provide a full characterization of the CEF levels. In fact, even if the Γ wavefunctions are assigned to the levels, the amount of their J_z mixing is unknown. To better understand this statement, one shall refer to Equations 1.27 and 1.28, that show the relations holding, in Stevens' approximation, between the energy and mixing of the ${}^2F_{5/2}$ levels and the CEF parameters $\check{A}_2^0$, $\check{A}_4^0$ and $\check{A}_4^4$. As discussed there, the full characterization of the (unhybridized) $4f$ states is equivalent to the definition of the set of CEF parameters describing them. Trying to revert

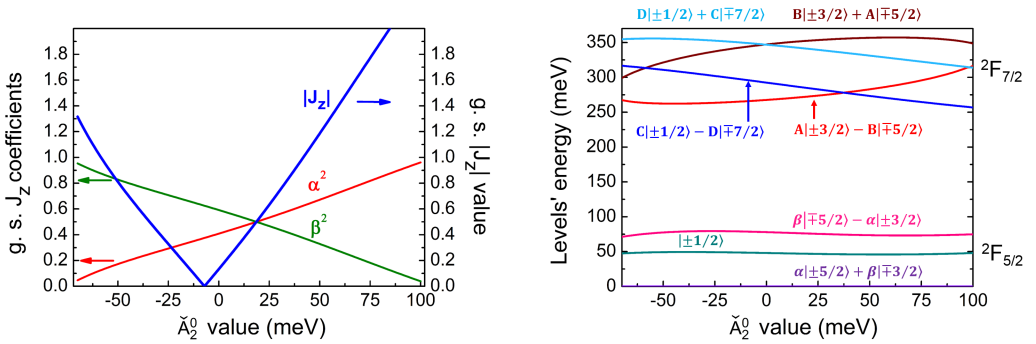

Figure 4.5: Left: Dependence on $\check{A}_2^0$ of the ground state ($\Gamma_7^1 = \alpha|\pm 5/2\rangle + \beta|\mp 3/2\rangle$)) mixing coefficients and of its J_z expectation value. Right: Full CEF scheme (including the $^2F_{7/2}$ multiplet) in function of $\check{A}_2^0$.

Equation 1.28 to find the CEF parameters as a function of the splittings, one ends up with an underdetermined system, made of two equations (to impose $\Delta E_1 = E_{\Gamma_6} - E_{\Gamma_7^1} = 46$ meV and $\Delta E_2 = E_{\Gamma_7^2} - E_{\Gamma_7^1} = 73$ meV) and three unknowns ($\check{A}_2^0$, $\check{A}_4^0$ and $\check{A}_4^4$). It is anyway possible to express two parameters as a function of the third, obtaining:

$$\begin{aligned} A_4^0 &= 7\Delta E_1 - \frac{7}{2}\Delta E_2 - \frac{12}{5}A_2^0 \\ A_4^4 &= \pm\frac{1}{10}\sqrt{\frac{7}{2}}\sqrt{-(20\Delta E_1 - 25\Delta E_2 - 12A_2^0)(20\Delta E_1 + 25\Delta E_2 - 12A_2^0)}\ . \end{aligned} \tag{4.1}$$

These relations define, as a function of $\check{A}_2^0$, sets of parameters generating the same splittings ΔE_1 and ΔE_2, but different J_z mixing of the wavefunctions. The dependence of the ground-state mixing on $\check{A}_2^0$ is shown in Figure 4.5 (left). The ground state mixing can vary continuously from a pure $|5/2\rangle$ ($\alpha^2 = 0$, $\beta^2 = 1$) to a pure $|3/2\rangle$ ($\alpha^2 = 1$, $\beta^2 = 0$) state. The one-to-one dependence that holds between $\check{A}_2^0$ and the mixing parameters makes sufficient to determine α^2 or the J_z expectation value to find $\check{A}_2^0$ and completely define the CEF. These physical quantities are measurable, for example, with XAS spectroscopy or magnetic measurements (as magnetic susceptibility).

RIXS is not directly sensitive to α or J_z, but these are not the only measurable properties affected by $\check{A}_2^0$. Figure 4.5 (right panel) shows the energy of all the 7 CEF-split $4f$ levels as a function of $\check{A}_2^0$. As expected, the energy splitting of the $^2F_{5/2}$ levels is constant, apart from a small deviation due to the limits of Stevens' approximation, that can be taken into account and corrected. Yet there are large modifications of the $^2F_{7/2}$ levels' splitting scheme. These, together with a cross section change, give sizeable effects on the RIXS spectra. Strictly speaking, for a precise description of the $^2F_{7/2}$ levels, the $\check{A}_6^0$ and $\check{A}_6^4$ parameters should be

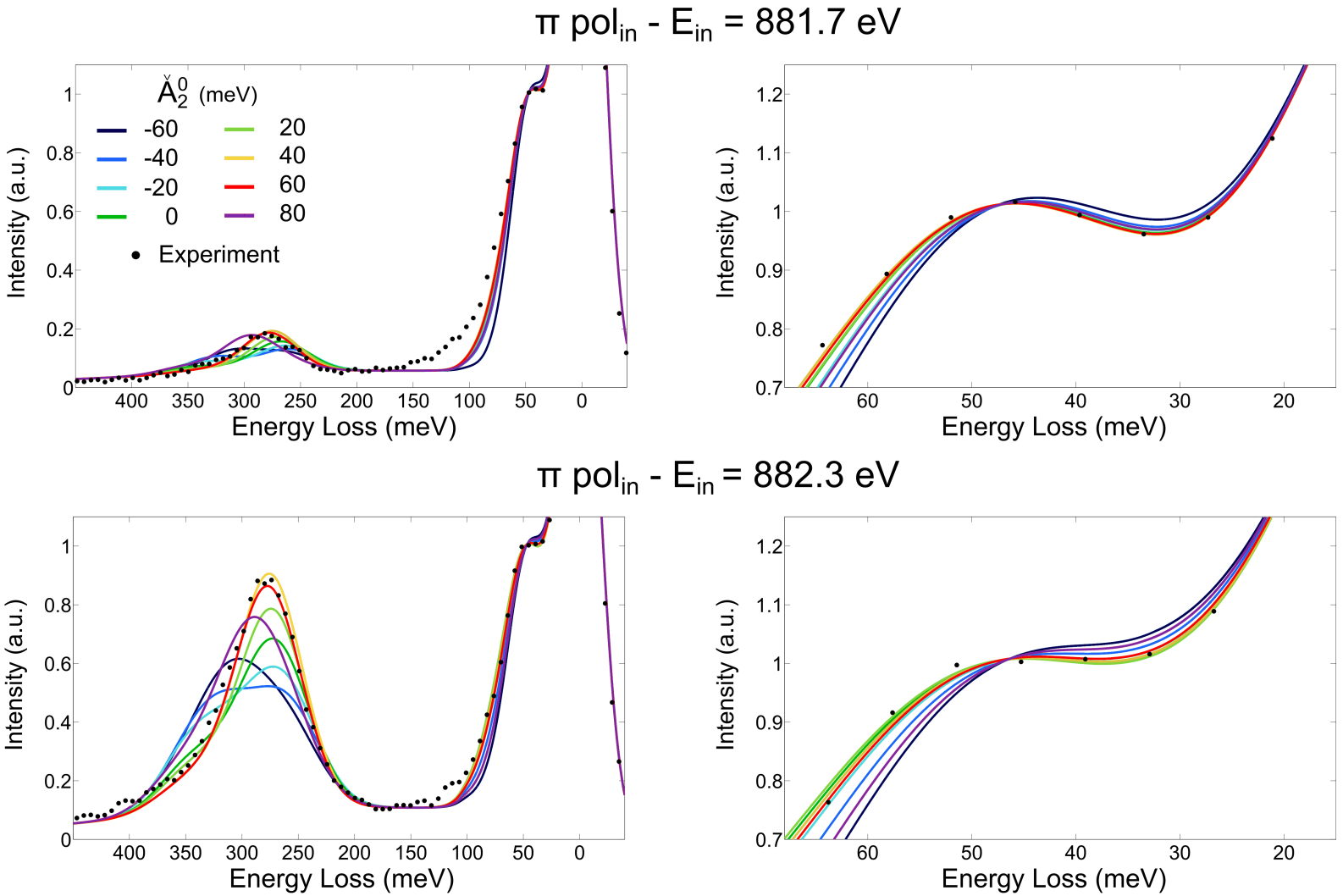

Figure 4.6: Comparison between experimental data (π polarisation) and simulations with the determined splitting scheme and various $\check{A}_2^0$ values. Looking at the excitations in the $^2F_{7/2}$ multiplet (200-400 meV), the simulations with $\check{A}_2^0 = 60$ meV best reproduce the data (left column). In the low energy region (right column), instead, the sensitivity on $\check{A}_2^0$ is much lower.

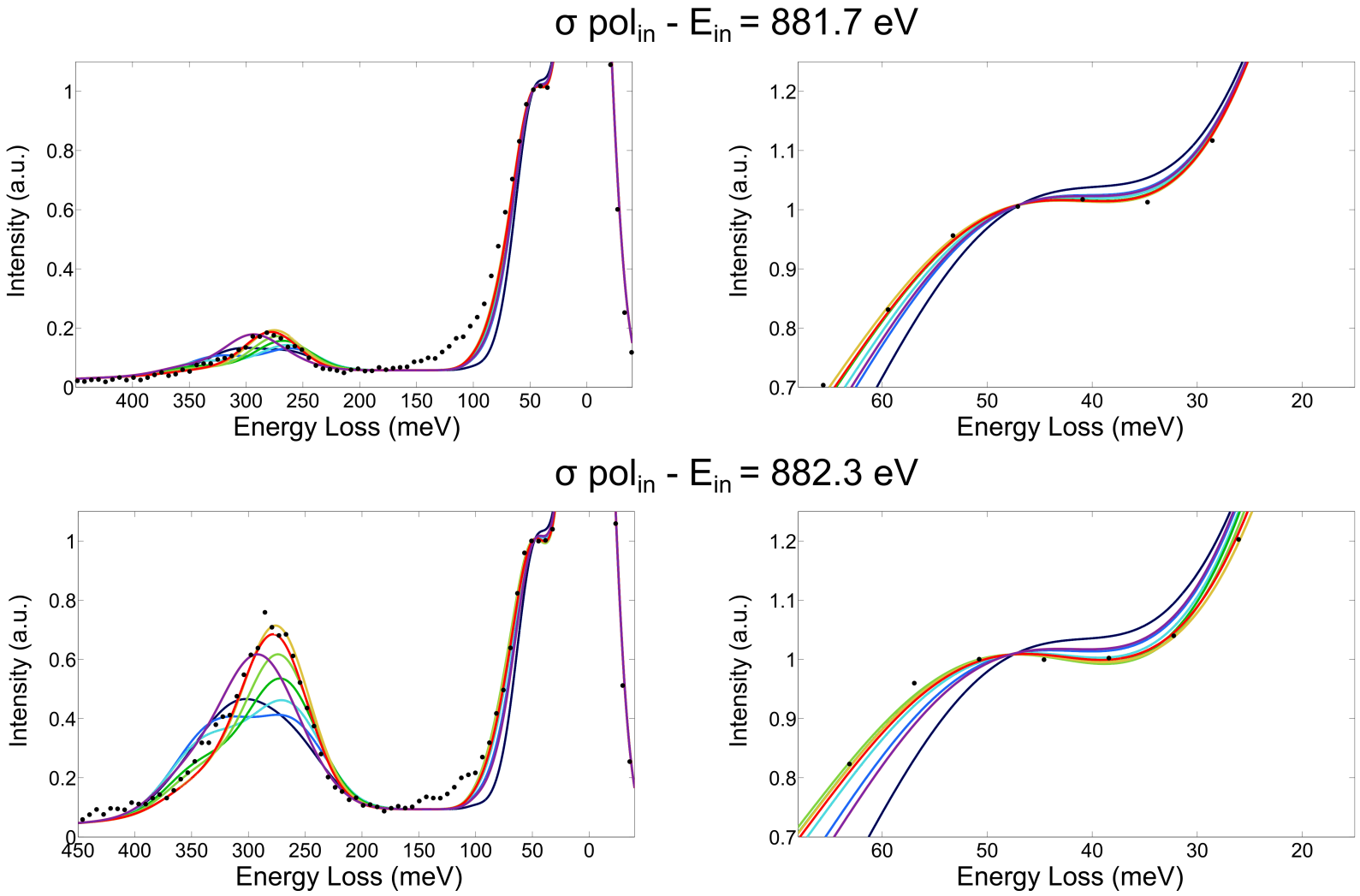

Figure 4.7: Comparison between experimental data (σ polarisation) and simulations with the determined splitting scheme and various $\check{A}_2^0$ values. Looking at the excitations in the $^2F_{7/2}$ multiplet (200-400 meV), the simulations with $\check{A}_2^0 = 60$ meV best reproduce the data (left column). In the low energy region (right column), instead, the sensitivity on $\check{A}_2^0$ is much lower.

introduced, but their higher-order effect can be neglected for the present discussion.

Figures 4.6 and 4.7 present the calculated RIXS spectra for various values of $\check{A}_2^0$ and their comparison with experimental data. The signal from the ${}^2F_{7/2}$ levels (left columns) is, as expected, highly dependent on $\check{A}_2^0$ and the best agreement with all the experimental spectra is obtained for $\check{A}_2^0 \approx 60$ meV (and thus, by Equation 4.1 $\check{A}_4^0 \approx -77$ meV and $\check{A}_4^4 \approx 194$ meV, the value of A_4^4 being increased of 8% compared to the formula in order to correct for the errors of Stevens' approximation). On the other hand, the low energy region (right columns) presents a much lower dependence on $\check{A}_2^0$, only due to a small variation of the cross sections (the small errors on the peaks' positions, due to Stevens' approximation, were corrected here). The subtle differences among the calculated spectra are of the size of the estimation errors on the peaks' position and broadening and shall not be considered crucial. However, the calculation with $\check{A}_2^0 \approx 60$ meV always provides a good fit of the data. The extra intensity visible at 100 meV is not due to CEF excitations and will be discussed later.

The low dependency of the ${}^2F_{5/2}$ signal on $\check{A}_2^0$ is actually an advantage more than a limitation. It indeed allows to study the energy splitting and symmetry of the ${}^2F_{5/2}$ levels using calculated spectra, as done in Figure 4.4, without the need of knowing the precise value of $\check{A}_2^0$, which can be determined afterwards.

Comparison with other techniques

It is interesting at this point to check the found value $\check{A}_2^0 \approx 60$ meV against data of other techniques usually employed to probe α and J_z.

The temperature dependence of magnetic susceptibility probes the magnetic moment per Ce ion, related with J_z. Two curves of the magnetic susceptibility can be found in literature, reported in Figure 4.8 with empty diamonds (from Ref. [70]) and circles (Ref. [139]). The paramagnetic region ($T \gg T_{N_1} = 37$ K) is well reproduced by the dotted curves, both calculated with the same CEF splitting and symmetry schemes determined with RIXS (46-73 meV and $\Gamma_7^1 - \Gamma_6 - \Gamma_7^2$). The dotted grey lines in Figure 4.8 are obtained with $\check{A}_2^0 = 60$ meV, which gives a set of parameters identical to the one derived above from the RIXS data. On the other hand the calculation of black curves needed, in order to reproduce the larger magnetic anysotropy, a slightly higher value of the parameter $\check{A}_2^0 = 76$ meV (in this second case $\check{A}_4^0 = -116$ meV and $\check{A}_4^4 = 166$ meV). The corresponding values of J_z, 1.41 and 1.79, are in good agreement with the magnetic moment per cerium ion measured by other techniques ($m_{AF} = g_J J_z \mu_B = 6/7 J_z \mu_B = 1.2 - 1.52 \mu_B$) [71, 129, 130].

The measurements of the magnetic properties therefore confirm, within the experimental uncertainties, the results found by the analysis of above. It is worth mentioning that in Ref.

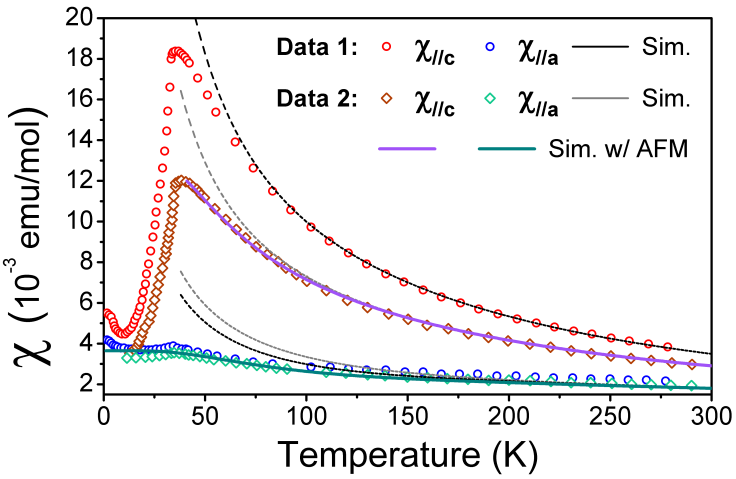

Figure 4.8: Temperature dependence of the magnetic susceptibility from Refs. [139] (Data 1) and [70] (Data 2) and corresponding fit performed with the CEF scheme found by the RIXS data and, respectively, $\check{A}_2^0 = 76$ meV and 60 meV. An exchange field along c was introduced to better reproduce the low-T region, with a value of $H_{exc} \sim -9$ meV for the $\chi_{\|c}$ simulation (violet line) and ~ -37 meV for $\chi_{\|a}$ (teal).

[70] a scheme $\Gamma_7^1 - \Gamma_6 - \Gamma_7^2$ with 31-78 meV splittings (instead of 46-73 meV) were supposed by the fit of the same magnetic susceptibility curve of figure Figure 4.8. The errors on the splitting could be due to the lower sensitivity to the excited levels, whose thermal population is still low in the measured temperature range.

To complete the discussion about the magnetic susceptibility data, it must be noticed that the fit can be improved in the low-T region by introducing a mean magnetic field along the c axis to reproduce the exchange interactions leading to the AFM magnetic order [128]. The exchange field was set to ~ -9 meV to calculate $\chi_{\|c}$ (violet line) and ~ -37 meV for $\chi_{\|a}$ (teal). The factor ≈ 4 between the two values is similar to the ratio between the two molecular field parameters λ_a and λ_c used in Ref. [70]. Another technique recently employed to determine the (ground state) J_z mixing is X-ray absorption spectroscopy. Data from Ref. [51] are shown in Figure 4.9, together with simulations with varying $\check{A}_2^0$ values (and therefore varying J_z mixing α^2 of the ground state). The calculation with $\check{A}_2^0 \approx 50$ meV provide a good fit of the data, thus not disproving the value $\check{A}_2^0 \approx 60$ meV found above with RIXS and magnetic susceptibility. But the quality of the fit improves going towards lower values of $\check{A}_2^0$. In particular, the spectrum with polarisation $\epsilon \parallel c$ is better fit, in the M_5 (880-885 eV) region, by the calculation with $\check{A}_2^0 = 20$ meV. This value would be in agreement with the results of Ref. [51], that lead to a mixing $\alpha^2 = 0.53$. However it should be remembered that

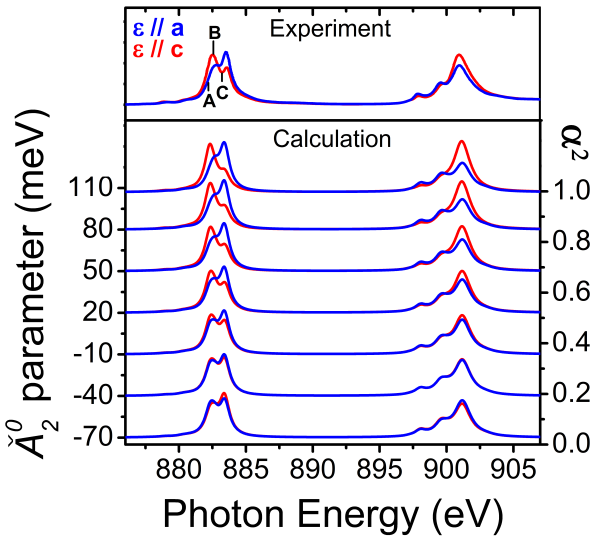

Figure 4.9: XAS experimental spectra from Ref. [51] and calculations with the CEF levels' splitting and symmetry found in this work and varying $\check{A}_2^0$ and the mixing α.

the XAS spectra are affected by both the magnetic order (the experiment was performed at 18 K $< T_{N_2} =$ 26 K $< T_{N_1} =$ 37 K) and the mixed valence of $CeRh_2Si_2$. Therefore, after considering the XAS experimental uncertainties and the small change of the calculated spectra in the range 20 meV $< \check{A}_2^0 <$ 80 meV, it's safe to say that XAS spectroscopy's results are compatible enough with those of RIXS spectroscopy.

To conclude the comparison, the XAS-INS study of Ref. [51] gave splittings 30 - 52 meV and a scheme $\Gamma_7^1 - \Gamma_7^2 - \Gamma_6$ of the CEF levels, in clear contrast with the RIXS data presented in the previous section which in turn agrees well with the findings based on magnetic susceptibility and photoemission measurements. A possible reason for this disagreement could lie in the limitations of XAS and INS. XAS probes the ground state's mixing, while the excited levels can be accessed only by thermal population, thus indirectly. Unfortunately, the magnetic ordering, the splittings and the excited levels' symmetry all give different temperature dependencies of the spectra, difficult to disentangle. On the other hand, the INS spectra can probe only a limited range of excitation energies (in that paper, $E_{Loss} < 60$ meV) and the determination of the peak's position can be affected by the phonon background subtraction.

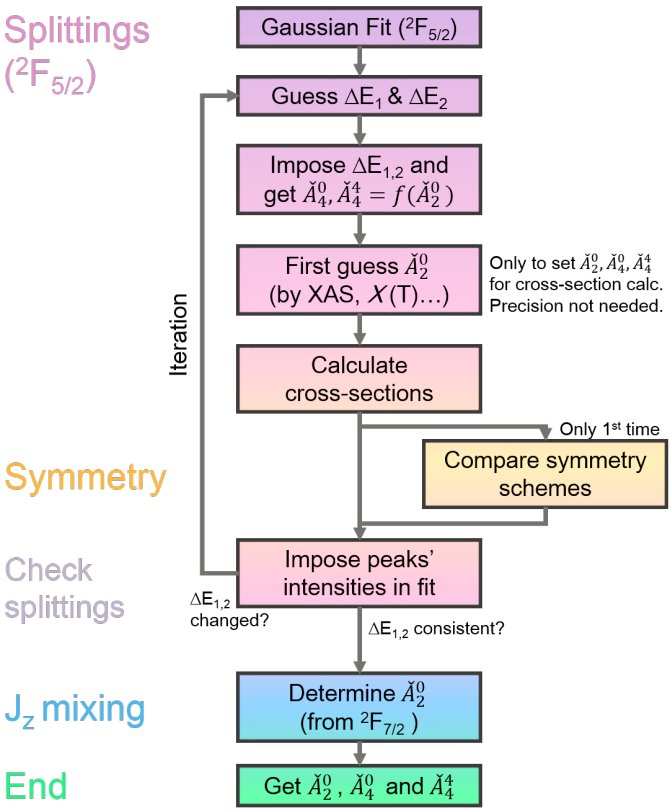

Figure 4.10: Flowchart summarizing the procedure for determining the CEF parameters from the RIXS spectra.

4.2.3 Procedure for the determination of the crystal electric field parameters

It is useful at this point to summarize the procedure employed to get the CEF parameters from the RIXS spectra (Figure 4.10). One should at first focus on the three $^2F_{5/2}$ levels, in order to reduce the number of variables. A first guess of the splittings ΔE_1 and ΔE_2 can be found by fitting the experimental data with three resolution-limited gaussians and thus estimating the position of the two inelastic peaks. The values of the energy splitting allow to reverse the expressions of $E_{\Gamma_7^1}$, $E_{\Gamma_7^2}$ and E_{Γ_6} in Equation 1.28 and get $\check{A}_4^0$ and $\check{A}_4^4$ as a function of $\check{A}_2^0$. Since the symmetries are not assigned yet to the levels, three expressions are obtained for each of the two parameters, corresponding to the three possible schemes $\Gamma_6 - \Gamma_7^1 - \Gamma_7^2$, $\Gamma_7^1 - \Gamma_6 - \Gamma_7^2$ and $\Gamma_7^1 - \Gamma_7^2 - \Gamma_6$.

The determination of the symmetry can be performed by comparing the relative intensity of the inelastic peaks with cross section calculations (Figure 4.4, right panel). To do so, one needs to make a first guess of $\check{A}_2^0$, from which $\check{A}_4^0$ and $\check{A}_4^4$ are obtained. The value of $\check{A}_2^0$

can be determined, for example, by previous knowledge of the magnetic moment per Ce ion, magnetic susceptibility or by the XAS spectrum, which is always acquired during RIXS experiments (Figure 4.5, 4.8, 4.9). These techniques may also provide a first guess of the ground state symmetry. Since, as shown in Figure 4.6 and 4.7 (right columns), the relative cross section of the transitions within the ${}^2F_{5/2}$ multiplets are almost independent on $\check{A}_2^0$, the precise determination of its value is not critical at this stage.

The calculated cross sections provide constraints for the peaks' intensities to be used in a new gaussian fit of the experimental spectrum. If this second fit provides values of the splittings different from before, the procedure shall be iterated until self-consistency is achieved.

Once the splittings and symmetries of the levels are determined, the value of $\check{A}_2^0$ can be obtained by comparing the ${}^2F_{7/2}$ spectral shape of simulations and experimental data (Figure 4.6 and 4.7, left columns). Eventually, the $\check{A}_4^0$ and $\check{A}_4^4$ parameters are fixed by plugging $\check{A}_2^0$ into Equation 4.1.

4.3 RIXS with polarisation analysis

In the previous section, all the main properties of $4f$ levels (namely the splitting, symmetry and J_z mixing) have been determined from the study of (unpolarised) RIXS spectra. More information can be obtained from RIXS spectra by analysing the polarisation of the scattered beam.

4.3.1 Determination of wavefunction orientation in the ab plane

When substituting the value of $\check{A}_2^0$ in Equation 4.1, two solutions with opposite signs are possible for $\check{A}_4^4$. This occurs because the states energies in Equation 1.28 only depend on $(\check{A}_4^4)^2$ and are therefore insensitive to its sign. The same holds true for the J_z mixing, since in this case the measured quantity is α^2, which only depends on the square of $\check{A}_4^4$ (see Equation 1.27). On the other hand, $\check{A}_4^4$ determines the sign of α and therefore the sign of the linear combination of the Γ_7 wavefunctions. This affects the states' angular distribution, which rotates 45° degrees in the crystal ab plane (as shown at the top of Figure 4.11).

The orientation of the states in a symmetry higher than twofold cannot be investigated by the standard dipole-based techniques (as INS, XAS, $\chi(T)$, ...). Resonant Inelastic X-ray Scattering, being a second order process, is not constrained by dipole symmetry and can therefore access the information on the states' orientation. This is particularly clear with polarisation analysis of the scattered photons. If one calculates the RIXS spectra

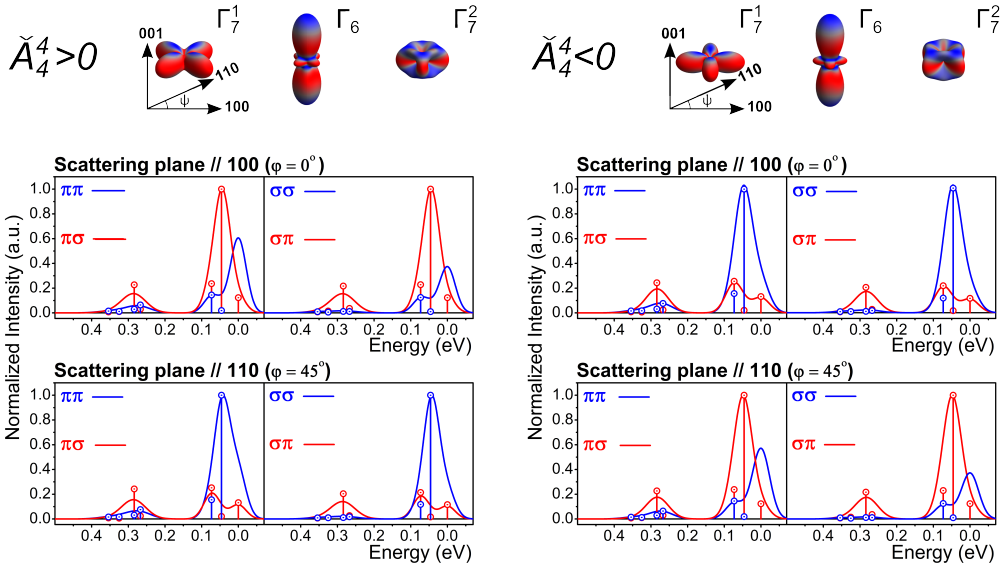

Figure 4.11: Spatial distribution of ${}^2F_{5/2}$ wavefunctions for positive and negative $\check{A}_4^4$ and corresponding simulated spectra with polarisation analysis, for both π and σ incident polarisations and two orientations of the sample relative to the scattering plane ($\varphi = 0°$ and $\varphi = 45°$). The energy of the incident photons was set to the first peak of the XAS spectrum, i.e. 882 eV (labelled as B in Figure 4.2). $2\theta = 150°$, $\chi = 0°$.

for all possible polarisation channels they show indeed a strong dependence on the states orientation. This is shown in Figure 4.11. For $\varphi = 0°$, i.e. the (100) axis in the scattering plane (upper row of spectra), the strongest feature, due to the transition $\Gamma_7^1 - \Gamma_6$ at 46 meV, is found in the crossed-polarisation channels ($\pi\sigma$ and $\sigma\pi$) for $\check{A}_4^4 > 0$ (left) and in the non-crossed channel for $\check{A}_4^4 < 0$ (left). On the other hand, all the other cross sections are approximately constant. Note that the Γ_6 state is almost insensitive to the sign of $\check{A}_4^4$. It has an almost purely $J_z = |\pm 1/2\rangle$ character, which makes it invariant under rotations around the c axis. The two Γ_7 states instead are characterized by a C_4 rotational axis and are both strongly affected by the 45° rotation due to the sign of $\check{A}_4^4$. This dependence on the states' orientation is further confirmed by the spectra in the lower row of the Figure, which shows that a rotation of the crystal of 45° degrees around the c axis ($\varphi = 45°$) is equivalent to changing the sign of $\check{A}_4^4$.

Comparing these simulations to the RIXS data (Figure 4.12) they are in perfect agreement for $\check{A}_4^4 > 0$, for both sample orientations and polarisations. This result is in line with the orientation of the ground state found with Non-resonant Inelastic X-ray Scattering (NIXS) by Willers *et al.* on the ambient-pressure superconducting parent compound

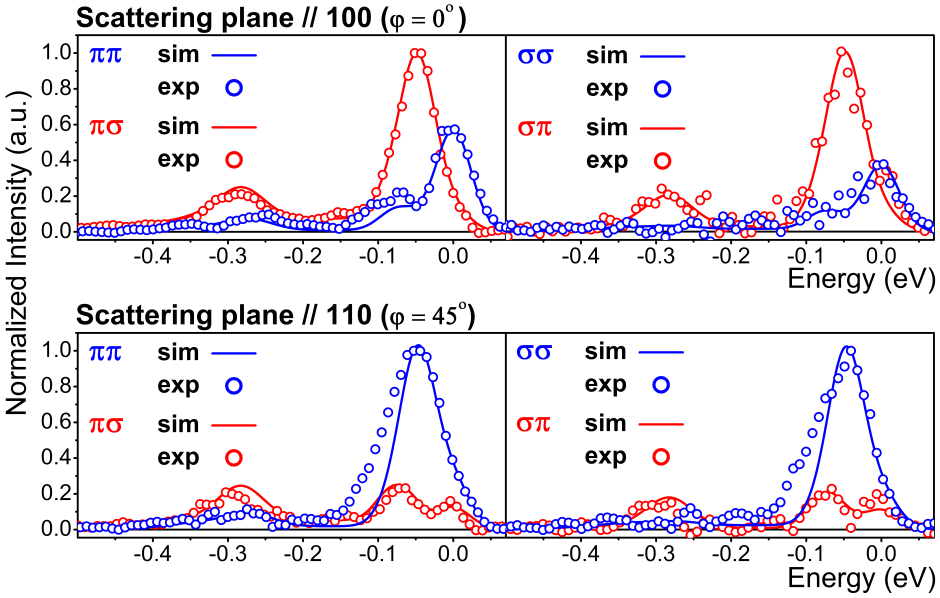

Figure 4.12: M_5 RIXS data and simulations ($\check{A}_4^4 > 0$) with polarisation analysis of the scattered beam. $2\theta = 150°$, $\chi \approx 0°$, $\delta \approx 0°$, $E_{in} = 882$ eV. Spectra with incident π polarisation have been acquired for 12 hours each, while spectra with σ polarisation for 3 ($\varphi = 0°$) and 6 hours ($\varphi = 45°$). The experimental resolution was lowered to 60 meV to increase the photon flux. The storage ring was operating at 90 mA in 16 bunch top-up filling mode.

$CeCu_2Si_2$ [43]. Furthermore, thanks to their different polarisation dependence, the $^2F_{5/2}$ peaks can be easily distinguished in the experimental spectra despite the lower resolution (60 meV) and their positions further confirm the splittings determined above.

Interestingly, the simulations correctly reproduce also the intensity at zero energy loss for the crossed-polarisation channels (red lines). This channel is indeed free of the contributions of phonon excitations and surface reflections, since these two processes don't rotate the polarisation. On the contrary, the elastic intensity of the non-crossed channel needed as usual to be corrected to better fit the data. The non-crossed elastic contribution was anyway reduced by cleaving the sample in vacuum and slightly misaligning the sample relative to specular geometry ($\delta = 0°$, $\chi \approx 0°$).

4.3.2 Other spectral features

The non-crossed spectra in Figure 4.12 show some extra intensity around 100 meV, which is not reproduced by the multiplet calculations. The residuals, after smoothing, are shown in

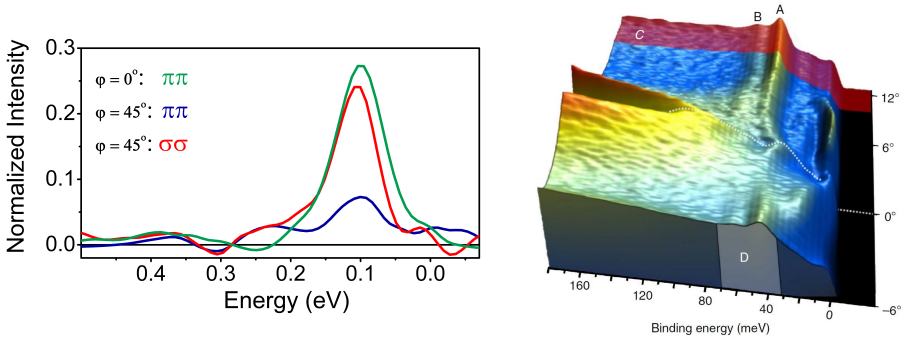

Figure 4.13: Left: Residuals (smoothed) of the fit in Figure 4.12 showing the presence of an extra feature at 100 meV, in the non-crossed channel. Right: The energy position of this feature agrees well with the energy of the hybridized Rh4d-Ce4f states seen in ARPES [88].

Figure 4.13. A similar behavior was visible in the zoom of the unpolarised high-resolution data of Figures 4.6 and 4.7, left column.

Since this extra feature appears in Figure 4.12 in the non-crossed polarisation channels ($\pi\pi$ and $\sigma\sigma$), while it is completely absent in the crossed channels ($\pi\sigma$ and $\sigma\pi$), it cannot be correlated to any of the ff transitions. Moreover, it cannot arise from magnetic excitations, since these rotate the photons' polarisation to fulfill the angular momentum conservation, giving a signal in the crossed channel [118].

Due to its polarisation dependence, this extra feature could be assigned to phonon or charge excitations. Electronic conduction bands originated from Rh 4d states and strongly hybridizing with the Ce 4f states have been observed by photoemission [88] to start at about 100 meV and disperse towards higher energies (see Figure 1.10). The 100 meV peak can therefore arise from electronic excitations, possibly of charge transfer (CT) nature, into the 4d states. This provides also an explanation for the slowly varying background introduced to better fit the data (e.g. in Figure 4.3), which, starting at $\sim$ 100 meV, could be due to higher energy excitations in the dispersing 4d band.

4.4 Temperature dependence and magnetism

To avoid the thermal population of the excited levels, which would give additional peaks in the spectra, RIXS data are usually acquired at cryogenic sample temperatures. This was also found to prevent radiation damage effects. Obviously, the properties of the sample at the measuring temperature must be considered, because different sample phases (e.g. heavy fermion, Kondo region, magnetic order...) may give rise to different spectral features.

In the specific case of $CeRh_2Si_2$, data were acquired at $T_{\text{sample}} = 25$ K, below $T_{N_1} = 37$ K, at

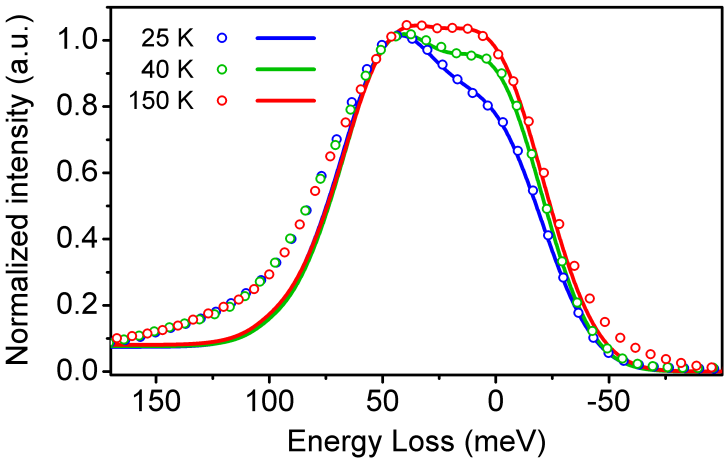

Figure 4.14: RIXS spectra of $CeRh_2Si_2$ at three different temperatures across the AFM transition, acquired with $2\theta = 150°$, $\delta = 15°$ and σ polarisation. No temperature dependence is visible in the inelastic part, while the elastic peak grows with temperature, possibly due to an increased diffuse scattering. Simulations without antiferromagnetic ordering fit equally well the three spectra, confirming that our analysis is not affected by the magnetism. Calculations were performed considering the Boltzmann population of excited levels which was always lower than 2.8%.

which the antiferromagnetic phase (AFM) sets in. In general, collective magnetic excitations (magnons) or further $4f$ levels' splittings (induced by the internal magnetic field) arise in presence of magnetic ordering.

M_5 RIXS spectra acquired at 25 K (AFM), 40 K (phase transition) and 150 K $\approx 4T_{N_1}$ (disordered phase) are presented in Figure 4.14. They show a perfect overlap in the inelastic region ($E_{loss} > 25meV$), meaning that, within the present experimental resolution (here $\sim$ 50 meV), no magnetism-induced modification of the CEF levels can be observed. Therefore, the results of this chapter are not affected by the antiferromagnetic ordering at 25 K. On the other hand, there is a relevant increase of the (quasi) elastic intensity with temperature. Magnetic excitations in $CeRh_2Si_2$ can be compatible with this energy range [51], but their study is impossible because other effects may dominate the temperature dependence of the quasi-elastic peak. Kondo-related effects might be present, as well as increased atomic vibrations, which give additional low energy features and a stronger diffuse scattering.

Spectra calculated using the usual CEF parameters (solid lines in Figure 4.14) fit the experimental data with the same accuracy at the three temperatures, further confirming the absence of inelastic magnetic features. As usual, the calculated elastic intensity needed to be corrected. However, the goodness of the resolution-limited Gaussian fit between 0 and

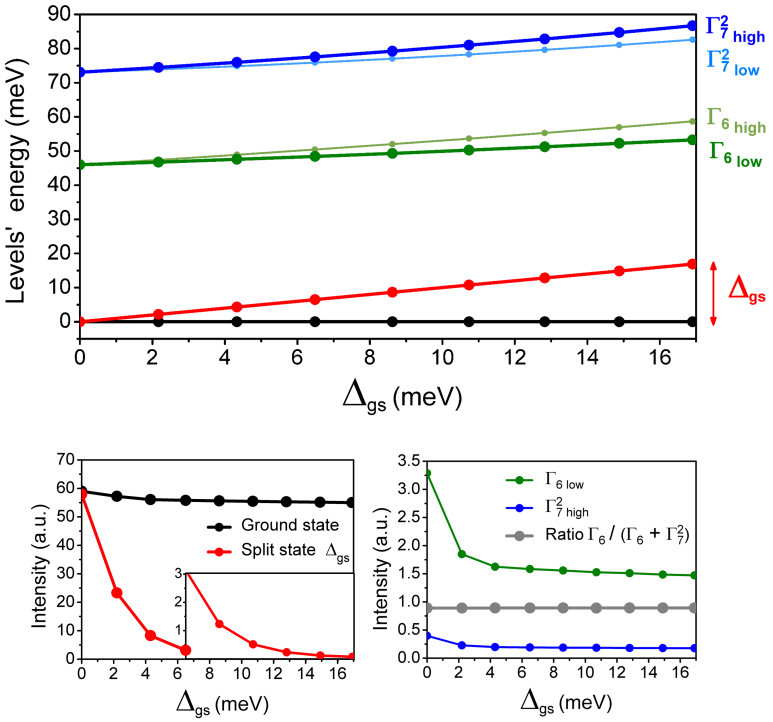

Figure 4.15: Effect of AFM order on the energy of the 4f levels and the RIXS cross sections. The plots are shown as a function of the ground state splitting Δ_{gs} induced by the magnetic exchange field along c. Top panel: Splittings of the lowest $4f$ CEF levels. The levels giving a non-negligible contribution to the RIXS spectra at $2\theta = 150°$, $\delta = 15°$ and σ polarisation (experimental conditions of Figure 4.14) are indicated by thicker lines and dots. Bottom panels: calculated cross sections for the possible tansitions.

50 meV doesn't suggest the presence of additional features in this energy range. At 100 meV the quality of the fit is again strongly affected by the broad CT peak, whose relative intensity is higher in the present scattering geometry. This could be mostly due to a relative reduction of the cross section for CEF excitations when going off-specular ($\delta = 15°$).

Although no magnetism-related effect is observed in RIXS spectra with the present resolution, it is anyway interesting to understand what could be expected, with the help of calculations. In the simplest approach, an interaction with a magnetic field along c , representing the internal exchange field aligning the moments [130], is added to the single-ion Hamiltonian. The field induces a Zeeman splitting of the $4f$ levels, shown in the top panel of Figure 4.15. The results are plotted as a function of the ground state splitting Δ_{gs} produced by the magnetic interaction. Based on INS data [51], on our RIXS measurements and on the fact that $T_{N_1} = 37$ K $\approxeq 3$ meV, the ground state splitting should be relatively small, let's say $\Delta_{gs} < 10meV$. The splitting of the higher CEF states is negligible in this

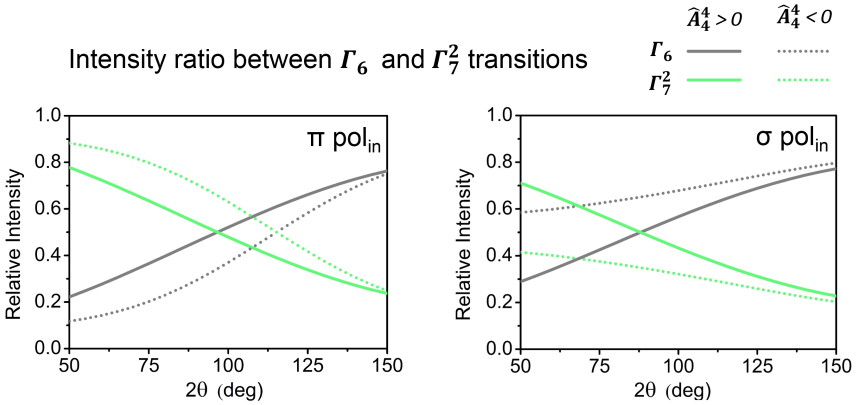

Figure 4.16: Relative intensities of the Γ_6 and Γ_7^2 peaks (calculated as $\Gamma_6/(\Gamma_6+\Gamma_7^2)$ and $\Gamma_7^2/(\Gamma_6+\Gamma_7^2)$) resulting from simulations at various scattering angles (in specular geometry, $\delta = 0°$). The two possible signs of $\check{A}_4^4$ give different dependencies on 2θ, but converge at 150°, allowing, at this angle, to neglect the $\check{A}_4^4$ sign and simplify the analysis.

range, while there is a slight increase of their average energy, due to lowering of the ground state's energy. Anyway, the maximum combined shift induced by the magnetism is small and not easily detectable by our measurements. Therefore the only effect observable in RIXS spectra would be the excitation in the Δ_{gs} split state. Yet its detection is impossible for the moment, being limited by the experimental resolution and by the uncertainties affecting the quasi-elastic region. Moreover, the calculated intensity of this magnetic feature is rapidly decreasing if compared to that of the adjacent elastic peak (bottom left panel of Figure 4.15). Therefore, if present, the Δ_{gs} excitation would be hidden in the tails of the elastic peak, and would be very difficult to detect. Regarding the transitions in the higher CEF levels, only the lowest of the two Γ_6 split states and the highest of the Γ_7^2 give non negligible intensities in the considered scattering conditions ($2\theta = 150°$, $\delta = 15°$ and σ polarisation, as those of Figure 4.14). As shown in the bottom right panel of Figure 4.15, both peaks should decrease with increasing magnetic interaction, but the ratio between the two is constant with Δ_{gs}. This further confirms what is observed in the experimental data: the shape of the inelastic part of the spectrum is not modified by the arising of the magnetic ordering and no magnetism-related effects are detectable in spectra.

4.5 Choice of scattering geometry and incident photon energy

To determine the CEF scheme from the spectra, the choice of the experimental parameters is particularly important. The relative intensity of the CEF peaks depends indeed on the

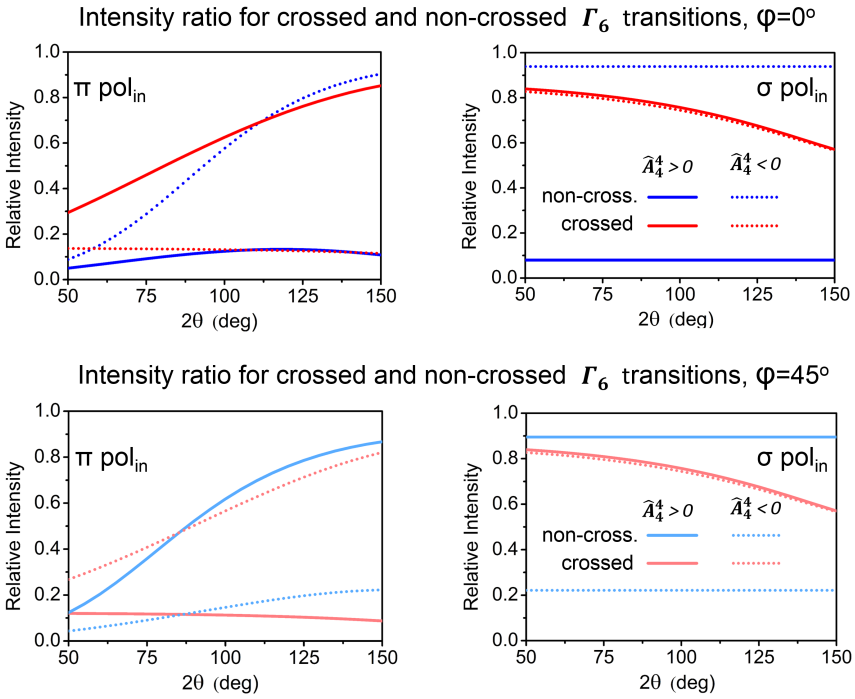

Figure 4.17: Calculated intensity ratios $\Gamma_6/(\Gamma_6+\Gamma_7^2)$ for the crossed and non-crossed polarisation channels at various scattering angles (and specular geometry). The two possible signs of $\check{A}_4^4$ give different Γ_6 ratios for the crossed and non-crossed spectra (which translate in different spectral shapes), allowing to determine the $\check{A}_4^4$ sign with a polarisation analysis. The difference is maximum at $2\theta = 150°$.

scattering angle and on energy and polarisation of the incident beam. Figure 4.16 shows the intensity ratios for the transitions from the Γ_7^1 into the Γ_6 and Γ_7^2 levels calculated for the found CEF parameters as a function of the scattering angle 2θ in the full range of the ERIXS spectrometer (50°-150°) and keeping the condition of specular geometry $\delta = 0°$. As a general trend, the Γ_7^2 relative intensity decreases, and the Γ_6 contribution increases, by increasing the scattering angle. The scattering geometry can therefore be used to enhance the signal of a specific excitation. For example, at 150° the higher intensity of the Γ_6 peak allowed to easily locate it on the tail of the elastic peak. Most importantly, at 150° the peaks' intensity ratio is the same for $\check{A}_4^4 > 0$ and $\check{A}_4^4 < 0$, if the two crossed and non-crossed polarisation channels are not separated. This allows to neglect the $\check{A}_4^4$ sign in the determination of the CEF levels' symmetry and energy, therefore restricting the possible variables and simplifying the analysis.

On the other hand, the two possible signs of $\check{A}_4^4$ give clearly different spectra if the channels for crossed- and non-crossed polarisations are studied individually. This is shown in Figure 4.17, which reports the calculated ratio $\Gamma_6/(\Gamma_6+\Gamma_7^2)$ for the two polarisation

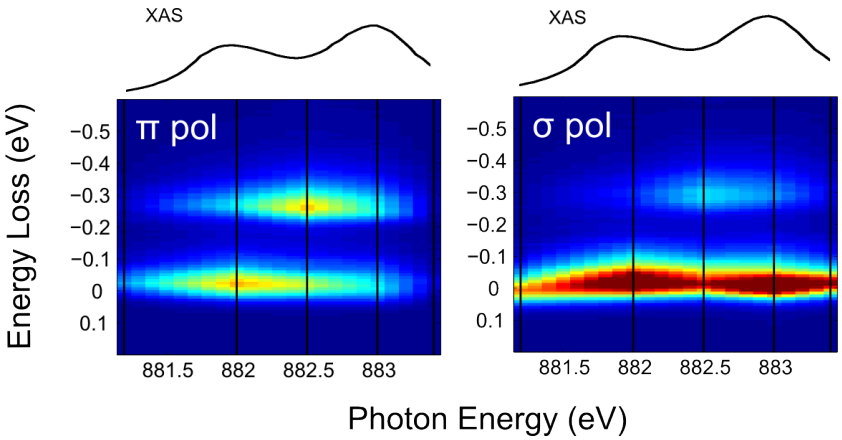

Figure 4.18: M_5 RIXS maps for $CeCu_2Si_2$ with π and σ polarisations of the incident photons and corresponding XAS spectra. The resonant energies for the excitations in the $^2F_{5/2}$ and $^2F_{7/2}$ multiplets, about 882 and 882.5 eV respectively, are visible in the map acquired with π polarisation, while the σ polarisation spectra are more affected by the strong elastic peak, which follows the XAS signal.

channels and for the two signs of $\check{A}_4^4$. Starting from the top panels ($\varphi = 0°$), if $\check{A}_4^4 > 0$ the Γ_6 relative intensity is higher in the crossed channels (red solid lines) and lower in the non-crossed ones (blue solid lines), while the intensity ratio is inverted if $\check{A}_4^4 < 0$ (dotted lines). The difference between the two situations reaches its maximum at 150°, making this angle the most suitable also for the determination of the $\check{A}_4^4$ sign, by using the ERIXS polarimeter. The bottom panel shows the same plots for $\varphi = 45°$, which presents an exactly opposite description, with the crossed- and non-crossed channel swapped. It is also worth to notice that towards $2\theta = 150°$, the intensity ratios for π an σ incident photons' polarisation become similar, consistently with the proximity of this angle to the backscattering condition (180°) at which the two polarisations would be equivalent for our sample orientation. The incident photon energy has almost no effect on the intensity ratio between the Γ_6 and Γ_7^2 transitions. On the other hand, the relative intensity of the excitations in the $^2F_{5/2}$ and $^2F_{7/2}$ multiplets is strongly dependent on E_{in}. The existence of a trend was already suggested by the low-resolution data, as visible in Figure 2.4, and then confirmed by the high-resolution spectra in Figure 4.3. To further investigate the observed effects, RIXS maps of $CeCu_2Si_2$ are shown in Figure 4.18. The spectra were acquired at $2\theta = 90°$, angle at which the elastic intensity is strongly reduced in the π polarisation channel. This allows to easily identify on the corresponding map (left panel) the $^2F_{5/2}$ resonance energy, located approximately in correspondence of the first M_5 XAS peak. The RIXS map built from σ polarised spectra (right) is in fact dominated by the elastic intensity, which follows the shape of the XAS spectrum and, being more intense, covers the $^2F_{5/2}$ resonance. On the other hand,

the excitation in the ${}^2F_{7/2}$ multiplet (at around 300 meV E_{loss}) is enhanced with incident energies halfway between the two main M_5 XAS peaks. Interestingly, the difference between the ${}^2F_{5/2}$ and ${}^2F_{7/2}$ resonance energies is approximately the energy distance separating the two multiplets ($\sim 300meV$).

Chapter 5

Momentum dependence of the crystal field excitations in $CeRh_2Si_2$

In Kondo systems, the CEF-split $4f$ levels hybridize with the conduction bands, losing their purely atomic-like character. Consequently, the energies of the $4f$ levels can become momentum dependent in the region of the reciprocal space where the they are crossed by the itinerant bands. Dispersion of $4f$ energy levels have been observed by angle resolved photoemission spectrocopy (ARPES) in several heavy fermion compounds, based both on cerium, such as $CeIrIn_5$ [142], and other rare-earths, as $YbRh_2Si_2$, $YbIr_2Si_2$ and $EuRh_2Si_2$ [143] [144] [145] [81]. In $CeRh_2Si_2$, angle resolved resonant PES revealed a curvature of the CEF levels (Figure 1.11) near $k_{x,y} = 0$ rlu , induced by the approaching hole-like Rh $4d-$derived band [88].

As a consequence, each CEF level is no longer characterised by one single energy E_{CEF} across the entire Brillouin zone, but forms a heavy band in a narrow energy range around E_{CEF} in part of the BZ. This deviation from the CEF model, and its effects on the spectra, should be considered for a correct description of the splittings. In RIXS, as well as INS, the $4f-$dispersion causes a broadening or, more generally, a shape modification of the peaks as well as an apparent shift of the RIXS (and INS) peaks' position in the spectra. The main difference between RIXS-INS and PES lies in the method employed for the determination of the CEF splitting. PES extracts electrons from the $4f$ states and measures their energy and momentum: by applying the conservation laws, it can retrieve information on the energy E and momentum $\boldsymbol{k}$ of each electron before the interaction and hence determine the dispersion relation $E(\boldsymbol{k})$ of the CEF levels. This also holds for resonant photoemission

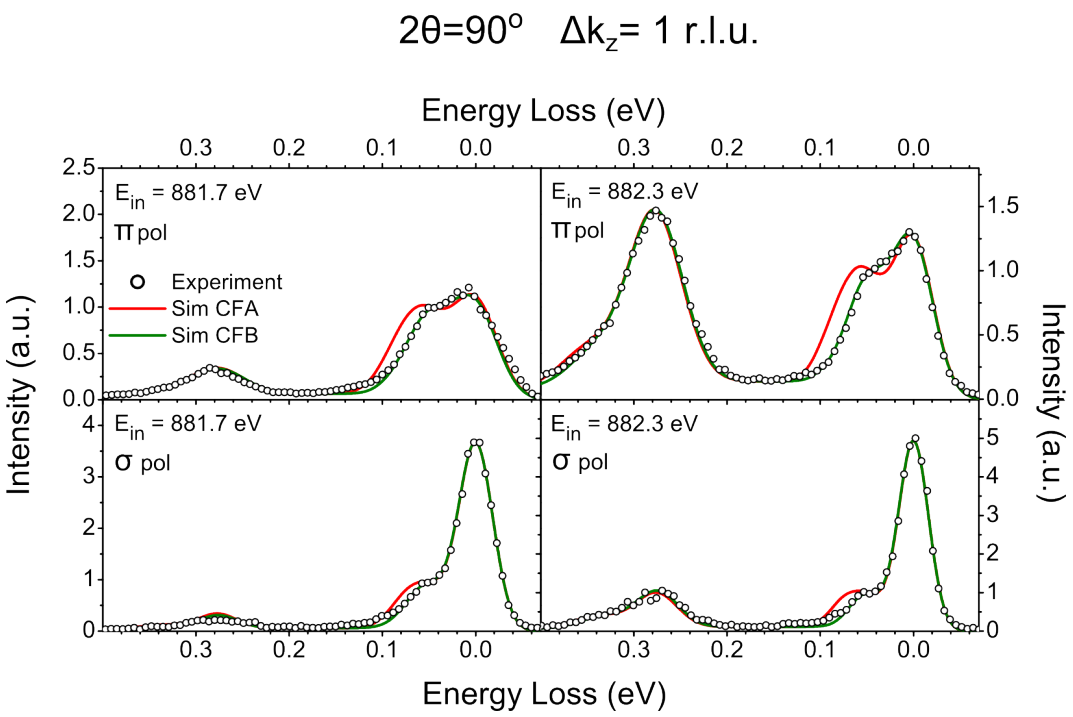

Figure 5.1: High-resolution ($\sim$ 35 meV) RIXS spectra at $2\theta = 90°$, specular geometry. The 46-73 meV splitting scheme (CFA), obtained by analyzing $2\theta = 150°$ data, doesn't fit the experimental data, while there they are accurately reproduced by using new values for the splittings, 43-63 meV (CFB), in simulations.

[146, 147]. RIXS and INS, instead, measure the energy and momentum transfer required for an electronic transition *between two* $4f$ *levels*. The shape and energy of the spectral features are therefore affected by the dispersion $E(\mathbf{k})$ of both levels, whose contributions are complexly entangled. Moreover, only the transferred momentum $\Delta\boldsymbol{k}$, fixed by the scattering geometry, is known, while the electrons' momenta in the initial and final states are undefined. Note that this is only when studying electronic transitions. The energy and momentum of magnons and phonons is well defined by the energy and momentum transferred to the sample in the excitation process that creates them. The present chapter investigates the effects of the CEF levels' dispersion in RIXS spectroscopy and the possible errors induced in the determination of the CEF. The first section introduces the problem by showing a dependence of the observed CEF peaks' positions on the scattering angle. In fact, the effects of the dispersion affecting the RIXS features vary with the transferred momentum $\Delta\boldsymbol{k}$, i.e. with the scattering geometry. This will be explained in the second section, where a simple model for the interpretation of the peaks' shifts will be introduced. The comparison between data and models with different states' dispersions can even, for simple situations, provide a qualitative description of the levels' $\boldsymbol{k}-$dependence, thus giving a more accurate description

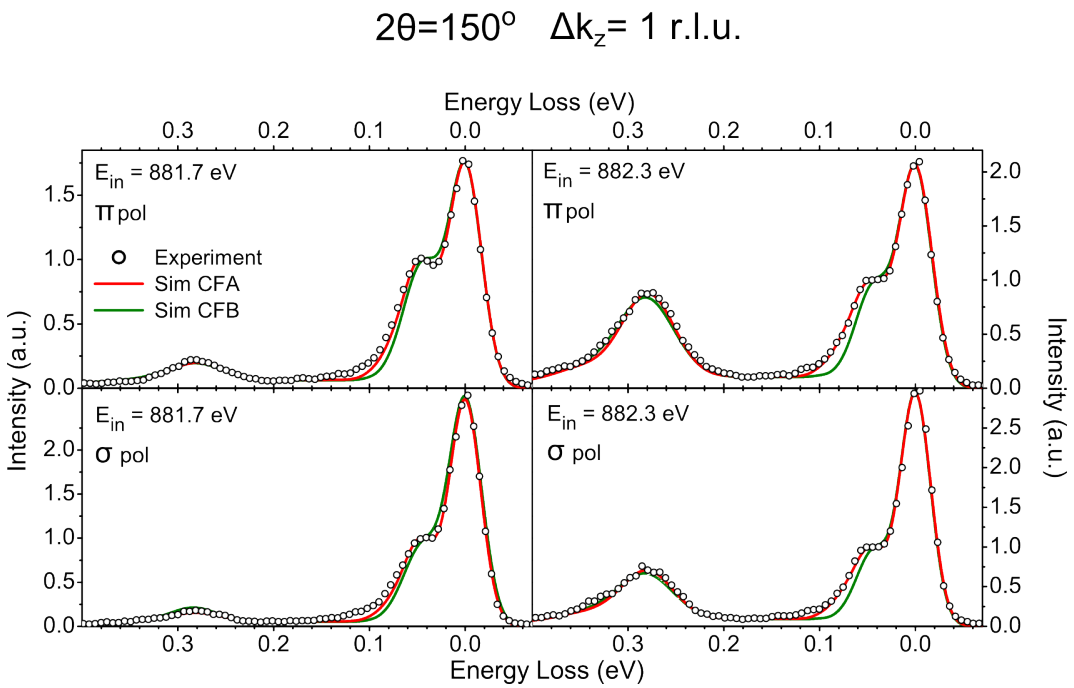

Figure 5.2: Comparison of the CFA and CFB splitting schemes with high-resolution data at 150° scattering angle, $\delta = 0°$. The fits confirm that the CFA scheme is the most accurate for data acquired in this geometry.

of the splittings. In the last section the CEF splittings obtained from RIXS spectra with various momentum transfers will be presented, confirming the qualitative agreement with the presented model.

5.1 Angular dependence of the CEF excitation energies

In the previous chapter, the analysis of $CeRh_2Si_2$ RIXS spectra gave an order $\Gamma_7^1 - \Gamma_6 - \Gamma_7^2$ of the $^2F_{5/2}$ CEF levels, with 46-73 meV splittings. The set of CEF parameters best reproducing the experimental data was $\check{A}_2^0 = 60$ meV, $\check{A}_4^0 = -76$ meV and $\check{A}_4^4 = 194$ meV, hereinafter referred to as CFA. The scattering geometry employed, ($2\theta = 150°$, $\delta = 0°$ and $\chi = 0°$) corresponds to a momentum transfer of about 1.4 rlu, parallel to k_z. The transition therefore occurs between states of neighboring Brillouin zones, which, once folded in the same zone, lie 0.4 rlu apart along $\boldsymbol{k}_z$, i.e. almost half the Brillouin zone size.

To investigate the effects of the CEF levels dispersion, the same set of data (π and σ polarisation, $E_{in} = 881.7, 882.3$ eV) was acquired at $2\theta = 90°$, corresponding to $\Delta\boldsymbol{k} \approx 1$ r.l.u. $\boldsymbol{k}_z$. Once the initial and final states are folded in the same Brillouin zone, they lie approximately in the same position, opposite to the case above, where the initial and final states were separated by approximately the maximum distance along $\boldsymbol{k}_z$.

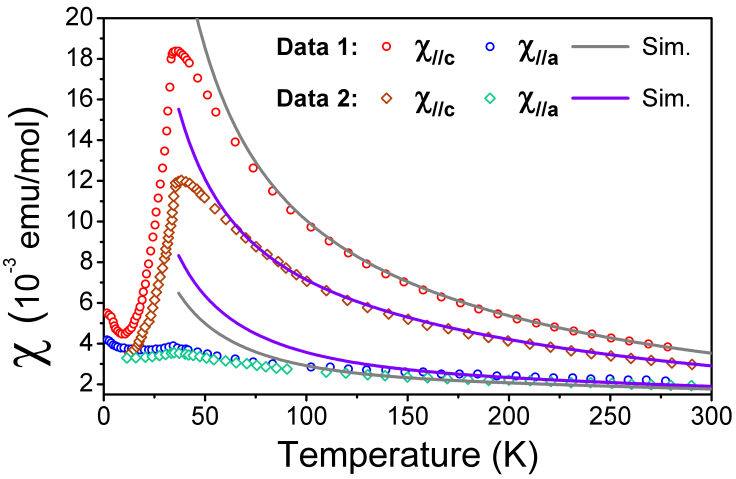

Figure 5.3: Fit of the temperature dependence of the magnetic susceptibility and simulations with the new CEF splittings (43-63 meV). Data 1 are from Refs. [139] and Data 2 from[70].

As shown in Figure 5.1, a new CEF description, with 43-63 meV splittings (CFB), is needed to reproduce the $2\theta = 90°$ data with simulations. The previous 46-73 meV splitting (CFA) scheme would give very different spectra. On the other hand, the comparison of $2\theta = 150°$ data with these two CEF schemes confirms that CFA better reproduces the experimental spectra at this angle. Therefore, the scattering geometry affects the estimate of the CEF splittings from RIXS data. This is due to the angular dependence of $\Delta\boldsymbol{k}$, which determines how the initial and final states' dispersions combine to shape (and shift) the peaks in the RIXS spectrum. The influence of the levels' dispersion on the CEF splitting determination will be discussed in the next section, together with a simple model to interpret the observed shifts of the peaks.

It is interesting to notice that the magnetic susceptibility curves are equally fitted by simulations with both CFA and CFB, provided that a suitable value of $\check{A}_2^0$, which gives the right J_z (or α^2), is chosen. Figure 5.3 presents calculated curves for CFB, with $\check{A}_2^0 = 56$ meV ($J_z = 1.41\ \mu_B$) and $\check{A}_2^0 = 71$ meV ($J_z = 1.76\ \mu_B$), respectively fitting the experimental data from Refs. [70] and [139]. An identical fit was obtained using CFA in Figure 4.8, despite the relevant differences in the values of the splittings between the two CEF schemes.

5.2 Interpretation of the observed Δk dependence

High resolution RIXS is normally employed to map the dispersion of collective excitations as phonons or magnons and $E(\boldsymbol{k})$ is readily obtained by the angular dependence of the peak positions. In fact, these quasiparticles, not present before the interaction, are created with a defined energy $E = E_{\text{loss}}$ and momentum $\boldsymbol{k} = \Delta\boldsymbol{k}$ by the RIXS process.

On the other hand, ff excitations occur between two dispersing states, $E_i(\boldsymbol{k}_i)$ and $E_f(\boldsymbol{k}_f)$. The condition on the momentum conservation defines a value for $\Delta\boldsymbol{k} = \boldsymbol{k}_f - \boldsymbol{k}_i$, but not $\boldsymbol{k}_i$ or $\boldsymbol{k}_f$ individually. As a consequence, transitions in any point of the $4f$ levels' dispersions simultaneously contribute to the same RIXS feature. A peak in the spectrum corresponds to the energy required for a given excitation $E_{\text{loss}} = E_{\text{excit.}} = E_f - E_i$ and, in case of dispersing levels, transitions occurring in different points of the reciprocal space will be characterized by different energies $E_f(\boldsymbol{k}_f) - E_i(\boldsymbol{k}_i) = E_f(\boldsymbol{k}_i + \Delta\boldsymbol{k}) - E_i(\boldsymbol{k}_i)$. Therefore, an ff excitation will not give a single peak at ΔE_{CEF}, but an intensity distribution proportional to:

$$I_{\Delta\boldsymbol{k}}(E_{\text{loss}}) = \int \sigma(E_f(\boldsymbol{k} + \Delta\boldsymbol{k}) - E_i(\boldsymbol{k}))d\boldsymbol{k} \ , \tag{5.1}$$

where the cross section σ can depend on $\boldsymbol{k}$. Under the assumption of constant cross section, the shape of a CEF feature is given by the energy difference, integrated over the reciprocal space, between the dispersions of the two levels "staggered" by $\Delta\boldsymbol{k}$. For strongly asymmetric shapes of $I_{\Delta\boldsymbol{k}}(E_{\text{loss}})$, the measured peak's position can deviate substantially from the splitting ΔE_{CEF}, that would be observable in absence of hybridization and dispersion.

By changing $\Delta\boldsymbol{k}$, the staggering between the two dispersions changes, modifying the feature's intensity distribution and, potentially, the peak's position in the spectrum. This is the origin of the shifts observed between experimental data at $2\theta = 150°$ and $90°$. The dependence of the observed peak's energy on $\Delta\boldsymbol{k}$ is strictly related to the shape of the dispersions, therefore, by comparing the experimental shifts with $E_i(\boldsymbol{k})$ and $E_f(\boldsymbol{k})$ from ARPES measurements and band structure calculations, it is in principle possible to retrieve a qualitative description of the level's $\boldsymbol{k}-$dependence.

An intuitive representation of the discussed effects is depicted in Figures 5.4 and 5.5, which provide a simple model for the interpretation of the angular dependence of $CeRh_2Si_2$ spectra. The ${}^2F_{5/2}$ levels deviate from the flat dispersionless behavior near the zone boundaries, where, according to bandstructure calculations [121] (and similar observation in the parent compound $EuRh_2Si_2$ [81]) the $4f$ levels are crossed by Rh $4d-$derived bands. In the

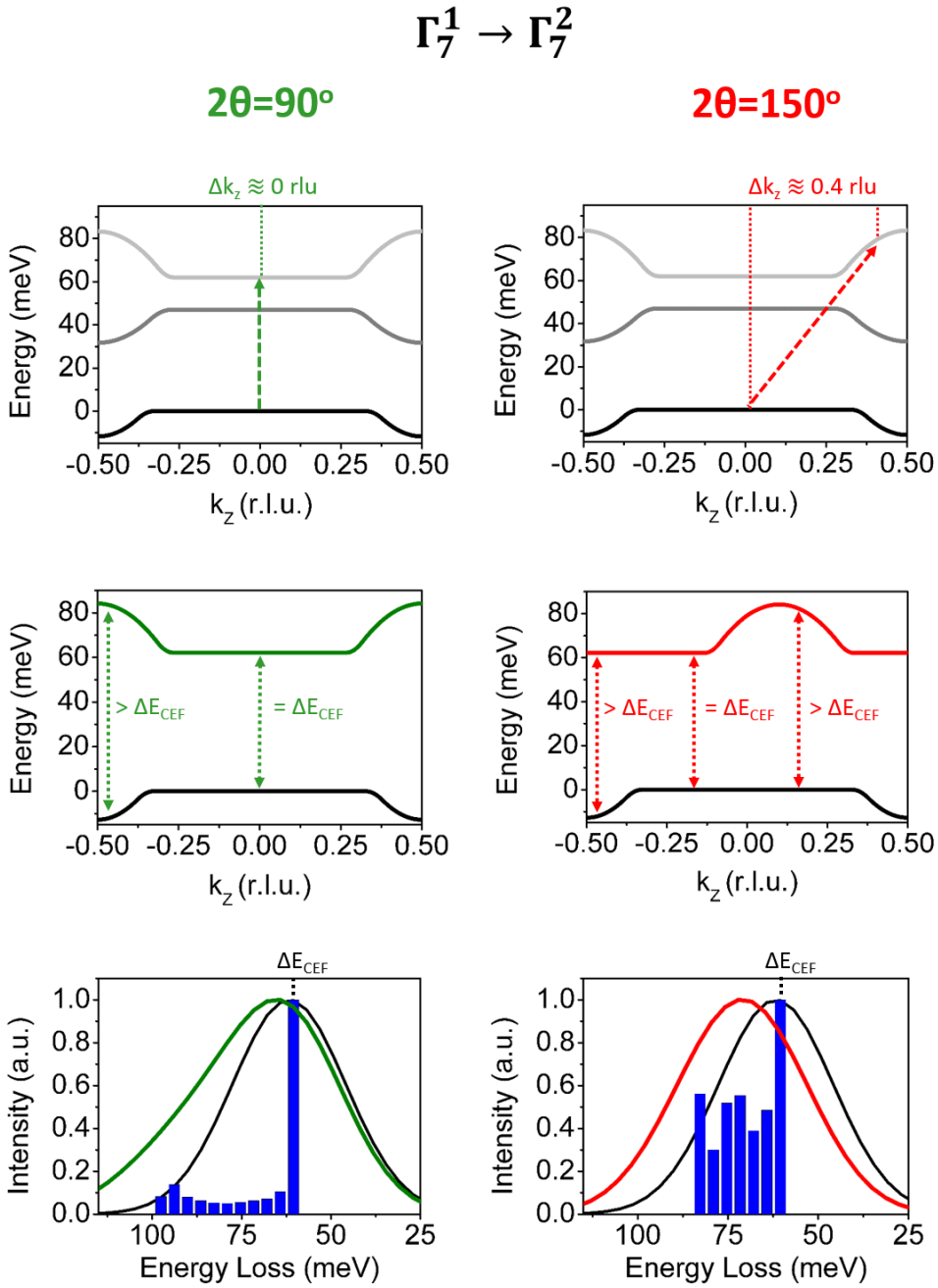

Figure 5.4: Simple model for the intepretation of the angular dependence observed for the $\Gamma_7^1 \rightarrow \Gamma_7^2$ excitation. Top row: A guess for the levels' dispersions along $\boldsymbol{k}_z$ and the Δk_z for the RIXS processes at the two angles. Middle row: The top band is shifted according to Δk_z, in order to allow an easy representation of the various possible transition energies. Bottom row: The histogram (blue) of the transition energies and its convolution with the experimental resolution (green and red lines), which gives the shape of the RIXS feature on the spectra. The RIXS peaks are considerably shifted in energy compared to the ΔE_{CEF} position observable in absence of dispersion.

ARPES data in Figure 1.11 both Γ_7^1 and Γ_6 display a hole-like dispersion while Γ_7^2 shows opposite, electron-like behaviour [88] .

As discussed above, at $2\theta = 90^\circ$ the transition occurs between two equivalent points in the $\boldsymbol{k}-$space ($\Delta\mathbf{k} = (0\,0\,1)$ rlu). At $2\theta = 150^\circ$, instead, the initial and final states are 0.4 rlu apart along $\boldsymbol{k}_z$. Following Equation 5.1, the ($\boldsymbol{k}-$dependent) excitation energy is calculated as the distance between the ground level and the excited one shifted by $\Delta\boldsymbol{k}$. This relative $\Delta\boldsymbol{k}_z$ band shift is depicted in the middle rows of Figures 5.4 and 5.5, to visualize the excitation energies in different points of the reciprocal space for the two scattering geometries. The shape of a RIXS feature in the spectrum will be given by the distribution in energy of all the possible transitions with fixed $\Delta\boldsymbol{k}$ between the two levels (blue bars in the bottom rows of Figures 5.4 and 5.5). At 90° the excitation in the Γ_7^2 level (Figure 5.4) occurs mostly between flat portions of both the initial and final levels, giving a strong peak at the CEF splitting energy ΔE_{CEF}. The transitions between the dispersing regions give only a minor contribution and produce a small tail towards higher energies. After the convolution with the experimental resolution (green line), the position of the peak is only slightly shifted ($\sim 1-2$ meV) towards higher energies compared to its theoretical value ΔE_{CEF} in absence of dispersion (black line).

The effect of the levels' dispersion is much more relevant at 150°, because, due to the relative shift of 0.4 rlu of the two bands, larger portions of the Brillouin zone contribute with transitions of energy $E > \Delta E_{CEF}$. As a result, the observed peak's energy is about 11 meV larger than the value of the CEF splitting. Compared to the presented experimental splitting estimates (63 meV at 90° and 73 meV at 150°), this model reproduces the measured $\sim$ 10 meV variation between the two scattering angles and suggests a value of about 62 meV for the Γ_7^1-Γ_7^2 splitting for those regions of the BZ where the CEF levels do not show dispersion.

The Γ_6 peak undergoes much smaller shifts, because both Γ_7^1 and Γ_6 show a very similar dispersion at the Z point, keeping the distribution of the transition energies always close to ΔE_{CEF}. If the shapes of the two dispersions were exactly the same, no shift of the peaks would be observed, and the measured splitting would coincide with ΔE_{CEF}. To reproduce the observed shifts (43 meV at 90° and 46 meV at 150°) a stronger dispersion must be assigned to the Γ_6 state. This moves the RIXS peak towards lower energies in the 90° spectra, due to the arising of transitions with $E < \Delta E_{CEF}$, while at 150° the shift gets lost in the broader linewidth, caused by transitions energies both larger and smaller than ΔE_{CEF}. A splitting $\Delta E_{\mathrm{CEF}} = 47$ meV was imposed between the flat regions of the two dispersions, in order to get peaks' positions consistent with the experiments.

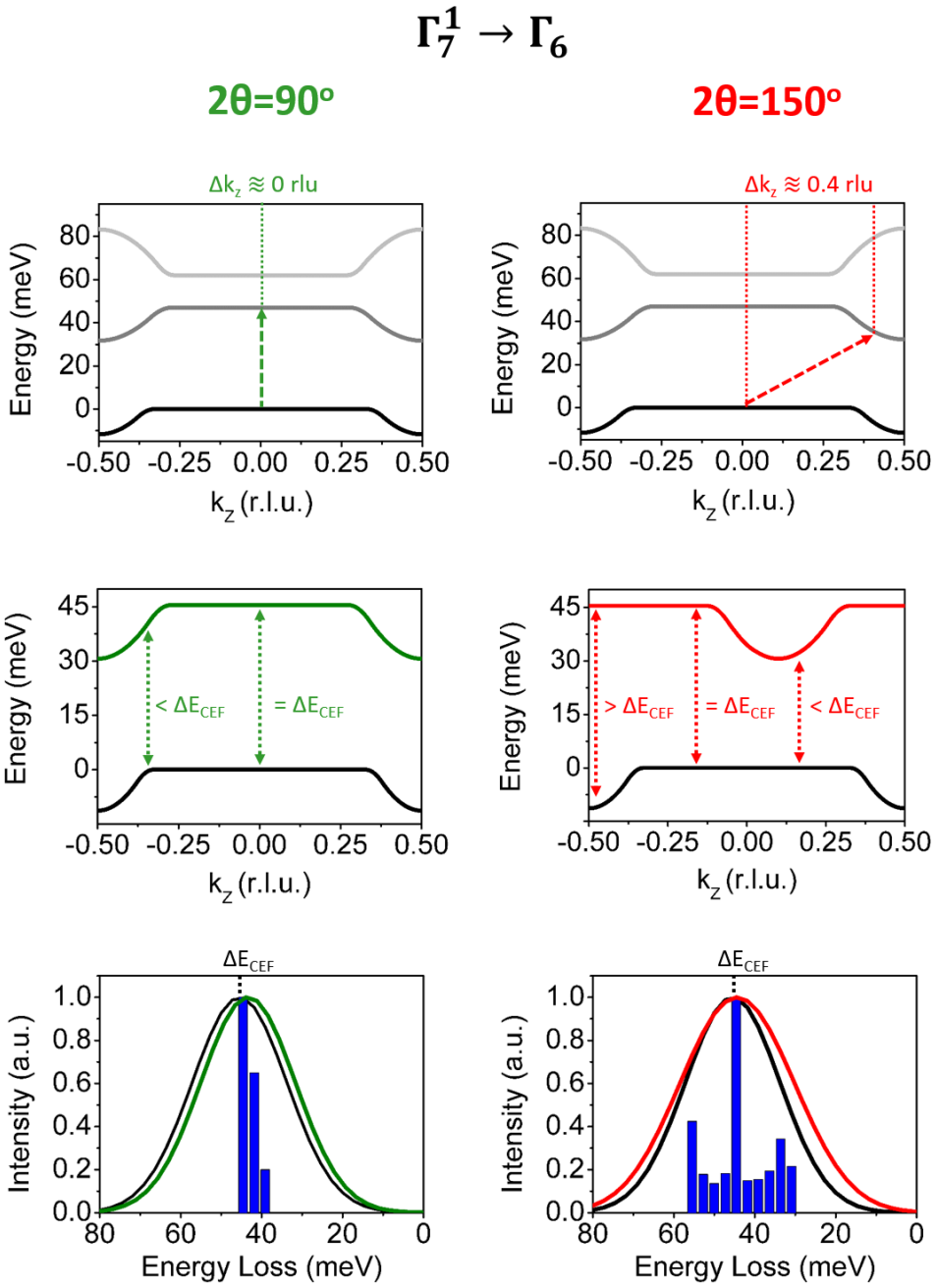

Figure 5.5: Simplified model for the intepretation of the angular dependence of the $\Gamma_7^1 \rightarrow \Gamma_6$ excitation. Top row: A guess for the levels' dispersions along $\boldsymbol{k}_z$ and the Δk_z of the two angles. Middle row: The top band is shifted according to Δk_z, to easily represent the transition energies. Bottom row: The histogram (blue) of the possible energies and its convolution with the experimental resolution (green and red lines), which gives the shape of the RIXS feature on the spectra. Due to the similar dispersions of the two levels, the energy distribution is less asymmetric and the peaks are closer to ΔE_{CEF}. A ~ -3 meV shift is anyway visible in the 90° case, where the deviation from the ΔE_{CEF} transition energy occurs only towards lower energies.

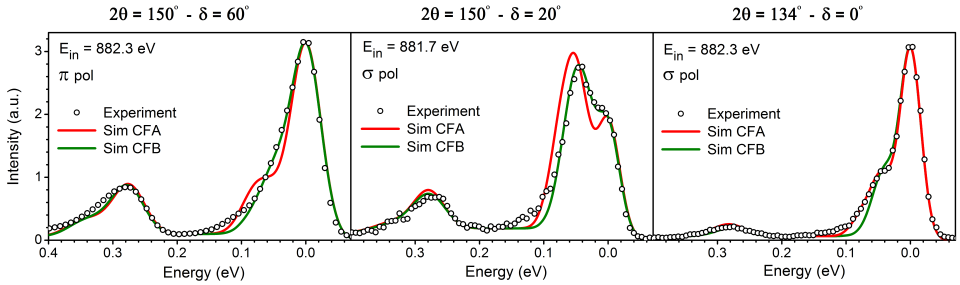

Figure 5.6: High resolution RIXS spectra acquired in various angles and fits using the CFA and CFB schemes. The CEF best reproducing the data varies with the scattering geometry. It is anyway possible, with the present resolution, to fit the data with one of the two schemes found above.

Surprisingly, the estimated 47-62 meV scheme perfectly agrees with the splittings measured between the non-dispersing portions of RPES data [88], suggesting that the dispersion effects should always be considered in order to correctly compare the results of different techniques. The simple model presented already provides an intuitive interpretation of the observed angular dependence of the peaks and a tool for a qualitative analysis.

5.3 Mapping the reciprocal space

Folded back into the first Brillouin zone, the momentum transferred in the two scattering geometries correspond to positions close to the Γ point ($\Delta\boldsymbol{k}^{2\theta=90^\circ,\delta=0^\circ}$) and the Z point ($\Delta\boldsymbol{k}^{2\theta=150^\circ,\delta=0^\circ}$), i.e. the zone center and the zone boundary along $\boldsymbol{k}_z$. To further investigate the $\Delta\boldsymbol{k}-$dependence of the RIXS peaks, we acquired high-resolution spectra at various angles (Figure 5.6) and compared them with spectra calculated for the two CEF schemes CFA (46-73 meV) and CFB (43-63 meV) obtained at $2\theta = 150^\circ$ ($\approx Z$ point) and $2\theta = 90^\circ$ (Γ point), respectively. Contrary to those acquired in specular geometry, the new spectra at $2\theta = 150^\circ$, with $\delta = 20^\circ$ and 60° off-specular, are in better agreement with the CFB splitting scheme. Their transferred momenta, both with $\Delta k_z \approxeq 0.3$ rlu and, respectively, $\Delta k_x \approx 0.2$ rlu and $\Delta k_x \approx 0.5$ rlu ($\Delta k_y = 0$) move away from the Z point. On the other hand, the spectrum acquired in specular geometry at $2\theta = 134^\circ$, with a transferred momentum closer to the Z point, is reproduced by calculations with CFA splittings. It seems therefore that the CFA scheme only suits spectra whose momentum transfers lie within a region around the Z point, while other spectra are better reproduced by CFB.

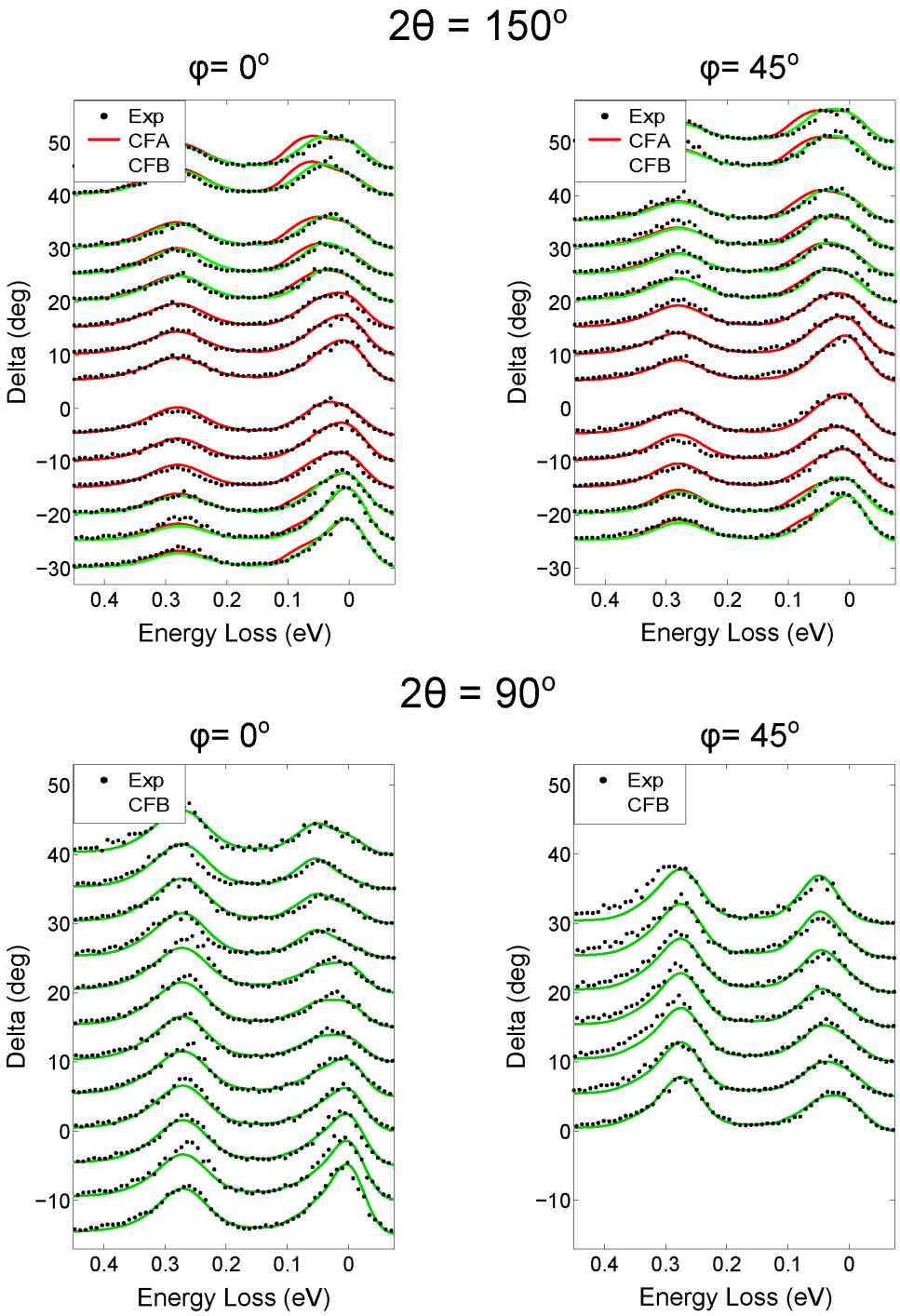

Figure 5.7: 60-meV resolution RIXS spectra at various δ for both $2\theta = 150°$ and 90°, and $\varphi = 0°$ and 45°. The CFA scheme fits the data at 150° around $\delta = 0°$, while at large positive and negative values of δ the experimental spectra are reproduced more accurately by calculations with CFB. At 90°, instead, the CFB scheme provides a good agreement for every δ.

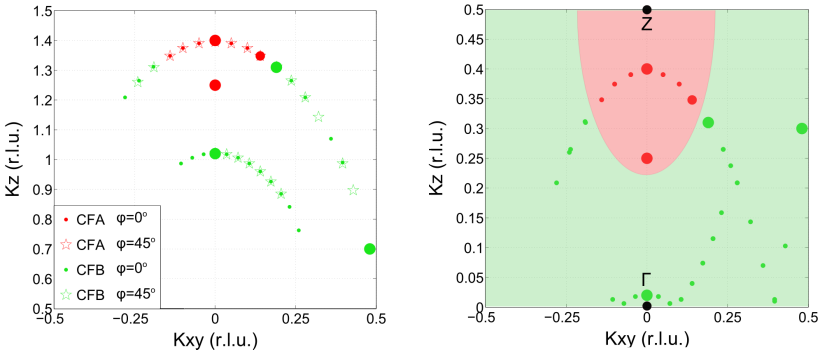

Figure 5.8: Left: Map on the reciprocal space of the transferred momenta of all the scattering geometries tested, indicating the CEF scheme better fitting each spectrum. The larger dots represent the high resolution data (shown in Figures 5.1, 5.2, 5.6 and 4.14). Right: Folding the points in the same half of the Brillouin zone, it can be noticed that the CFA scheme fits only spectra with $\Delta\boldsymbol{k}$ around the Z point.

The two CEF schemes were sufficient to fit the RIXS spectra acquired in various scattering geometries, within the experimental uncertainties. In general, the shift of the RIXS features induced by the level's dispersion should vary gradually and continuosly with $\Delta\boldsymbol{k}$, resulting in slightly different splittings at each angle.

To map the reciprocal space in more points, we acquired 60 meV-resolution spectra (Figure 5.7) varying δ in steps of 5°, for both $2\theta = 150°$ and 90°, and $\phi = 0°$ ($\Delta k_{xy} = \Delta k_x$, $\Delta k_y = 0$) and 45° ($\Delta k_x = \Delta k_y = \Delta k_{xy}/\sqrt{2}$). The CFA scheme correctly reproduces the spectra at 150° scattering angle for small values of δ, while at about $\delta = \pm 20°$ the calculations start to deviate from the experimental data. At larger δ, instead, the the spectra are better reproduced using the CFB scheme. On the other hand, 90° data are all in agreement, within the experimental uncertainties, with the CFB scheme. No difference is observed between the two orientations of the sample $\varphi = 0°$ and 45°. All these findings enforce the conclusions above that the CFA scheme describes the experimental observations in a restricted region around Z (approximately 150°, $\delta = 0°$), while CFB fits the data everywhere else. Due to the noise and the lowered energy resolution, it was not possible to investigate the transition between the CFA and CFB schemes, or to try fitting the spectra at new angles using other splittings. By plotting in the reciprocal space the transferred momenta (Δk_z, Δk_{xy}) of all the $CeRh_2Si_2$ spectra presented, one obtains the maps in Figure 5.8, where the colors of the dots indicate which CEF scheme better fits the data. After folding the points in their equivalent positions within the first Brillouin zone, the special character of spectra with $\Delta\boldsymbol{k}$ near the Z becomes evident. A more complete model than the one presented above might be needed to fully understand the details of this $\Delta\boldsymbol{k}$

dependence of the CEF peaks in RIXS. Nonetheless, this first observation of an angular dependence of ff excitations is crucial to better interpret the results of RIXS and INS. With a detailed theoretical analysis of these effects, it could be possible to completely determine the three-dimensional dispersion of $4f$ levels from the angular dependence of the $4f$ features.

Chapter 6

Crystal field excitations in other Ce 122 compounds

In the previous chapters, the ability of RIXS of probing the $4f$ levels in cerium intermetallics was discussed using the example of $CeRh_2Si_2$. In that case, the splittings were comparable to the experimental resolution. It is useful at this point to investigate the limits of applicability of RIXS spectroscopy to study the $4f$ states' properties within the CEF model. To this end, two opposite cases will be considered in this chapter. In $CeCu_2Si_2$ the CEF splittings are smaller than our energy resolution and it will be shown that it is nonetheless possible to obtain information on the CEF by exploiting the polarisation and angular dependence of the cross sections. At the other end, $CeCo_2Ge_2$ presents extremely large splittings and all the ff excitations are clearly resolved in the spectra, allowing even a detailed analysis of the $^2F_{7/2}$ levels. Yet, for such large effects on the $4f$ levels, the usual CEF approach loses its validity. The Stevens' approximation doesn't hold true anymore and the mixing between the two spin-orbit multiplets can't be neglected. Moreover, and most importantly, the strong interaction of the $4f$ electrons with the surroundings cause a significant broadening of the spectral features and modify the peaks' intensities compared to single-ion calculations which introduces uncertainties in the analysis.

6.1 $CeCu_2Si_2$: crystal field splittings below the experimental resolution

$CeCu_2Si_2$ is the first compound in which heavy fermion superconductivity was discovered [15]. Further studies found two distinct superconducting domes in the phase diagram, one (T_{c1} = 600 mK, P_{c1} = 0.45 GPa) related to a magnetic quantum critical point and the

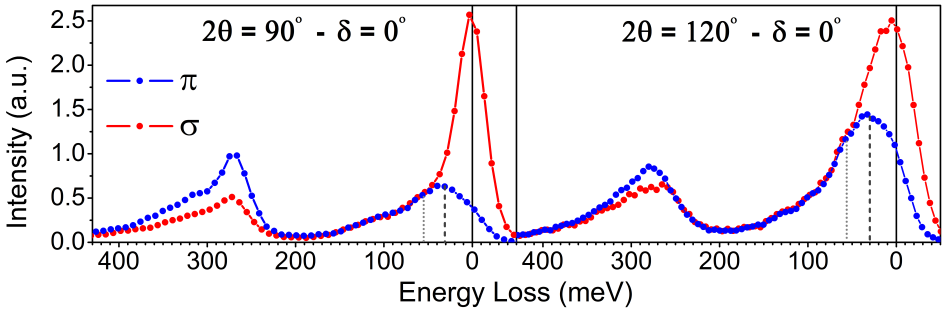

Figure 6.1: RIXs spectra of $CeCu_2Si_2$. Thanks to the reduction of the elastic intensity with π polarisation, a first inelastic peak is visible at 30 meV (dashed line). A shoulder is visible at higher energies (dotted line), in addition to a broad tail up to 170 meV. Spectra have been renormalized to easy the comparison between σ and π polarizations.

other ($T_{c_2} = 2$ K and $P_{c_2} \approx 4$ GPa) to orbital or valence fluctuations [28, 29, 31, 34, 35]. Ce is close to 3+ valence and the sample's magnetic properties at $T > T_K \approx 10$ K describe a system of non-interacting local $4f$ moments. Below this temperature a nonmagnetic state develops and the electrons at the Fermi level acquire huge effective masses. The specific heat discontinuity at T_c is enhanced by a factor of 10^3 if compared to normal superconductors, similar to the normal-state electronic specific-heat coefficient, confirming the participation of the heavy fermions in the superconducting behavior [1, 148, 103].

Boosted by these discoveries, several studies have been addressed to the determination of the CEF splitting scheme in $CeCu_2Si_2$. The first INS investigation [149] assigned two peaks to the lowest CEF levels, with splittings of 12 meV and 30 meV and this result was roughly confirmed by another work on non-stoichiometric $CeCu_{2+x}Si_2$ [150]. Inelastic scattering of polarised neutrons [151, 152] revealed the presence of the peak at 30 meV, but nothing was detected at lower energies. The discrepancy was attributed to to the lower resolution and the higher noise of the polarised spectra. Later, the presence of a crystal-field level at 12 meV was further disproved by specific-heat and INS measurements [153] [103] and the most accepted CEF scheme is now the one proposed in Ref. [103], with two closely spaced excited levels at about 30 meV. Anyway, all these studies could only investigate excitation energies up to approximately 50 meV. Therefore $CeCu_2Si_2$ constitutes an optimal test for the ability of RIXS of studying small CEF splittings and, at the same time, investigate higher energy excitations.

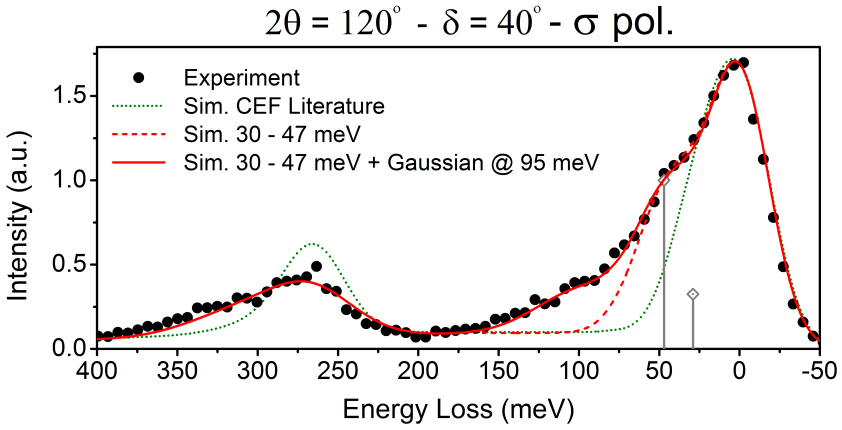

Figure 6.2: Experimental data in a scattering geometry that enhances the cross section for $\Gamma_7^1 \rightarrow \Gamma_7^2$ transition. The shoulder is here more visible, suggesting the presence of a peak at 47 meV. Simulations with a 30-47 meV splitting scheme prodivide a good fit of the data ($\check{A}_2^0 = 40$ meV, $\check{A}_4^0 = -50$ meV and $\check{A}_4^4 = 117$ meV). The quality of the fit further improves by adding a Gaussian at 95 meV. On the other hand, the CEF proposed in Ref. [103] give a very different spectra.

6.1.1 Determination of the crystal electric field splittings

Splittings smaller than the experimental resolution can be detected by exploiting the angular and polarisation dependence of the cross sections. With the present experimental resolution of $\sim$ 35 meV, the CEF peak expected at 30 meV might be hidden by the neighboring (and usually much stronger) elastic peak, which must be strongly reduced to allow for the detection of the ff transitions. A consistent portion of the elastic intensity is due to diffuse scattering and has a $\boldsymbol{\epsilon}_{in} \cdot \boldsymbol{\epsilon}_{out}$ polarisation dependence [92]. This contribution can be minimized by using π polarised photons and detecting the signal at $2\theta = 90°$: in these conditions the polarisation vectors of the outgoing photons are always perpendicular to $\boldsymbol{\epsilon}_{in}$, giving a zero scalar product. The effect is shown in Figure 6.1, where spectra acquired with both σ and π incident polarisation are compared, the latter showing a reduced elastic peak intensity. In these spectra, an inelastic peak arises at 30 meV, (indicated by the dashed line) in agreement with the previous studies.

In addition to this first peak, the spectra show some intensity up to 170 meV. In part, it can be assigned to excitations in the conduction band, similarly to what was discussed before for $CeRh_2Si_2$. Yet, a small shoulder is visible in all spectra on the high-energy side of the first ff excitation (dotted line). This feature may represent another ff excitation at higher energy, not detected by the previous studies due to the limitations on the maximum

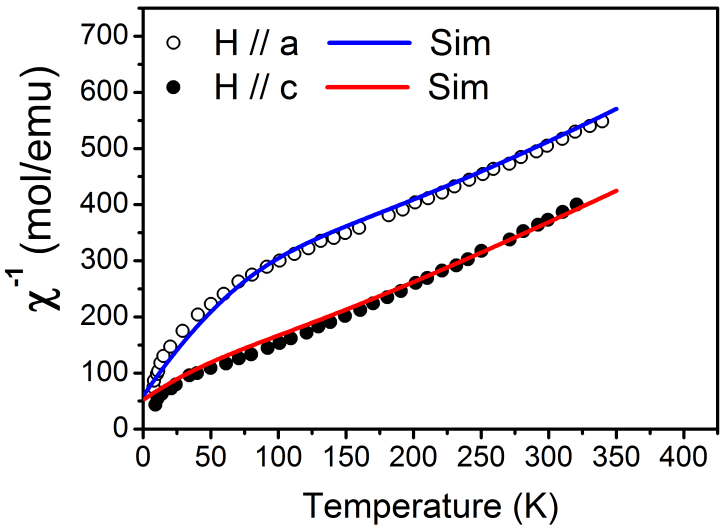

Figure 6.3: Fit of the inverse magnetic susceptibility data from Ref. [154] using the proposed set of CEF parameters.

excitation energy. To verify this hypothesis, we selected experimental conditions that enhance the excitation in the Γ_7^2 state, which was found to be the highest of the three $^2F_5/2$ levels in $CeRh_2Si_2$ (Figure 6.2). The presence of a second feature over 30 meV is clear from the experimental spectrum. By assigning the first peak to the Γ_6 state and the second to the Γ_7^2, the best fit is obtained with 30 - 47 meV splittings and CEF parameters $\check{A}_2^0 = 40$ meV, $\check{A}_4^0 = -50$ meV and $\check{A}_4^4 = 117$ meV. The quality of the fit improves by adding a broad gaussian centered at 95 meV, to account for the extra intensity probably due to CT-like features. On the other hand, the CEF scheme proposed in Ref. [103] can't reproduce correctly the experimental data.

The new set of CEF parameters can also fit the inverse magnetic susceptibility curves $\chi^{-1}(T)$ presented in Ref. [154], which were used in Ref. [103] to test the soundness of the 30 - 30 meV scheme (Figure 6.3). Interestingly, a weak feature at 50 meV has been observed by Raman scattering in Ref. [155] and it was there assigned to a phonon mode of the Silicon ions. Yet, its symmetry and temperature dependencies, as well as its absence at low temperatures on the parent compound $LaCu_2Si_2$, are compatible with a CEF transition.
All the data acquired can be fitted using the proposed scheme, with two separated ff excitations and a broad feature at higher energies (Figure 6.4). Unfortunately the spectra are not well defined, mostly due to a weak second peak, and it is difficult to estimate the accuracy of the simulations. Therefore, despite the intriguing results, the energy resolution

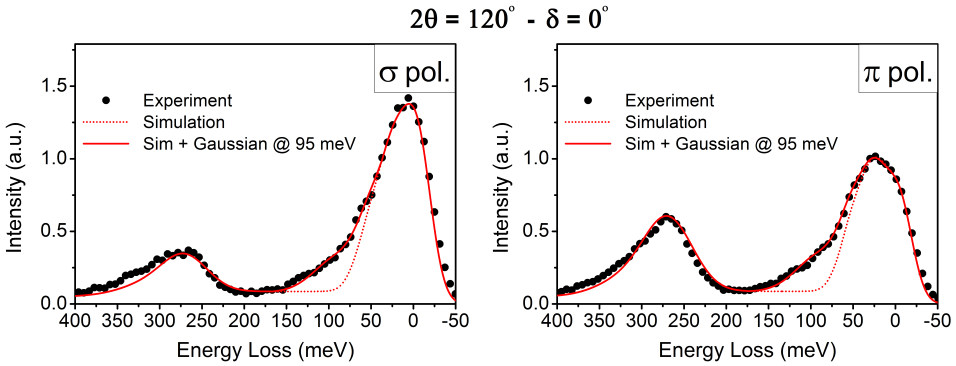

Figure 6.4: $CeCu_2Si_2$ experimental data at $2\theta = 120°$ and $\delta = 0°$, and simulated spectra. The simulations best reproducing the data have a slightly modified scheme, with the second peak positioned at 55 meV instead of 47 meV. The shoulder is anyway weak and the broad feature at 95 meV strongly modifies the shape of the spectra, not allowing for a clear identification of the features.

is still insufficient to investigate more in detail the $CeCu_2Si_2$ CEF splittings and the nature of the observed spectral features. Moreover, the broad and relatively intense peak at 95 meV introduces uncertainty in the data analysis and it should be better identified to provide a more reliable interpretation of the data.

6.1.2 Determination of the wavefunctions' orientation without polarisation analysis

The orientation of the CEF wavefunctions in $CeCu_2Si_2$ was determined by Willers *et al.* with non-resonant X-ray scattering [43], reaching the same conclusions found in section 4.3 for $CeRh_2Si_2$. The investigation of such effects on this sample can serve as an example of the RIXS ability of studying the CEF properties in presence of small splittings.

With such close and overlapping features an analysis of the polarisation of the scattered beam, as the one carried out for $CeRh_2Si_2$, is not possible. The intensity loss ($\sim 90\%$) on the multilayer requires indeed to lower the resolution to ~ 60 meV, in order to recover a reasonable photon flux on the detector. With this resolution, the features would be indistinguishable on the polarised spectra. Anyway, it is possible to find an experimental condition that maximized the dependence of the (non-polarised) cross sections on the property of interest. As shown in Figure 4.16, the intensity ratio between the Γ_6 and Γ_7^2 peaks depends on the scattering angles and on the sign of the $\check{A}_4^4$ parameter, which determines the wavefunctions' orientation. At about 90°, depending on the $\check{A}_4^4$ sign, the two transitions can have

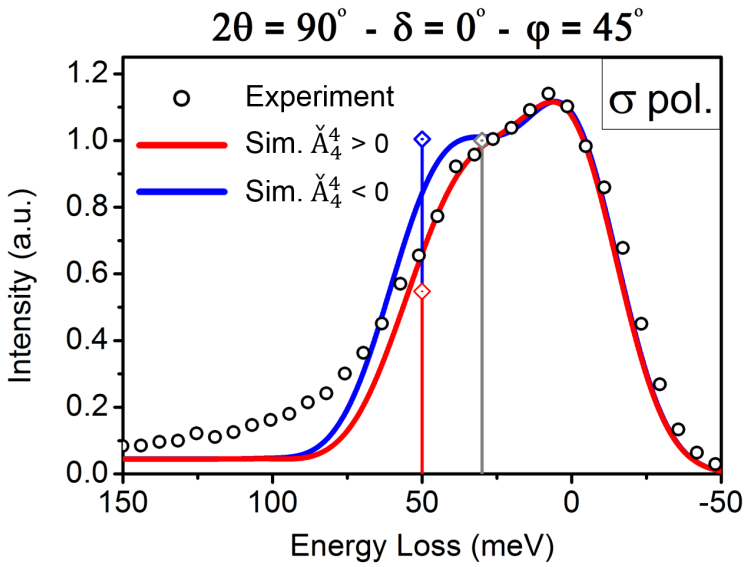

Figure 6.5: The cross section dependence on the $\check{A}_4^4$ sign can be exploited to determine the wavefunciton orientation, without the need of a polarisation analysis. Supposing that the CEF scheme proposed for $CeCu_2Si_2$ is correct, simulations with $\check{A}_4^4 > 0$ are in better agreement with the experimental data, confirming the results of Ref. [43].

similar intensities or Γ_6 is two times more intense than Γ_7^2. Figure 6.5 shows the comparison of experimental data with the two possibilities, confirming the findings that $\check{A}_4^4 > 0$. Note that in these data $\varphi = 45°$ and so the cross section dependence on the $\check{A}_4^4$ sign is inverted if compared to what shown in Figure 4.16.

6.2 $CeCo_2Ge_2$: large splittings and limitations of the crystal field model

$CeCo_2Ge_2$ shows intermediate $4f$ occupation at low temperatures, while at room temperature Ce ions are close to a trivalent state [156, 157, 158]. Anomalies in the magnetic susceptibility and in the resistivity indicate the arising of a strong Kondo state at $T_K \approx 120$ K [157], in agreement with specific-heat measurements [156]. Around this temperature, it has also been observed a large thermal expansion in both the a and c lattice constants. Below 20 K, the quadratic dependence of the resistivity suggests a Fermi-liquid behavior [157].

No experimental study of the $4f$ CEF splittings has been reported. The intermediate valence effects [157] and other non-local contributions to the magnetism [156] make it impossible to deduce the CEF parameters from susceptibility curves and no INS study has

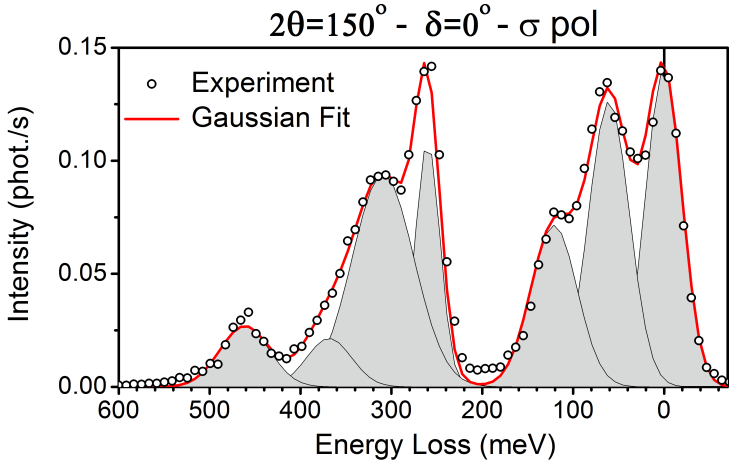

Figure 6.6: $CeCo_2Ge_2$ RIXS spectrum and a fit with 7 Gaussians representing the 7 CEF levels. The peak widths vary between 35 and 65 meV.

been published. Resonant photoemission spectroscopy [159] detected a strongly dispersing state with relevant $4f_{7/2}$ character, confirming the strong f electrons' delocalization at low temperatures, but the resolution was insufficient to resolve the single CEF levels.

The only estimate of the CEF scheme given in literature results from a point-charge model calculation and predicts splittings of 14 and 22 meV for the lowest CEF levels [157].

6.2.1 Direct observation of the entire $4f$ splitting scheme

The determination of the $4f$ splittings is straightforward from $CeCo_2Ge_2$ RIXS data. The 7 CEF split states produce well separated peaks, which can be easily identified on the spectrum shown in Figure 6.6. The level's energies determined by fitting with Gaussians are 0 - 62 - 120 meV and 260 - 315 - 365 - 460 meV for the three $^2F_{5/2}$ and the four $^2F_{7/2}$-split states respectively. Moreover the features show different widths, especially those belonging to the $^2F_{7/2}$ multiplet.

The splittings are extremely large if compared to the other 122 cerium compounds, as a possible consequence of the strong $4f$ hybridization. The same applies for the peak widths, which may reflect the dispersive character of the $4f$ states observed in Ref. [159]. The influence of effects other than purely electrostatic might also explain the strong disagreement with the point-charge model predictions.

The possibility of a detailed study of such large splittings is a specific characteristic of RIXS spectroscopy. The large energy scales can indeed be the reason why $4f$ splittings in

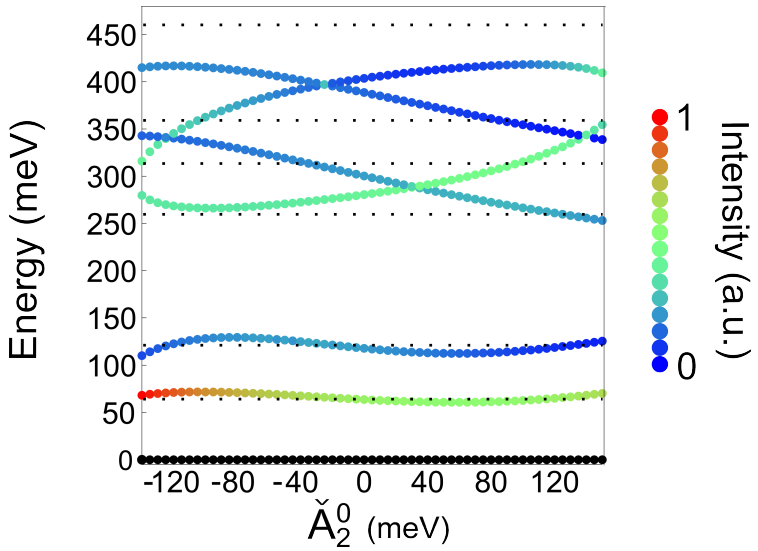

Figure 6.7: Calculated levels' energies varying $\check{A}_2^0$, after imposing the 62-120 meV splittings of the $^2F_{5/2}$ multiplet ($\check{A}_6^0, \check{A}_6^4 = 0$). Without the higher order parameters, the $^2F_{7/2}$ splittings (dotted lines) are not correctly reproduced for any $\check{A}_2^0$. The calculated peak intensities vary considerably with $\check{A}_2^0$.

$CeCo_2Ge_2$ have not been observed with techniques such as INS and specific heat, limited in maximum excitation energy.

6.2.2 Crystal electric field analysis

The observation of the $^2F_{7/2}$ levels' splittings on the spectra allows, in principle, for a more complete determination of the CEF potential. In fact, so far the analysis have been limited to the $^2F_{5/2}$ splittings, which, within Stevens' approximation, are determined by $\check{A}_2^0$ $\check{A}_4^0$ and $\check{A}_4^4$. The $^2F_{7/2}$ splittings are affected also by parameters of higher order, namely $\check{A}_6^0$ and $\check{A}_6^4$. The effect of these parameters is usually neglected when studying the CEF on cerium but must now be considered for a better interpretation of the $CeCo_2Ge_2$ RIXS spectra.

As a starting point, the method presented in section 4.2.3 can be employed, neglecting, for the moment, $\check{A}_6^0$ and $\check{A}_6^4$. The reduced set of parameters is determined as a function of $\check{A}_2^0$ by imposing the measured $^2F_{5/2}$ splittings in Equation 1.28. Figure 6.7 reports the calculated levels' energies and RIXS peaks' intensities varying $\check{A}_2^0$ (for σ polarisation, $2\theta = 150°$ and specular geometry). The calculated $^2F_{7/2}$ splittings don't match the measured values (dotted lines) for any $\check{A}_2^0$, confirming the need of higher order parameters to correctly describe these levels.

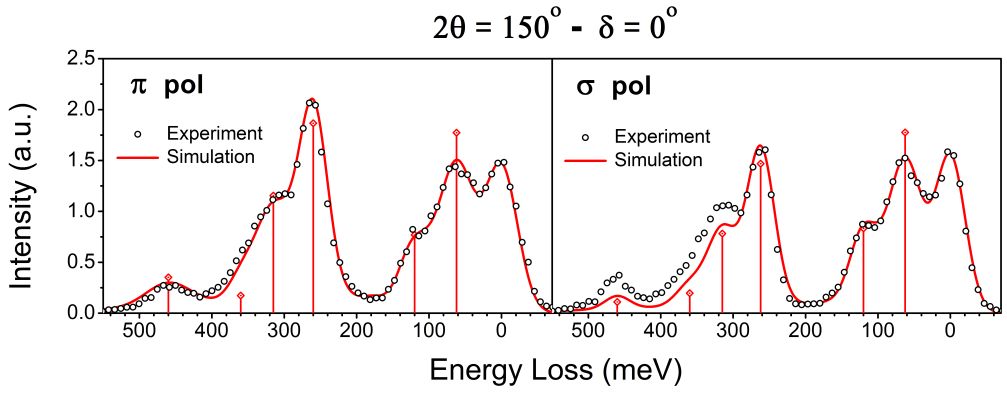

Figure 6.8: $CeCo_2Ge_2$ RIXS spectra at $2\theta = 150°$ and simulations with $\check{A}_2^0 = 17$ meV, $\check{A}_4^0 = -73$ meV, $\check{A}_4^4 = 377$ meV, $\check{A}_6^0 = 220$ meV and $\check{A}_6^4 = 200$ meV.

Moreover, the intensity of the first two peaks at 62 and 120 meV varies with $\check{A}_2^0$. This dependence was already observed in the analysis of $CeRh_2Si_2$ spectra (Figures 4.6 and 4.7), but it is here enhanced by the stronger CEF effects. Such a strong intensity variation can be used to determine the value of $\check{A}_2^0$, by comparison between calculations and measurements. In fact, the other methods presented in chapter 3 to find the $\check{A}_2^0$ value cannot be used for $CeCo_2Ge_2$. The magnetic susceptibility and XAS data are strongly affected by the $4f$ mixed valence, while the RIXS signal of the $^2F_{7/2}$ multiplet is influenced also by the $\check{A}_6^0$ and $\check{A}_6^4$ parameters.

After defining the possible (reduced) sets of parameters that reproduce the $^2F_{5/2}$ splittings, $\check{A}_6^0$ and $\check{A}_6^4$ shall be determined. This can be done by applying the same analysis of above, but now focusing on the $^2F_{7/2}$ states. The measured splittings are imposed in calculations and the best CEF scheme is chosen by comparing simulations to experimental data. In principle, the introduction of parameters of higher order should keep the $^2F_{5/2}$ splittings unvaried, as long as the relations among $\check{A}_2^0$, $\check{A}_4^0$ and $\check{A}_4^4$ are not changed. Yet, for such large splittings the Stevens' condition $\Delta E_{\text{CEF}} \ll \Delta E_{\text{spin-orbit}}$ is not satisfied and there is a non-negligible mixing between the two spin-orbit multiplets. As a consequence, the splittings of the $^2F_{5/2}$-derived states will be slightly modified by the introduction $\check{A}_6^0$ and $\check{A}_6^4$ and small corrections of the parameters are needed.

The final set of parameters is: $\check{A}_2^0 = 17$ meV, $\check{A}_4^0 = -73$ meV, $\check{A}_4^4 = 377$ meV, $\check{A}_6^0 = 220$ meV and $\check{A}_6^4 = 200$ meV. It allows to perfectly reproduce the experimental spectra at $2\theta = 150°$, as shown in Figure 6.8. Yet, simulations with these parameters are not able to fit the spectra acquired at $2\theta = 90°$ scattering angle (Figure 6.9). In particular, there is a strong disagreement between the calculated and observed intensities, while the shift of the

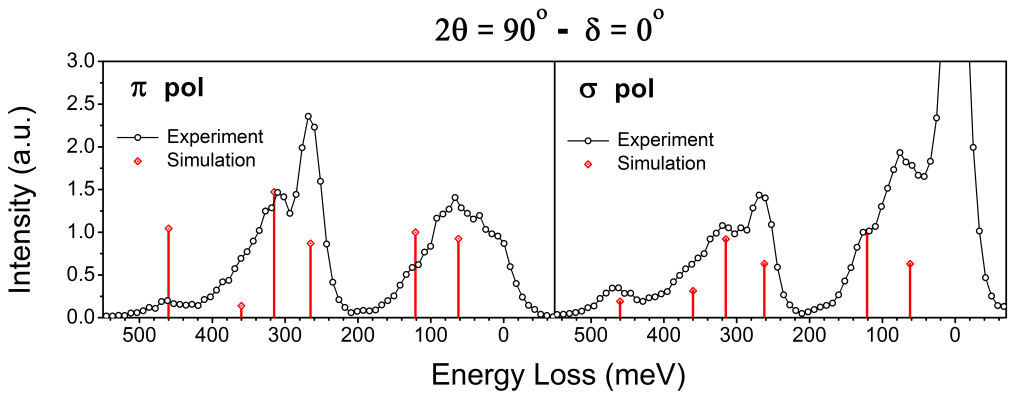

Figure 6.9: $CeCo_2Ge_2$ RIXS spectra at $2\theta = 90°$ and calculated cross sections. The simulations give intensity of the peaks that are very different from the measured ones.

peaks' positions is relatively small (within 3 and 10 meV).

Therefore the approach presented in this thesis, based on the CEF theory, fails to interpret the $CeCo_2Ge_2$ spectra. It is possible that the peak intensities are affected by interactions that cannot be explained with a simple CEF model. Further work is needed to understand the causes of the large splittings observed in $CeCo_2Ge_2$ and their effects on the RIXS cross sections. This first detection of unexpectedly large splittings is very interesting for the physics of cerium intermetallics, and would not have been possible with other techniques. Moreover, RIXS spectroscopy, by studying the polarisation and angular dependence of each feature, allows for a more precise analysis and interpretation of the data, thus providing a privileged tool for future studies on large $4f$ splittings.

Chapter 7

Summary and outlook

Resonant Inelastic soft X-ray Scattering (soft-RIXS) has been presented as a new tool to probe the properties of $4f$ states in cerium intermetallic compounds. The physics of $4f$ electrons, typically characterized by low energy scales, became accessible to soft-RIXS in the last years, with the construction and commissioning of the ID32 beamline and the *ERIXS* high-resolution spectrometer at ESRF. The design and functioning of this world-leading instrument have been presented in detail, paying particular attention to the most important innovations. The example of $CeRh_2Si_2$ has been used to discuss the information that can be retrieved from high-resolution RIXS spectra at the M_5 edge. In particular, it was possible to determine the $4f$ states' splittings and symmetry within the crystal electric field model, by comparing the experimental spectra to full-multiplet single-ion simulations. A general procedure for data analysis was also outlined, providing a guideline for the future works. Further insight was obtained by analyzing the polarisation and momentum dependencies of the ff transitions. The polarisation analysis of the scattered beam revealed the orientation of the wavefunctions in the crystal ab plane and confirmed the crystal-field splitting scheme. A variation of the measured splittings with the scattering geometry was detected, unveiling effects of the $4f$ states' dispersion in RIXS spectroscopy. A first interpretation of the observed peaks' shifts was illustrated with a simplified model. The final result of the presented analysis on $CeRh_2Si_2$ gave a Γ_7^1 - Γ_6 - Γ_7^2 splitting scheme for the lowest $4f$ levels ($^2F_{5/2}$ multiplet), with energies and dispersions compatible with resonant photoemission data. No temperature dependence of the ff transitions across $T_{\text{Nèel}}$ has been detected.

The example of $CeRh_2Si_2$ shows that a complete crystal-field analysis can be performed with RIXS on $4f$ splittings comparable to the experimental resolution (35 meV). An investigation of smaller splittings is possible, by exploiting the angular and polarisation dependence of the ff cross-sections. The first spectra of $CeCu_2Si_2$ revealed the presence of a peak at

energies higher than expected, which would disprove the currently accepted crystal field scheme. Yet the results are uncertain due to both the insufficient resolution and a broad feature in the same energy range probably of charge transfer nature. Large splittings allow instead to clearly resolve and study all the ff transitions, including the excitations into the $^2F_{7/2}$ states. This was shown with the example of $CeCo_2Ge_2$. However, in this case the presented crystal-field approach failed in the interpretation of the data. The simulations could not in fact reproduce the cross-sections variation with the scattering geometry, suggesting the influence of phenomena not considered within the crystal-field theory.

The demonstrated ability of RIXS to probe the ff transitions opens up many possibilities for future studies. In particular, the angular dependence of the measured splittings needs to be addressed both with systematic experiments and theoretical work. A detailed mapping of these effects will provide deeper insight in the $4f$ states' energies, hybridization and dispersion. Yet, this will be possible only if a refined model for the interpretation of the measured effects will be available. The broad peak detected around 100 meV in both $CeRh_2Si_2$ and $CeCu_2Si_2$ and the anomalous spectra of $CeCo_2Ge_2$ also deserve further investigation. The interactions of the $4f$ levels with the surroundings cause indeed modifications of the spectra that need to be understood for a more accurate comparison between simulations and measurements.

In the future, the RIXS investigation of $4f$ levels will benefit from further technological advances. New soft-RIXS spectrometers are in construction in many facilities, as NSLS-II in Brookhaven (NY, USA), MAX-IV in Lund (Sweden), Diamond Light Source (UK) and NSRRC (Taiwan). With the expected improvements in the experimental resolution smaller splittings will become accessible and an even more detailed analysis will be possible. This thesis explored the potential of RIXS and laid the groundwork for new studies on the physics of $4f$ electrons. Soft-RIXS demonstrated to be complementary to traditional techniques and free of many of their disadvantages. Its greatest limitation, the experimental resolution, is being overcome thanks to the rapid improvements of the instrumentation. With the present work, a new field of research opens up and brings a wealth of new possibilities to probe the fascinating properties of rare-earth compounds.

Bibliography

[1] G. R. Stewart. Heavy-fermion systems. *Reviews Modern Physics*, 56:755–787, Oct 1984.

[2] P. Misra. Chapter 1: Overview of heavy fermion systems. In *Heavy-Fermion Systems*, volume 2 of *Handbook of Metal Physics*, pages 1 – 7. Elsevier, 2008.

[3] P. Coleman. *Heavy Fermions: electrons at the edge of magnetism*, volume 1 of *Handbook of Magnetism and Advanced Magnetic Materials*. 2006.

[4] D. I. Khomskii. *Basic aspects of the quantum theory of solids: order and elementary excitations*. Cambridge University Press, 2010.

[5] F. Stigari. Hybridization and crystal-field effects in Kondo insulators studied by means of core-level spectroscopy. *PhD Thesis, Cologne*, 2015.

[6] P. S. Riseborough. Heavy fermion semiconductors. *Advances in Physics*, 49(3):257–320, 2000.

[7] W. J. de Haas, J. de Boer, and G.J. van den Berg. The electrical resistance of gold, copper and lead at low temperatures. *Physica*, 1(7):1115 – 1124, 1934.

[8] G. J. van den Berg. Anomalies in dilute metallic solutions of transition metals. In *Low Temperature Physics LT9*, pages 955–984. Springer, 1965.

[9] J. Kondo. Resistance minimum in dilute magnetic alloys. *Progress of theoretical physics*, 32(1):37–49, 1964.

[10] P. W. Anderson. Localized magnetic states in metals. *Physical Review*, 124:41–53, Oct 1961.

[11] K. Andres, J. E. Graebner, and H. R. Ott. 4 f-virtual-bound-state formation in $CeAl_3$ at low temperatures. *Physical Review Letters*, 35(26):1779, 1975.

[12] S. Doniach. The Kondo lattice and weak antiferromagnetism. *Physica B+C*, 91:231 – 234, 1977.

[13] E. Bucher, J. P. Maita, G. W. Hull, R. C. Fulton, and A. S. Cooper. Electronic properties of beryllides of the rare earth and some actinides. *Physical Review B*, 11(1):440, 1975.

[14] L. N. Cooper. Bound electron pairs in a degenerate Fermi gas. *Physical Review*, 104(4):1189, 1956.

[15] F. Steglich, J. Aarts, C. D. Bredl, W. Lieke, D. Meschede, W. Franz, and H. Schäfer. Superconductivity in the presence of strong Pauli paramagnetism: $CeCu_2Si_2$. *Physical Review Letters*, 43:1892–1896, Dec 1979.

[16] H. v. Löhneysen, T. Pietrus, G. Portisch, H. G. Schlager, A. Schröder, M. Sieck, and T. Trappmann. Non-Fermi-liquid behavior in a heavy-fermion alloy at a magnetic instability. *Physical Review Letters*, 72:3262–3265, May 1994.

[17] D. Aoki, W. Knafo, and I. Sheikin. Heavy fermions in a high magnetic field. *Comptes Rendus Physique*, 14(1):53–77, 2013.

[18] G. R. Stewart. Non-Fermi-liquid behavior in d-and f-electron metals. *Reviews of modern Physics*, 73(4):797, 2001.

[19] C. Pfleiderer. Superconducting phases of f-electron compounds. *Reviews of Modern Physics*, 81(4):1551, 2009.

[20] L. D. Landau. The theory of a Fermi liquid. *Soviet Physics Jetp-USSR*, 3(6):920–925, 1957.

[21] S. Panwar and I. Singh. Magnetic susceptibility of heavy fermions and mixed-valence systems. *Physica Status Solidi B*, 168(2):583–590, 1991.

[22] G. M. Carneiro and C. J. Pethick. Finite-temperature contributions to the magnetic susceptibility of a normal Fermi liquid. *Physical Review B*, 16(5):1933, 1977.

[23] K. G. Wilson. The renormalization group: Critical phenomena and the Kondo problem. *Reviews Modern Physics*, 47:773–840, Oct 1975.

[24] K. Kadowaki and S. B. Woods. Universal relationship of the resistivity and specific heat in heavy-fermion compounds. *Solid State Communications*, 58(8):507 – 509, 1986.

[25] G. Knebel, D. Aoki, and J. Flouquet. Antiferromagnetism and superconductivity in cerium based heavy-fermion compounds. *Comptes Rendus Physique*, 12(5):542–566, 2011.

[26] Piers Coleman and Andrew J Schofield. Quantum criticality. *Nature*, 433(7023):226–229, 2005.

[27] Q. Si, S. Rabello, K. Ingersent, and J. L. Smith. Locally critical quantum phase transitions in strongly correlated metals. *Nature*, 413(6858):804–808, 2001.

[28] A. T. Holmes, D. Jaccard, and K. Miyake. Valence instability and superconductivity in heavy fermion systems. *Journal of the Physical Society of Japan*, 76(5):051002, 2007.

[29] F. Thomas, J. Thomasson, C. Ayache, C. Geibel, and F. Steglich. Precise determination of the pressure dependence of T_c in the heavy-fermion superconductor $CeCu_2Si_2$. *Physica B: Condensed Matter*, 186:303 – 306, 1993.

[30] H. Q. Yuan, F. M. Grosche, M. Deppe, C. Geibel, G. Sparn, and F. Steglich. Observation of two distinct superconducting phases in $CeCu_2Si_2$. *Science*, 302(5653):2104–2107, 2003.

[31] K. Miyake. New trend of superconductivity in strongly correlated electron systems. *Journal of Physics: Condensed Matter*, 19(12):125201, 2007.

[32] J.-P. Rueff, S. Raymond, M. Taguchi, M. Sikora, J.-P. Itié, F. Baudelet, D. Braithwaite, G. Knebel, and D. Jaccard. Pressure-induced valence crossover in superconducting $CeCu_2Si_2$. *Physical Review Letters*, 106:186405, May 2011.

[33] K. Fujiwara, Y. Hata, K. Kobayashi, K. Miyoshi, J. Takeuchi, Y. Shimaoka, Hhi K., T. V. Kobayashi, C. Geibel, and F. Steglich. High pressure NQR measurement in $CeCu_2Si_2$ up to sudden disappearance of superconductivity. *Journal of the Physical Society of Japan*, 77(12):123711, 2008.

[34] K. Hattori. Meta-orbital transition in heavy-fermion systems: Analysis by dynamical mean field theory and self-consistent renormalization theory of orbital fluctuations. *Journal of the Physical Society of Japan*, 79(11):114717, 2010.

[35] L. V. Pourovskii, P. Hansmann, M. Ferrero, and A. Georges. Theoretical prediction and spectroscopic fingerprints of an orbital transition in $CeCu_2Si_2$. *Physical Review Letters*, 112:106407, Mar 2014.

[36] G. Zwicknagl. Quasi-particles in heavy fermion systems. *Advances in Physics*, 41(3):203–302, 1992.

[37] O. Gunnarsson and N. E. Christensen. Crystal-field and configuration dependence of hopping-matrix elements for $CeCu_2Si_2$. *Physical Review B*, 42:2363–2367, Aug 1990.

[38] Y. Matsumoto, K. Kuga, T. Tomita, Y. Karaki, and S. Nakatsuji. Anisotropic heavy-Fermi-liquid formation in valence-fluctuating α-$YbAlB_4$. *Physical Review B*, 84:125126, Sep 2011.

[39] G. Zwicknagl and U. Pulst. $CeCu_2Si_2$: Renormalized band structure, quasiparticles and co-operative phenomena. *Physica B: Condensed Matter*, 186:895 – 898, 1993.

[40] I. Eremin, G. Zwicknagl, P. Thalmeier, and P. Fulde. Feedback spin resonance in superconducting $CeCu_2Si_2$ and $CeCoIn_5$. *Physical Review Letters*, 101:187001, Oct 2008.

[41] A. H. Nevidomskyy and P. Coleman. Layered Kondo lattice model for quantum critical β-$YbAlB_4$. *Physical Review Letters*, 102:077202, Feb 2009.

[42] R. Flint and P. Coleman. Tandem pairing in heavy-fermion superconductors. *Physical Review Letters*, 105:246404, Dec 2010.

[43] T. Willers, F. Strigari, N. Hiraoka, Y. Q. Cai, M. W. Haverkort, K.-D. Tsuei, Y. F. Liao, S. Seiro, C. Geibel, F. Steglich, L. H. Tjeng, and A. Severing. Determining the in-plane orientation of the ground-state orbital of $CeCu_2Si_2$. *Physical Review Letters*, 109:046401, Jul 2012.

[44] E. U. Condon and G.H. Shortley. The Theory of Atomic Spectra. *Cambridge University Press, Cambridge*, 1:158, 1935.

[45] Z. B. Goldschmidt. Chapter 1: Atomic properties (free atom). In *Metals*, volume 1 of *Handbook on the Physics and Chemistry of Rare Earths*, pages 1 – 171. North-Holland, Amsterdam, 1978.

[46] J. C. Slater. The theory of complex spectra. *Physical Review*, 34:1293–1322, Nov 1929.

[47] M. W. Haverkort. Spin and orbital degrees of freedom in transition metal oxides and oxide thin films studied by soft X-ray absorption spectroscopy. *PhD Thesis, Cologne*, 2005.

[48] F. de Groot. Multiplet effects in X-ray spectroscopy. *Coordination Chemistry Reviews*, 249(1):31–63, 2005.

[49] Robert D Cowan. *The theory of atomic structure and spectra*. Number 3. Univ of California Press, 1981.

[50] B. T. Thole, G. van der Laan, J. C. Fuggle, G. A. Sawatzky, R. C. Karnatak, and J.-M. Esteva. *3d* X-ray-absorption lines and the $3d^9 4f^{n+1}$ multiplets of the lanthanides. *Physical Review B*, 32:5107–5118, Oct 1985.

[51] T. Willers, D. T. Adroja, B. D. Rainford, Z. Hu, N. Hollmann, P. O. Körner, Y.-Y. Chin, D. Schmitz, H. H. Hsieh, H.-J. Lin, C. T. Chen, E. D. Bauer, J. L. Sarrao, K. J. McClellan, D. Byler, C. Geibel, F. Steglich, H. Aoki, P. Lejay, A. Tanaka, L. H. Tjeng, and A. Severing. Spectroscopic determination of crystal-field levels in $CeRh_2Si_2$ and $CeRu_2Si_2$ and of the $4f^0$ contributions in CeM_2Si_2 (M=Cu, Ru, Rh, Pd, and Au). *Physical Review B*, 85:035117, Jan 2012.

[52] P. Fulde. Chapter 17: Crystal fields. In *Alloys and Intermetallics*, volume 2 of *Handbook on the Physics and Chemistry of Rare Earths*, pages 295 – 386. Elsevier, 1979.

[53] M. Rotter. *McPhase User Manual.* http://www2.cpfs.mpg.de∼rotter/homepage_mcphase/manual/manual.html.

[54] G. Liu. *Electronic Energy Level Structure*, pages 1–94. Springer Berlin Heidelberg, Berlin, Heidelberg, 2005.

[55] K. N. R. Taylor and M. I. Darby. Physics of rare earth solids. 1972.

[56] V. R. Sastri, J. R. Perumareddi, V. Ramachandra Rao, G. V. S. Rayudu, and J.-C. G. Bünzli. *Modern aspects of rare earths and their complexes*. Elsevier, 2003.

[57] D. J. Newman and B. Ng. *Crystal field handbook*. Cambridge University Press, 2007.

[58] C. Görller-Walrand and K. Binnemans. Chapter 155: Rationalization of crystal-field parametrization. volume 23 of *Handbook on the physics and chemistry of rare earths*, pages 121–283. North-Holland, Amsterdam, 1996.

[59] K. W. H. Stevens. Matrix elements and operator equivalents connected with the magnetic properties of rare earth ions. *Proceedings of the Physical Society. Section A*, 65(3):209, 1952.

[60] J. Sievers. Asphericity of $4f$-shells in their Hund's rule ground states. *Zeitschrift für Physik B Condensed Matter*, 45(4):289–296, 1982.

[61] G. H. Dieke, H. M. Crosswhite, and H. Crosswhite. *Spectra and energy levels of rare earth ions in crystals*. Interscience Publishers New York, 1968.

[62] S. Hufner. *Optical spectra of transparent rare earth compounds*. Elsevier, 2012.

[63] G.S. Ofelt. Intensities of crystal spectra of rare earth ions. *The Journal of Chemical Physics*, 37(3):511–520, 1962.

[64] K. Baberschke. Crystal electric field effects in the ESR of dilute alloys. In *Crystalline Electric Field Effects in f-Electron Magnetism*, pages 101–112. Springer, 1982.

[65] R. G. Barnes. NMR, EPR and Mössbauer effect: metals, alloys and compounds. *Handbook on the Physics and Chemistry of Rare Earths*, 2:387–505, 1979.

[66] P. Fulde and M. Loewenhaupt. Magnetic excitations in crystal-field split $4f$ systems. *Advances in Physics*, 34(5):589–661, 1985.

[67] E. Borchi and S. De Gennaro. Kondo effect in cerium intermetallics: Magnetic susceptibility. *Physical Review B*, 14(5):1989, 1976.

[68] Z. S. Liu. The susceptibilities and molecular-field constants of rare-earth compounds from mean-field theory. *Materials Letters*, 58(25):3111–3114, 2004.

[69] B. C. Sales and D. K. Wohlleben. Susceptibility of interconfiguration-fluctuation compounds. *Physical Review Letters*, 35(18):1240, 1975.

[70] A. Hideki, K. Hideaki, S. Hiroyuki, K. Giyuu, and M. Takehiko. Magnetic properties of $CeRh_2Si_2$ and $CePd_2Si_2$ single crystals. *Journal of Magnetism and Magnetic Materials*, 177:479 – 480, 1998.

[71] R. Settai, A. Misawa, S. Araki, M. Kosaki, K. Sugiyama, T. Takeuchi, K. Kindo, Y. Haga, E. Yamamoto, and Y. Ōnuki. Single crystal growth and magnetic properties of $CeRh_2Si_2$. *Journal of the Physical Society of Japan*, 66(8):2260–2263, 1997.

[72] H. Meyer and P. L. Smith. The heat capacities of seven rare-earth ethylsulphates at low temperature. *Journal of Physics and Chemistry of Solids*, 9(3):285–295, 1959.

[73] S. Patil, K. Kummer, A. Hannaske, C. Krellner, M. Kuhnt, S Danzenbächer, C. Laubschat, C. Geibel, and D. V. Vyalikh. Crystalline electric field splitting of $4f$ states in $YbIr_2Si_2$: An ARPES view. *Proceedings of the International Conference on Strongly Correlated Electron Systems (SCES2013)*.

[74] E. A. Goremychkin, A. Y. Muzychka, and R. Osborn. Crystal field effects in $RCu_2 2Si_2$ compounds (R= Ce, Pr, Nd, Ho, Er): Inelastic neutron scattering investigation. *Journal of Experimental and Theoretical Physics*, 83(4):738–746, 1996.

[75] D. Cribier and B. Jacrot. Difusion des neutrons et effet Stark cristallin dans les oxydes de terre rare. *Comptes rendus hebdomadaires des seances de l' academie des sciences*, 250(17):2871–2873, 1960.

[76] R. M. Moon, T. Riste, and W. C. Koehler. Polarization analysis of thermal-neutron scattering. *Physical Review*, 181:920–931, May 1969.

[77] T. Jo and S. Imada. Calculation of linear dichroism in the Ce $4d$-Core XAS and $4f$ electronic state of $CeRh_3B_2$. *Journal of the Physical Society of Japan*, 59(7):2312–2315, 1990.

[78] K. Yamaguchi, H. Namatame, A. Fujimori, T. Koide, T. Shidara, M. Nakamura, A. Misu, H. Fukutani, M. Yuri, M. Kasaya, H. Suzuki, and T. Kasuya. Soft-X-ray linear-dichroism and magnetic-circular-dichroism studies of $CeRh_3B_2$: Large crystal-field splitting and anomalous ferromagnetism. *Physical Review B*, 51:13952–13960, May 1995.

[79] P. Hansmann, A. Severing, Z. Hu, M. W. Haverkort, C. F. Chang, S. Klein, A. Tanaka, H. H. Hsieh, H.-J. Lin, C. T. Chen, B. Fåk, P. Lejay, and L. H. Tjeng. Determining the crystal-field ground state in rare earth heavy fermion materials using soft-X-ray absorption spectroscopy. *Physical Review Letters*, 100:066405, Feb 2008.

[80] F. Givord, J. X. Boucherle, E. Lelievre-Berna, and P. Lejay. The cerium magnetic form factor and diffuse polarization in $CeRh_3B_2$ as functions of temperature. *Journal of Physics: Condensed Matter*, 16(8):1211, 2004.

[81] M. Höppner, S. Seiro, A. Chikina, A. Fedorov, M. Güttler, S. Danzenbächer, A. Generalov, K. Kummer, S. Patil, S. L. Molodtsov, Y. Kucherenko, C. Geibel, V. N. Strocov, M. Shi, M. Radovic, T. Schmitt, Laubschat C., and D. V. Vyalikh. Interplay of Dirac fermions and heavy quasiparticles in solids. *Nature communications*, 4:1646, 2013.

[82] M. Sundermann, F. Strigari, T. Willers, H. Winkler, A. Prokofiev, J. M. Ablett, J.-P. Rueff, D. Schmitz, E. Weschke, M. Moretti Sala, A. Al-Zein, A. Tanaka, M. W. Haverkort, D. Kasinathan, L. Hao Tjeng, S. Paschen, and S. Severing. $CeRu_4Sn_6$: a strongly correlated material with nontrivial topology. *Scientific reports*, 5, 2015.

[83] B. T. Thole, G. Van der Laan, and G. A. Sawatzky. Strong magnetic dichroism predicted in the $M_{4,5}$ X-ray absorption spectra of magnetic rare-earth materials. *Phys.l Rev. Lett.*, 55(19):2086, 1985.

[84] K. Chen, F. Strigari, M. Sundermann, S. Agrestini, N. J. Ghimire, S.-Z. Lin, C. D. Batista, E. D. Bauer, J. D. Thompson, E. Otero, A. Tanaka, and A. Severing. Exchange field effect in the crystal-field ground state of $CeMAl_4Si_2$. *Physical Review B*, 94:115111, Sep 2016.

[85] T. Mori, S. Kitayama, Y. Kanai, S. Naimen, H. Fujiwara, K. Higashiya, A. Tamasaku, A. Tanaka, K. Terashima, S. Imada, A. Yasui, Y. Saitoh, K. Yamagami, K. Yano, T. Matsumoto, T. Kiss, T. Yabashi, M. Ishikawa, S. Suga, Y. Onuki, T. Ebihara, and A. Sekiyama. Probing strongly correlated $4f$-orbital symmetry of the ground state in Yb compounds by linear dichroism in core-level photoemission. *Journal of the Physical Society of Japan*, 83(12):123702, 2014.

[86] D. Ehm, S. Hüfner, F. Reinert, J. Kroha, P. Wölfle, O. Stockert, C. Geibel, and H. v. Löhneysen. High-resolution photoemission study on low-T K Ce systems: Kondo resonance, crystal field structures, and their temperature dependence. *Physical Review B*, 76(4):045117, 2007.

[87] P. Weibel, M. Grioni, D. Malterre, B. Dardel, and Y. Baer. Resonant inverse photoemission: A new probe of correlated systems. *Physical Review Letters*, 72:1252–1255, Feb 1994.

[88] S. Patil, A. Generalov, M. Güttler, P. Kushwaha, A. Chikina, K. Kummer, T. C. Rödel, A. F. Santander-Syro, N. Caroca-Canales, C. Geibel, S. Danzenbächer, Laubschat C. and. Allen J. W. Kucherenko, Y., and D. V. Vyalikh. ARPES view on surface and bulk hybridization phenomena in the antiferromagnetic Kondo lattice $CeRh_2Si_2$. *Nature communications*, 7, 2016.

[89] L. J. P. Ament, G. Ghiringhelli, M. Moretti Sala, L. Braicovich, and J. van den Brink. Theoretical demonstration of how the dispersion of magnetic excitations in cuprate compounds can be determined using resonant inelastic X-ray scattering. *Physical Review Letters*, 103(11):117003, 2009.

[90] P. Glatzel, M. Sikora, and M. Fernandez-Garcia. Resonant X-ray spectroscopy to study K absorption pre-edges in $3d$ transition metal compounds. *The European Physical Journal Special Topics*, 169(1):207–214, 2009.

[91] M. Matsubara, T. Uozumi, A. Kotani, Y. Harada, and S. Shin. Polarization dependence of resonant X-ray emission spectra in early transition metal compounds. *Journal of the Physics Society Japan*, 69(5):1558–1565, 2000.

[92] L. J. P. Ament, M. Van Veenendaal, T. P. Devereaux, J. P. Hill, and J. Van Den Brink. Resonant inelastic X-ray scattering studies of elementary excitations. *Reviews of Modern Physics*, 83(2):705, 2011.

[93] J. Singh, C. Lamberti, and J. A. van Bokhoven. Advanced X-ray absorption and emission spectroscopy: in situ catalytic studies. *Chemical Society Reviews*, 39(12):4754–4766, 2010.

[94] A. Kotani and S. Shin. Resonant inelastic X-ray scattering spectra for electrons in solids. *Reviews of Modern Physics*, 73(1):203, 2001.

[95] S. G. Chiuzbăian, G. Ghiringhelli, C. Dallera, M. Grioni, P. Amann, X. Wang, L. Braicovich, and L. Patthey. Localized electronic excitations in NiO studied with resonant inelastic X-ray scattering at the Ni M threshold: Evidence of spin flip. *Physical Review Letters*, 95(19):197402, 2005.

[96] G. Ghiringhelli, N. B. Brookes, E. Annese, H. Berger, C. Dallera, M. Grioni, L. Perfetti, A. Tagliaferri, and L. Braicovich. Low energy electronic excitations in the layered cuprates studied by copper L_3 Resonant Inelastic X-Ray Scattering. *Physical Review Letters*, 92(11):117406, 2004.

[97] L. J. P. Ament, G. Khaliullin, and J. Van den Brink. Resonant inelastic X-ray scattering on spin-orbit coupled insulating iridates. *arXiv preprint arXiv:1008.4862*, 2010.

[98] M. Moretti Sala. Magnetic and orbital resonant inelastic X-ray scattering. *PhD Thesis, Milano*, 2011.

[99] L. Braicovich, J. van den Brink, V. Bisogni, M. Moretti Sala, L. J. P. Ament, N. B. Brookes, G. M. De Luca, M. Salluzzo, T. Schmitt, V. N. Strocov, and G. Ghiringhelli. Magnetic excitations and phase separation in the underdoped $La_{2-x}Sr_xCuO_4$ superconductor measured by resonant inelastic X-ray scattering. *Physical Review Letters*, 104(7):077002, 2010.

[100] H. Yavaş, M. Van Veenendaal, J. van den Brink, L. J. P. Ament, A. Alatas, B. M. Leu, M. O. Apostu, N. Wizent, G. Behr, W. Sturhahn, H. Sinn, and E. E. Alp. Observation of phonons with resonant inelastic X-ray scattering. *Journal of Physics: Condensed Matter*, 22(48):485601, 2010.

[101] G. Ghiringhelli, M. Le Tacon, M. Minola, S. Blanco-Canosa, C. Mazzoli, N. B. Brookes, G. M. De Luca, A. Frano, D. G. Hawthorn, F. He, T. Loew, M. Moretti Sala, D. C. Peets, M. Salluzzo, E. Schierle, R. Sutarto, G. A. Sawatzky, E. Weschke, B. Keimer, and L. Braicovich. Long-range incommensurate charge fluctuations in (Y,Nd)Ba2Cu3O6+x. *Science*, 337(6096):821–825, 2012.

[102] A. Amorese, G. Dellea, M. Fanciulli, S. Seiro, C. Geibel, C. Krellner, I. P. Makarova, L. Braicovich, G. Ghiringhelli, D. V. Vyalikh, N. B. Brookes, and K. Kummer. $4f$ excitations in Ce Kondo lattices studied by resonant inelastic X-ray scattering. *Physical Review B*, 93:165134, Apr 2016.

[103] E. A. Goremychkin and R. Osborn. Crystal-field excitations in $CeCu_2Si_2$. *Physical Review B*, 47:14280–14290, Jun 1993.

[104] M. Nakazawa, S. Tanaka, T. Uozumi, and A. Kotani. Theory of resonant X-ray emission spectra in Ce compounds. *Journal of the Physical Society of Japan*, 65(7):2303–2310, 1996.

[105] M. Nakazawa, H. Ogasawara, and A. Kotani. Theory of polarization dependence in resonant X-ray emission spectroscopy of Ce compounds. *Journal of the Physical Society of Japan*, 69(12):4071–4077, 2000.

[106] M. Watanabe, Y. Harada, M. Nakazawa, Y. Ishiwata, R. Eguchi, T. Takeuchi, A. Kotani, and S. Shin. Polarization dependence of resonant soft X-ray emission spectra in Ce compounds. *Surface Review and Letters*, 9(02):983–987, 2002.

[107] M. Nakazawa and A. Kotani. Theoretical study on the effect of electron-hole pair excitations in resonant X-ray emission spectroscopy for Ce intermetallic compounds. *Journal of the Physical Society of Japan*, (11):2804–2814, 2002.

[108] C. Dallera, K. Giarda, G. Ghiringhelli, A. Tagliaferri, L. Braicovich, and N. B. Brookes. Charge-transfer excitations in lanthanum compounds measured by resonant inelastic X-ray scattering at the M_5 edge. *Physical Review B*, 64(15):153104, 2001.

[109] W. Lenth, F. Lutz, J. Barth, G. Kalkoffen, and C. Kunz. Giant resonance enhancement of the $4f$, $5p$, and $5s$ states in the photoemission spectra of rare-earth compounds. *Physical Review Letters*, 41:1185–1188, Oct 1978.

[110] S. Tanaka, Y. Kayanuma, and A. Kotani. Theory of the resonant $5p \rightarrow 3d$ X-ray emission spectra in CeO_2. *Journal of the Physical Society of Japan*, 59(4):1488–1495, 1990.

[111] P. Wang, H.and Bencok, P. Steadman, E. Longhi, J. Zhu, and Z. Wang. Complete polarization analysis of an APPLE II undulator using a soft X-ray polarimeter. *Journal of Synchrotron Radiation*, 19(6):944–948, Nov 2012.

[112] University of Winsconsin Madison website. http://www.src.wisc.edu.

[113] S. Sasaki, K. Kakuno, T. Takada, T. Shimada, K. Yanagida, and Y. Miyahara. Design of a new type of planar undulator for generating variably polarized radiation. *Nuclear Instruments and Methods in Physics Research Section A: Accelerators, Spectrometers, Detectors and Associated Equipment*, 331(1):763–767, 1993.

[114] M. Fujisawa, A. Harasawa, A. Agui, M. Watanabe, A. Kakizaki, S. Shin, T. Ishii, T. Kita, T. Harada, Y. Saitoh, and S. Suga. Varied line spacing plane grating monochromator for undulator beamline. *Review of Scientific Instruments*, 67(2):345–349, 1996.

[115] H. Petersen, C. Jung, C. Hellwig, W. B. Peatman, and W. Gudat. Review of plane grating focusing for soft X-ray monochromators. *Review of Scientific Instruments*, 66(1):1–14, 1995.

[116] K. Kummer, A. Fondacaro, E. Jimenez, E. Velez-Fort, A. Amorese, M. Aspbury, F. Yakhou-Harris, P. van der Linden, and N. B. Brookes. The high-field magnet endstation for X-ray magnetic dichroism experiments at ESRF soft X-ray beamline ID32. *Journal of synchrotron radiation*, 23(2), 2016.

[117] G. Ghiringhelli, A. Piazzalunga, C. Dallera, G. Trezzi, L. Braicovich, T. Schmitt, V. N. Strocov, R. Betemps, L. Patthey, X. Wang, and M. Grioni. SAXES, a high resolution spectrometer for resonant X-ray emission in the 400-1600 eV energy range. *Review of Scientific Instruments*, 77(11):113108, 2006.

[118] L. Braicovich, M. Minola, G. Dellea, M. Le Tacon, M. Moretti Sala, C. Morawe, J. C. Peffen, R. Supruangnet, F. Yakhou, G. Ghiringhelli, and N. B. Brookes. The simultaneous measurement of energy and linear polarization of the scattered radiation in resonant inelastic soft X-ray scattering. *Review of Scientific Instruments*, 85(11):115104, 2014.

[119] L. C. Duda, P. Kuiper, D. C. Mancini, C. J. Englund, and J. Nordgren. A helicity resolving soft X-ray emission spectrometer for studying magnetic circular dichroism with laboratory excitation sources. *Nuclear Instruments and Methods in Physics Research Section A: Accelerators, Spectrometers, Detectors and Associated Equipment*, 376(2):291–297, 1996.

[120] K. Ishii, S. Ishihara, Y. Murakami, K. Ikeuchi, K. Kuzushita, T. Inami, K. Ohwada, M. Yoshida, I. Jarrige, N. Tatami, S. Niioka, D. Bizen, Y. Ando, J. Mizuki, S. Maekawa, and Y. Endoh. Polarization-analyzed resonant inelastic x-ray scattering of the orbital excitations in $KCuF_3$. *Physical Review B*, 83:241101, Jun 2011.

[121] Kurt kummer, private communication.

[122] A. Amorese, G. Dellea, and G. Braicovich, L.and Ghiringhelli. Enhancing spatial resolution of soft X-ray CCD detectors by single-photon centroid determination. *arXiv preprint arXiv:1410.1587*, 2014.

[123] A. Amorese. Single photon acquisition in CCD detectors for high resolution resonant inelastic soft x-ray scattering. 2013.

[124] M. R. Soman, D. J. Hall, J. H. Tutt, N. J. Murray, A. D. Holland, T. Schmitt, J. Raabe, and B. Schmitt. Improving the spatial resolution of a soft X-ray Charge Coupled Device used for resonant inelastic X-ray scattering. *Journal of Instrumentation*, 6(11):C11021, 2011.

[125] D. J. Hall, M. Soman, J. Tutt, N. Murray, A. Holland, T. Schmitt, J. Raabe, V. N. Strocov, and B. Schmitt. Improving the resolution in soft X-ray emission spectrometers through photon-counting using an electron multiplying CCD. *Journal of Instrumentation*, 7(01):C01063, 2012.

[126] C. Langini. *Advances in the detection at the new XMCD and RIXS beamline of the ESRF*. Master Thesis, Politecnico di Milano, 2015.

[127] C. Godart, L. C. Gupta, and M. F. Ravet-Krill. Investigations of the magnetic properties of $CeRh_2Si_2$ using lattice parameter, LIII edge and extended X-ray absorption fine structure measurements. *Journal of the Less Common Metals*, 94(1):187 – 193, 1983.

[128] S. Quezel, J. Rossat-Mignod, B. Chevalier, P. Lejay, and J. Etourneau. Magnetic ordering in $TbRh_2Si_2$ and $CeRh_2Si_2$. *Solid state communications*, 49(7):685–691, 1984.

[129] S. Kawarazaki, M. Sato, Y. Miyako, N. Chigusa, K. Watanabe, N. Metoki, Y. Koike, and M. Nishi. Ground-state magnetic structure of $CeRh_2Si_2$ and the response to hydrostatic pressure as studied by neutron diffraction. *Physical Review B*, 61(6):4167, 2000.

[130] B. H. Grier, J. M. Lawrence, V. Murgai, and R. D. Parks. Magnetic ordering in CeM_2Si_2 (M= Ag, Au, Pd, Rh) compounds as studied by neutron diffraction. *Physical Review B*, 29(5):2664, 1984.

[131] T. Graf, M. F. Hundley, R. Modler, R. Movshovich, J. D. Thompson, D. Mandrus, R. A. Fisher, and N. E. Phillips. Magnetic phase transitions in $CeRh_2Si_2$: specific heat, susceptibility and resistance studies. *Physical Review B*, 57:7442–7445, Apr 1998.

[132] R. Movshovich, T. Graf, D. Mandrus, J. D. Thompson, J. L. Smith, and Z. Fisk. Superconductivity in heavy-fermion $CeRh_2Si_2$. *Physical Review B*, 53:8241–8244, Apr 1996.

[133] J. D. Thompson, R. D. Parks, and H. Borges. Effect of pressure on the Néel temperature of Kondo-lattice systems. *Journal of Magnetism and Magnetic Materials*, 54:377–378, 1986.

[134] S. Araki, M. Nakashima, R. Settai, T. C Kobayashi, and Y. Onuki. Pressure-induced superconductivity in an antiferromagnet $CeRh_2Si_2$. *Journal of Physics: Condensed Matter*, 14(21):L377, 2002.

[135] D. Jaccard, K. Behnia, and J. Sierro. Pressure induced heavy fermion superconductivity of $CeCu_2Ge_2$. *Physics Letters A*, 163(5):475–480, 1992.

[136] F. M. Grosche, S. R. Julian, N. D. Mathur, and G. G. Lonzarich. Magnetic and superconducting phases of $CePd_2Si_2$. *Physica B: Condensed Matter*, 223:50–52, 1996.

[137] R. Boursier, A. Villaume, G. Lapertot, D. Aoki, G. Knebel, and J. Flouquet. Comparison between Ce and Yb heavy fermion compounds: $CeRh_2Si_2$ versus $YbRh_2Si_2$. *Physica B: Condensed Matter*, 403(5):726–730, 2008.

[138] Y. Kawasaki, K. Ishida, Y. Kitaoka, and K. Asayama. Si-NMR study of antiferromagnetic heavy-fermion compounds $CePd_2Si_2$ and $CeRh_2Si_2$. *Physical Review B*, 58(13):8634, 1998.

[139] H. Mori, N. Takeshita, N. N Môri, and Y. Uwatoko. Effect of pressure on the magnetization of single crystal $CeRh_2Si_2$. *Physica B: Condensed Matter*, 259261:58 – 60, 1999.

[140] S. Araki, R. Settai, T. C. Kobayashi, H. Harima, and Y. Ōnuki. Fermi surface instability in $CeRh_2Si_2$ under pressure. *Physical Review B*, 64(22):224417, 2001.

[141] V. Vildosola, A. M. Llois, and M. Alouani. Spectral properties and crystal-field splittings in CeM_2Si_2 (M= Ru, Rh, or Pd) compounds. *Physical Review B*, 71(18):184420, 2005.

[142] S. Fujimori, A. Fujimori, Kenya Shimada, T. Narimura, K. Kobayashi, H. Namatame, M. Taniguchi, H. Harima, H. Shishido, S. Ikeda, D. Aoki, Y. Tokiwa, Y. Haga, and Y. Ōnuki. Direct observation of a quasiparticle band in $CeIrIn_5$: An angle-resolved photoemission spectroscopy study. *Physical Review B*, 73:224517, Jun 2006.

[143] D. V. Vyalikh, S. Danzenbächer, A. N. Yaresko, M. Holder, Yu. Kucherenko, C. Laubschat, C. Krellner, Z. Hossain, C. Geibel, M. Shi, L. Patthey, and S. L. Molodtsov. Photoemission insight into heavy-fermion behavior in $YbRh_2Si_2$. *Physical Review Letters*, 100:056402, Feb 2008.

[144] S. Danzenbächer, Yu. Kucherenko, C. Laubschat, D. V. Vyalikh, Z. Hossain, C. Geibel, X. J. Zhou, W. L. Yang, N. Mannella, Z. Hussain, Z.-X. Shen, and S. L. Molodtsov. Energy dispersion of $4f$-derived emissions in photoelectron spectra of the heavy-fermion compound $YbIr_2Si_2$. *Physical Review Letters*, 96:106402, Mar 2006.

[145] S. Danzenbächer, Yu. Kucherenko, D. V. Vyalikh, M. Holder, C. Laubschat, A. N. Yaresko, C. Krellner, Z. Hossain, C. Geibel, X. J. Zhou, W. L. Yang, N. Mannella, Z. Hussain, Z.-X. Shen, M. Shi, L. Patthey, and S. L. Molodtsov. Momentum dependence of $4f$ hybridization in heavy-fermion compounds: Angle-resolved photoemission study of $YbIr_2Si_2$ and $YbRh_2Si_2$. *Physical Review B*, 75:045109, Jan 2007.

[146] C. G. Olson, P. J. Benning, M. Schmidt, D. W. Lynch, P. Canfield, and D. M. Wieliczka. Valence-band dispersion in angle-resolved resonant photoemission from LaSb. *Physical Review Letters*, 76(22):4265, 1996.

[147] C. G. Olson, S. J. Chase, P. Canfield, and D. W. Lynch. Crystal momentum conservation in resonant photoelectron emission. *Journal of electron spectroscopy and related phenomena*, 93(1):175–180, 1998.

[148] N. Grewe and F. Steglich. Handbook on the physics and chemistry of rare earths vol 14. *North-Holland, Amsterdam*, page 343, 1991.

[149] S. Horn, E. Holland-Moritz, M. Loewenhaupt, F. Steglich, H. Scheuer, A. Benoit, and J. Flouquet. Magnetic neutron scattering and crystal-field states in $CeCu_2Si_2$. *Physical Review B*, 23(7):3171, 1981.

[150] E. Holland-Moritz, W. Weber, A. Severing, E. Zirngiebl, H. Spille, W. Baus, S. Horn, A. P. Murani, and J. L. Ragazzoni. Crystal-field splitting and magnetic relaxation in $CeCu_{2.02}Si_2$. *Physical Review B*, 39(10):6409, 1989.

[151] C. Stassis, B. Battlog, J. P. Remeika, J. D. Axe, G. Shirane, and Y. J. Uemura. Polarized-neutron study of the paramagnetic scattering from $CeCu_2Si_2$. *Physical Review B*, 33(3):1680, 1986.

[152] Y. J. Uemura, C. F. Majkrzak, G. Shirane, C. Stassis, G. Aeppli, B. Batlogg, and J. P. Remeika. Polarized neutron scattering from $CeCu_2Si_2$ in applied magnetic fields. *Physical Review B*, 33(9):6508, 1986.

[153] C. D. Bredl, W. Lieke, R. Schefzyk, M. Lang, U. Rauchschwalbe, F. Steglich, S. Riegel, R. Felten, G. Weber, J. Klaasse, J. Aarts, and F. R. de Boer. Specific heat and thermal expansion of $CeCu_2Si_2$ at low temperature. *Journal of Magnetism and Magnetic Materials*, 47:30–32, 1985.

[154] B. Batlogg, J. P. Remeika, A. S. Cooper, and Z Fisk. Magnetism and superconductivity in $CeCu_2Si_2$ single crystals. *Journal of Applied Physics*, 55(6):2001–2003, 1984.

[155] S. L. Cooper, M. V. Klein, Z. Fisk, and J. L. Smith. Raman scattering study of the electronic and vibrational excitations in $CeCu_2Si_2$. *Physical Review B*, 34(9):6235, 1986.

[156] T. Kong, C. E. Cunningham, V. Taufour, S. L. Bud, M. L. C. Buffon, X. Lin, H. Emmons, and P. C. Canfield. Thermodynamic and transport properties of single crystalline RCo_2Ge_2 (R= Y, La-Nd, Sm-Tm). *Journal of Magnetism and Magnetic Materials*, 358:212–227, 2014.

[157] H. Fujii, E. Ueda, Y. Uwatoko, and T. Shigeoka. Magnetic properties of $CeCo_2Ge_2$ and $NdCo_2Ge_2$ single crystals. *Journal of Magnetism and Magnetic Materials*, 76:179–181, 1988.

[158] P. H. Ansari, B. Qi, G. Liang, I. Perez, F. Lu, and M. Croft. The near-edge x-ray absorption spectroscopy of RT_2Si_2 and RT_2Ge_2 compounds. *Journal of Applied Physics*, 63(8):3503–3505, 1988.

[159] F. Venturini, J. C. Cezar, C. De Nadaï, P. C. Canfield, and N. B. Brookes. The Ce 4f electronic structure in $CeCo_2Ge_2$: a soft x-ray resonant photoemission investigation. *Journal of Physics: Condensed Matter*, 18(40):9221, 2006.

Summary

Cerium intermetallic compounds exhibit fascinating magnetic, electronic and thermodynamic properties at low temperatures. Their physics is governed by two competing interactions between the conduction band and localised $4f$ electrons: the Kondo effect tends to screen the $4f$ magnetic moments while RKKY exchange favours ordered local moments. From this competition, a complex phase diagram arises and its understanding requires a full characterisation the $4f$ levels. The crystal electric field (CEF) effects lift the degeneracy of the spin-orbit multiplets and the resulting energy splittings (tens of meV) as well as the symmetry of the ground and excited states must be determined experimentally. CEF effects in the lanthanides can be studied with a number of experimental probes including magnetic susceptibility, inelastic neutron scattering, x-ray absorption spectroscopy or photoemission spectroscopy. However, each of these techniques has limitations which can prevent an accurate characterisation. This thesis discusses the potential of Resonant Inelastic soft X-ray Scattering (soft-RIXS) to become a new probe of the CEF in cerium compounds. The latest advances in instrumentation have pushed the energy resolution in soft RIXS down to 30 meV at the Ce M_5 edge, good enough to resolve the electronic transitions between the lowest lying $4f$ levels. This is demonstrated using the example of $CeRh_2Si_2$ spectra. The observed energies of the spin-orbit and CEF excitations provide a direct measurement of the $4f$ splittings and the comparison of the experimental spectra with full-multiplet single-ion calculations unambiguously identifies the symmetry of the lowest CEF levels. The orientation of the wave-functions in the crystal *ab* plane can also be determined in a straightforward manner by measuring the polarisation of the inelastically scattered photons. The interaction with itinerant states can lead to a momentum dependence of the $4f$ levels' energy and this leaves signatures in the excitation spectra that can be observed in RIXS. A simple model is proposed to explain the observed $\mathbf{q}$ dependence but further theoretical work is needed to properly account for the momentum dependence of the $4f$ excitations. Using the examples of $CeCu_2Si_2$ and $CeCo_2Ge_2$ it is demonstrated that RIXS can probe CEF splittings that are significantly smaller or much larger than those in $CeRh_2Si_2$. With better energy resolution and more advanced modelling RIXS studies of the CEF in Cerium and other lanthanide ions will become even more accurate in the future.

Résumé

Les composés intermétalliques à base de cérium présentent à basse température des propriétés magnétiques, électroniques et thermodynamiques tout à fait fascinantes. Deux interactions majeures entre la bande de conduction et les électrons localisés de la couche 4f entrent en compétition et régissent la physique de ces composés: l'effet Kondo tend à écranter les moments magnétiques 4f alors que les interactions RKKY favorisent plutôt des moments localisés et ordonnés. Un diagramme de phase complexe naît de cette compétition et le comprendre exige une caractérisation complète des niveaux 4f. La dégenerescence des multiplets liés au couplage spin-orbit est levée par les effets de champ cristallin, et les écarts entre les niveaux d'énergie qui en résultent ainsi que les symétries des états fondamentaux et excités doivent être déterminés expérimentalement. Les effets de champ cristallin dans les lanthanides peuvent être sondés par diverses techniques expérimentales dont la susceptibilité magnetique, la diffusion inélastique de neutrons, la spectroscopie par absorption de rayons X ou de photoémission. Cependant, chacune de ces techniques présente des limitations propres qui empêchent une caractérisation précise de ces effets. Nous présentons dans cette thèse les capacités de la technique de diffusion résonante inélastique des rayons X mous (soft-RIXS) à sonder les effets de champ cristallin dans les composés à base de cérium. Les dernieres avancées en instrumentation ont permis de repousser les limites de la résolution en énergie jusqu'à 30 meV au seuil M5 du Cérium, suffisant pour séparer les transitions électroniques des plus bas des niveaux 4f. Le composé CeRh2Si2 a été étudié à titre d'exemple. Les énergies des excitations de couplage spin-orbit et de champ cristallin observées expérimentalement fournissent une mesure directe des écarts des niveaux 4f, tandis que la comparaison entre les spectres expérimentaux et des calculs basés sur le multiplet complet dans l'approximation à un ion permet d'identifier sans ambigüité la symétrie des états de plus basse énergie du champ cristallin. L'orientation des fonctions d'ondes dans les plans ab du cristal peut aussi être déterminée de manière très simple en mesurant la polarisation des photons diffusés de manière inélastique. L'interaction avec les états itinérants peut introduire une variation de l'énergie des niveaux 4f en fonction du vecteur de diffusion q, qui se traduit par des signatures observables dans les spectres de diffusion inélastique résonante de rayons X. Un modèle simple est proposé pour expliquer la variation observée en fonction de q, mais des calculs théoriques plus poussés apparaissent nécessaires pour rendre compte de manière plus exacte de ces variations. L'étude des composés CeCu2Si2 et CeCo2Ge2 montre que la diffusion inélastique des rayons X peut sonder des effets de champ cristallin bien plus faibles ou bien plus importants que ceux observés dans CeRh2Si2. Dans le futur, une meilleure résolution en énergie et des modélisations plus poussées devraient encore améliorer la précision des études des effets de champ cristallin dans les composés de Cérium et autres lanthanides par diffusion inélastique de rayons X.